Despiking Velocimetric Data with 2D ARMA Models and the Role of Impulse in Sediment Movement on Variable Bed Slopes

by

Scott Dilling

A thesis
presented to the University of Waterloo
in fulfillment of the
thesis requirement for the degree of
Master of Applied Science
in
Civil Engineering

Waterloo, Ontario, Canada, 2015

I hereby declare that I am the sole author of this thesis. This is a true copy of the thesis, including any required final revisions, as accepted by my examiners.

I understand that my thesis may be made electronically available to the public.

Abstract

The link between hydrodynamics and morphology of river bedforms is an ongoing field of research. Existing studies have been unable to provide a complete understanding of the physical conditions required to initiate sediment movement, partially due to the complexities in accounting for turbulent fluctuations within a fluid. Flume experiments and velocity data filtering algorithms were completed to improve the methods available for use in future studies investigating the role of turbulence in particle mobility under non-uniform bed conditions.

High resolution velocity profiling instruments, such as the Vectrino II™ manufactured by Nortek AS, have enabled a new generation of turbulence studies, but data filtering methods have not kept pace. A new method was developed that uses autoregressive moving average (ARMA) models for spike detection, replacement and classifying cell quality. A series of flume experiments were completed to test the concept of impulse under non-uniform bed conditions. Impulse is hypothesized to be a superior predictor of transport potential by accounting for the magnitude and duration of individual turbulent events. Six experiments were completed under low flow conditions with local bed slopes ranging from -2.7^{o} to $+2.7^{o}$ relative to the overall bed to determine the spatial distribution of impulse events as well as the role of particle size and specific gravity. Another experiment was completed at high flow to test impulse with respect to the movement of a spherical particle placed at 42 sampling locations along the bed of the flume. Lastly, a Proof of Concept is presented for synchronized measurement of fluid velocities and image recordings of particles along the bed. Automated algorithms track a particle of interest and determine the precise time of movement for correlation with the velocity time series.

Overall, ARMA models offer a promising approach for filtering velocimetric data. Kurtosis of the model residuals is revealed to be a robust cutoff parameter within the despiking algorithm. Flume experiments demonstrate that impulse events are strongest immediately downstream of the transition to zones of decelerating flows, and strengthen toward the sidewalls of the flume. A positive correlation is noted between impulse and particle mobility, but additional testing is recommended to determine the precise turbulent events required to move a range of particle sizes under varying hydraulic conditions. The developed Proof of Concept should facilitate this type of experimental study.

Acknowledgements

I would like to thank my supervisor, Dr. Bruce MacVicar, for his guidance and support throughout this research project. Critical steps in my research were only possible due to his expertise and patience.

I extended my thanks to all the people who made completing my masters degree a much more rewarding and unique experience: Dr. David Brush, Vernon Bevan, Christina Bright, John Hufnagel, and all the river engineering graduate students.

Lastly, I would also like to thank Sarah Sheridan and my family for supporting me throughout the entire process.

Table of Contents

List of Figures

List of Tables

Chapter 1
INTRODUCTION

Rivers have a profound effect on the landscape of the planet by eroding the land and transporting sediments to downstream locations. Early civilizations situated themselves near riverbanks to take advantage of food sources, clean drinking water, irrigation for agriculture and accessibility to transportation routes. Rivers have been constantly modified throughout human history, with projects including channel straightening, dam construction and gravel mining. More recently, urbanized areas cause a reduction in the permeability of ground cover resulting in high intensity and short duration flood flows and decreased supply of bed material to the river (Annable et al, 2010). River restoration projects have become increasingly common, with more than 37,000 documented projects in the United States representing an annual expenditure of greater than $1 billion spent since 1990 (Bernhardt et al, 2005). Unfortunately, many of these restoration designs fail due to unintended erosion or sedimentation and an inadequate understanding of the sediment transport processes occurring in a river (Shields et al, 2003).

The study of bed load sediment transport is of interest to researchers in the fields of fluvial geomorphology, aquatic habitat protection, flood protection, hydraulic infrastructure management and water quality improvements (Diplas et al, 2010; Smart and Habersack, 2008). There is a growing recognition of the importance of self-maintaining processes to improve the sustainability and success of restoration projects (Shields et al, 2003; Parkinson et al, 2012). Recent restoration designs in gravel bed rivers have included the construction of bed features, such as riffle pool structures, for promoting habitat diversity by creating micro-habitats (Parkinson et al, 2012). These bed features are made of bed load sediments, which are defined as the component of transported fluvial material that is rolled or saltated along the bed with particle diameters coarser than 0.2 mm (Gomez and Church, 1989). An improved understanding of the mechanics of bed load transport is the defining problem of a growing body of research on the morphological processes that occur within a riverbed (Shields et al, 1995; Parkinson et al, 2012). A research gap has been noted between the hydraulics and morphology of gravel bed river systems, partially due to the difficulty of collecting high quality data in sufficient temporal and spatial densities to understand the interactions between flow hydraulics and sediment transport (de Almeida and Rodriguez, 2011). There is a need for high precision laboratory experimentation to resolve fundamental questions on the interaction between turbulent velocities in the near-bed environment and the mobility of

an alluvial sediment bed, particularly where the bed is non-uniform and flow conditions are near the point of incipient motion. Recent technological advancements in velocity profiling instrumentation offer the potential for precise measurement of turbulent velocities in the near-bed environment. Specialized testing of these instruments is required as well as a new set of filtering algorithms that improve the spike detection and replacement capabilities as well as accurately classify the quality of data in each sampling cell.

Velocity profiling instruments capable of measuring high resolution and high frequency three-dimensional data have enabled a new generation of advanced hydrodynamic studies. However, a limited number of studies have examined the role of turbulence in sediment mobility and available findings are inconclusive. The potential for a new velocity profiling instrument, the Vectrino II™ (VII) from Nortek AS, to measure the near-bed turbulence flow environment is tested to determine if it is appropriate for use high-precision turbulence and sediment mobility investigations. As with all velocity profiling instruments, the collected data are susceptible to erroneous spikes and poor quality time series. Filtering algorithms are required to avoid biasing the mean and turbulence statistics and to identify non-representative data within the sampling profile (Cea et al, 2007). Several algorithms for despiking velocity data are available, such as Goring and Nikora's (2002) phase-space threshold and an acceleration threshold approach (Cea et al, 2007), but various drawbacks are noted, including: decoupling of the spike detection and replacement stages; spatial and temporal correlative properties within the sampling profile are not incorporated; and unrealistic replacement values that can systematically reduce the representative variance within the time series. Advanced studies requiring high-quality, filtered data for meaningful analysis, such as in turbulence studies, necessitates the development of an improved set of filtering algorithms.

The availability of a single parameter for defining the threshold condition for the initiation of particle movement remains elusive to researchers. An abundance of bed load transport equations are available, but no single formula is universally accepted and none consistently perform well under a range of conditions. The abundance of transport formulae is worrisome to researchers, given the lack of reliable data sets on which they are developed (Gomez and Church, 1989). Common formulae for estimating the incipient motion condition for bed load sediments use time-averaged parameters, such as flow velocity, flow depth or energy gradient to provide a bulk estimate of the range of particle sizes that are expected to be mobile. However, formulae using these hydraulic parameters are ultimately differently scaled

equations of the discharge and cannot accurately characterize natural flow conditions (Gomez and Church, 1989). Considerable research has focused on evaluating the performance of existing transport formulae, rather than collecting high-quality data sets and developing enhanced approaches for predicting bed load transport capacities. Common sediment movement relationships have been subject to incremental refinement and improvement as additional laboratory data sets become available. Transport formulae have been noted to inadequately account for the important role of turbulence in sediment movement (Sumer et al, 2003; Nelson et al, 1995; Diplas et al, 2008; Celik et al, 2010; Radice et al, 2013). Furthermore, recent laboratory experiments have demonstrated that the magnitude of turbulent forces alone does not provide a reliable criterion for estimating the onset of particle mobility. Rather, the magnitude *and* duration of the force must be considered. The product of magnitude and duration of a turbulent force, or impulse, is proposed to be more applicable and a potential universal criterion for determining particle movement potential (Diplas et al, 2008; Valyrakis et al, 2011). The concept of impulse was developed by Diplas et al (2008) using metallic spheres in a dry environment and a laser to precisely determine the onset of particle motion. Subsequent studies by Celik at al (2010) used Teflon™ spheres at a single measurement location under uniform flow conditions to determine the threshold impulse conditions for a particle of interest. Within this thesis, tests are described that were designed to examine the threshold impulse condition under non-uniform bed conditions using the VII and visual observation of a Teflon sphere. Additional laboratory flume experiments were completed to develop an understanding of the spatial distribution of impulse events under non-uniform conditions over a rough bed.

Determining the precise turbulent conditions that cause particle movement is complicated by the difficulty in obtaining high-resolution simultaneous measurement of near-bed fluid velocities and particle location. No standard procedure is currently available for testing the concept of impulse with regards to sediment mobility. A new methodology is required to allow for simultaneous measurement of turbulent velocities acting on a particle of interest and the precise particle location. Furthermore, it is desirable to determine the trajectory of a mobile particle for use in evaluating the mode of entrainment, such as rolling or lifting. Existing experimental set ups are highly customized (Diplas et al, 2008; Valyrakis et al, 2011; Celik et al, 2010) and could not be applied in this study due to instrumentation availability, insufficient collected parameters and researcher preferences. Therefore, a Proof of Concept is developed in this study using the VII for velocity measurement and a high-resolution machine vision camera with an automated image analysis program for particle tracking. This Proof of Concept is intended to provide a

methodology for future laboratory studies investigating impulse and particle mobility and is universally applicable for a range of particles, bed slopes and particle locations within laboratory flumes.

Overall, the scope of this study consists of two interrelated components: filtering of velocimetric data and laboratory flume experiments investigating sediment mobility. The filtering algorithms were developed to:

- Filter high-frequency velocimetric data, including spike detection, replacement and cell quality classification
- Work with any type of multi-cell velocity profiling instruments, including the VII
- Couple the detection and replacement of spikes
- Incorporate spatial and temporal information into the algorithm
- Allow for the classification of data quality for each cell in sampling profile

The filtering algorithms are completed as a set of Matlab™ algorithms and produce a 'clean' data set for use in subsequent data analysis stages, such as the calculation of impulse events within a time series. It is anticipated that these filtering programs will be made available to interested researchers at a later date as part of a journal paper submission through an online software repository such as github.com.

The second component focuses on laboratory flume experiments for testing high-precision instruments (VII and machine-vision camera) and the development of experimental methodologies for use in turbulence and sediment mobility studies. Following preliminary testing of the VII, a limited number of experiments were completed to determine the spatial distribution of impulse events under a range of non-uniform bed conditions. A Proof of Concept was developed to provide a new methodology for simultaneous measurement of fluid velocities and particle location for future use in sediment transport studies, including impulse investigations. The motivation for the flume experiments were to:

- Test the VII for suitability in measuring near-bed velocities
- Investigate the relationship between impulse events and particle mobility
- Study the spatial distribution of impulse events under a range of non-uniform beds
- Develop and test a Proof of Concept for simultaneous measurement of turbulent velocities and particle location

This thesis is organized into seven chapters. Following this introduction, the second chapter provides an overview of literature available on sediment transport and examines the role of impulse in sediment movement. A brief review of the literature for existing despiking filtering algorithms is also provided. The third chapter is presented as a stand-alone proposed journal paper to describe the motivation, methods, results and discussion of a new filtering algorithm for the despiking of velocimetric time series. Chapter 4 provides the methodology and results of laboratory experiments evaluating impulse under different bed slopes. Chapter 5 describes methods developed for simultaneously measuring fluid velocities and sediment particle trajectories. The discussed methods are provided as a Proof of Concept, including a finalized procedure for future use in sediment mobility studies. Chapter 6 provides a discussion of the methods and results and includes recommendations for future work. Conclusions of this thesis are summarized in Chapter 7.

Chapter 2
LITERATURE REVIEW

This chapter provides a review of literature available on the study of hydrodynamics and the entrainment of sediment. An overview of existing methods that use mean flow conditions for estimating the incipient motion condition in gravel bed rivers is provided. The importance of accounting for turbulent fluctuations when estimating the incipient motion condition is discussed for both uniform and non-uniform flows. The concept of impulse is presented as a potentially superior estimator for predicting the onset of particle mobility by accounting for the duration and magnitude of individual turbulent events. The pervasive problem of collecting simultaneous data for hydrodynamic flow environment and sediment entrainment and transport is addressed, along with a discussion of existing methodologies and associated limitations. A discussion of flow dynamics over non-uniform beds is included, with a focus on the zones of accelerating and decelerating flows within riffle pool structures. A review of existing literature and data filtering methods for spike detection, replacement and cell quality assessment are discussed separately in Chapter 3.

2.1 Incipient motion as a function of mean flow conditions

The incipient motion condition defines the point at which a sediment particle just begins to move and governs the mechanics of particle entrainment and movement as well as the morphology of river bed features. Numerous formulae have been advocated to estimate the relationship between flow conditions, sediment parameters (e.g., size, shape, exposure) and the transport rate. However, the development of a single parameter or set of formulae delineating the movement/no movement threshold condition for sediments in gravel bed rivers continues to elude researchers.

The simplest and most common relationship for estimating incipient motion is shear stress, τ, which was developed nearly 80 years ago for uniform flow conditions. This parameter provides a spatially and temporally averaged measure of sediment transport potential (Buffington and Montgomery, 1997). The mean boundary shear stress is a function of the gravitational force acting parallel to the bed, given by:

$$\tau = \gamma RS \qquad (1)$$

where γ is the specific weight of the fluid, R is the hydraulic radius and S is the water surface slope (energy slope). The shear velocity, u^*, provides an alternate measure of the shear stress and is estimated using τ and the density of the fluid, ρ:

$$u^* = \sqrt{\tau/\rho} \tag{2}$$

Since sediments are displaced from the bed region, it follows that estimating hydraulic parameters within the near bed region is of particular interest. The near bed, or inner, region extends up to approximately $y/\gamma \approx 0.2$, where y is the distance above the bed, and γ is distance above the bed to where the maximum velocity in the profile is reached. The inner region of flows for rough beds is controlled by the roughness of the wall and can be characterized by the kinematic viscosity υ, equivalent roughness k_s, and the friction or shear velocity u^*. Within this inner region u^* can be described as a logarithmic distribution using the law of the wall (log-law):

$$\frac{u}{u^*} = \frac{1}{\kappa}\ln\left(\frac{y}{k_s}\right) + B_r \tag{3}$$

(Kironoto and Graf, 1994) where u is the mean velocity at distance y from the reference level, κ is von Karman's constant and B_r is a numerical constant of integration. This relationship has been found to be valid for both uniform and non-uniform flows (Kironoto and Graf, 1995). To estimate the shear velocity within the inner layer the Clauser method can be used with the log-law profile (Kironoto and Graf, 1995; Kendall et al, 2006). In this method the fit of the mean velocities at multiple sampling cells are used to estimate u^* within the inner logarithmic region. Shield's parameter, or the dimensionless shear stress, τ^*, defines the ratio between the shear force and the sediment particle weight and can be calculated using the shear velocity as:

$$\tau^* = (u^*)^2/(G-1)gD \tag{4}$$

(Julien, 2002) where G is the specific weight of the sediment particle and g is gravitational acceleration. The critical Shield's parameter, τ_c^*, or dimensionless critical shear stress, is considered a seminal contribution in sediment transport studies (McEwan and Heald, 2001) and provides an estimate of the threshold shear stress, τ_c, required for the initiation of motion for a given particle size, i:

$$\tau_c^* = \tau_c/(\rho_s - \rho)gD \tag{5}$$

(Buffington and Montgomery, 1997) where ρ_s and ρ are the particle and fluid densities, respectively, and D is the particle size of interest for transport potential. Due to the stochastic nature of sediment transport and the specific experimental measurement methodologies, it is difficult to define a single τ_c^* value for estimating the incipient motion condition for a given particle size. Several researchers have proposed such estimates ranging from 0.05 to 0.08, but these estimates cannot be universally applied due to variations in experimental procedures such as measurement methods, flow conditions, sediment properties and analysis methods (Buffington and Montgomery, 1997).

In many practical river engineering applications, the sediment transport rate is of interest. Most transport formulae utilize a mean estimate of flow conditions, such as shear stress, shear velocity or critical Shield's parameter to estimate the incipient condition. Among the most commonly used transport formulae for steady, uniform conditions is the Meyer-Peter and Muller (MPM) transport equation, originally published in 1948. This relationship estimates the bed load sediment transport rate in open channels as a function of the excess bed shear stress of a fluid that is available for acting on bed load particles. Wong and Parker (2006) reanalyzed the original data sets used by Meyer-Peter and Muller to update the equation by removing an unnecessary bed correction factor and to add an improved correction factor for sidewall effects, and is given by:

$$q^* = 3.97(\tau_b^* - 0.0495)^{1.50} \quad (6)$$

where q^* is the dimensionless volume bed load transport rate per unit width, and τ_b^* is the sidewall corrected boundary shear stress and τ is the boundary shear stress in the bed region:

$$\tau_b^* = \tau/(\rho_s - \rho)gD_i \quad (7)$$

The performance of sediment transport equations that were developed using mean hydrodynamic conditions and bulk transport volumes, including the modified MPM, can predict transport rates that vary more than an order of magnitude (Buffington and Montgomery, 1997).

Research projects which seek to better understand the link between flow conditions and the mobility of sediment particles require innovative methods for obtaining simultaneous measurement of hydrodynamic parameters and sediment location. The difficulty in collecting high quality data has resulted in only a limited number of relevant studies and the developed methods have typically been manually intensive. For example, in their study of the effect of bed surface grain size distribution on sediment transport rates,

Wilcock and McArdell (1993) used manual analysis of a series of photographs of a 'bed of many colors' along with measurements of mean hydraulic conditions. Their study examined the effect of sediment particles on the bed available for transport, rather than the typical usage of the bulk composition of the entire bed. Within a laboratory flume, 14 grain size fractions with particles in each fraction were painted a different color and mixed with the bed sediments. From photographs of the surface of the bed, the grain size distribution of particles on the bed available for transport could be identified. A scaled transport rate was then correlated with mean measurements of fluid velocity and bed shear stress to determine the hydraulic conditions required for mobility of a given grain size fraction to occur.

2.2 Influence of turbulence on incipient motion

Sediment can become mobile even when temporally and spatially averaged hydraulic parameters remain below threshold conditions (Celik et al, 2010; Diplas et al, 2008; Diplas et al, 2010; Valyrakis et al, 2010). To address this phenomenon, a limited number of recent research approaches have shifted to studying the specific mechanics of particle movement, with a focus on accounting for turbulent fluctuations in a fluid (Radice et al, 2013). An improved understanding of the role of turbulence in sediment transport is especially important when hydraulic conditions are near the point of incipient motion as even a minor change in the flow parameters can result in a substantial increase in the frequency of particle entrainment (Celik et al, 2010; Sumer et al, 2003). Velocity time series for the streamwise (u), lateral (v) and vertical (w) directions can be separated into the mean ($\bar{u}, \bar{v}, \bar{w}$) and fluctuating components (u', v', w') using a Reynolds decomposition such that:

$$u = \bar{u} + u' \tag{8}$$

$$v = \bar{v} + v' \tag{9}$$

$$w = \bar{w} + w' \tag{10}$$

The Reynolds shear stress, τ_R, accounts for turbulent fluctuations and is calculated using the decomposed velocities as follows:

$$\tau_R = \rho u_*^2 = -\rho\overline{u'v'} \tag{11}$$

(Kironoto and Graf, 1995). Reynolds shear stress provides a simple, time-averaged measure of turbulence intensity at a given sampling location and provides an indication of sediment movement potential, whereby larger τ_R values are generally associated with greater mobility. However, time-

averaged parameters, such as τ_R, do not allow for efficient investigation of the link between hydrodynamic flow conditions and the movement of individual sediment particles. Some researchers have suggested that a specific threshold bed shear stress for predicting incipient motion does not exist since mean flow characteristics do not account for individual turbulent events that can temporary exceed threshold conditions and cause a particle to move (Celik et al, 2010). For example, when conditions are near the point of incipient motion the exposure and imbrication of a particle can cause an order of magnitude variance in the dimensionless critical shear stress and produce an equivalent effect on sediment transport rates (Buffington and Montgomery, 1997). The work of Sumer et al (2003) showed that minute changes in the turbulence intensity when conditions are near the point of incipient motion can produce substantial increases in the amount of entrained sediment. In their study, a 50-fold increase in the sediment transport rate could be achieved even when bed shear stress remained constant and the turbulence intensity increased by only a factor of 1.3. Schmeeckle et al (2007) showed that for a spherical particle protruding half of its diameter above a rough bed, instantaneous turbulent fluctuations caused the horizontal force to increase by a factor of four relative to the mean force. The work of Nelson et al (1995) demonstrated that under specific laboratory conditions a 14% increase in the particle Reynolds number and 35% increase in τ_R was noted to produce a 50-fold increase in the entrainment rate of a spherical test particle during experiments under uniform flow conditions. They further argue that the nature of turbulence, such as sweeps ($u' > 0$, $v' < 0$) and ejections ($u' < 0$, $v' > 0$), play a critical role in understanding the rates of sediment transport, whereas bed shear stress provides an incomplete understanding. More specifically, it was shown that a decrease in the bed shear stress could be associated with increased rates of sediment transport. For example, outward interactions ($v' > 0$) occupied 13% of the total time of a flow and were associated with reduced shear stresses, yet 32% of the sediment was transported under these conditions.

The transport studies described above support the hypothesis that near bed turbulent structures are strongly associated with the mobility of sediment particles. While these studies have advanced the prediction of sediment transport rates, they have not attempted to establish a direct link between the movement of individual grains of sediment and the precise turbulent forces acting on the given particle. A limited amount of research has been conducted to investigate the hydrodynamic conditions that cause movement, but studies of this nature are hampered by the difficulties in collecting high-quality, non-intrusive, synchronized data for both the near-bed hydraulic conditions and the movement of sediment particles, especially when conditions are near the point of incipient motion (Nelson at al, 1995, Diplas et

al, 2010). Velocity profiling instruments, such as the VII, are seen as a promising technology for collecting high-resolution and high-frequency fluid velocities, but additional application-specific testing is required to confirm suitability in collecting near-bed turbulent velocities.

2.3 Impulse as a method of predicting incipient motion

The physical mechanics responsible for the entrainment of individual sediment particles remain poorly understood. Well-established sediment transport formulae that used time-averaged hydraulic parameters or peak turbulent velocities provide an incomplete description of the conditions required for the initiation of movement. Recently, Diplas et al (2008) experimentally demonstrated that it is not only the magnitude, but also the duration of individual turbulent structures that are responsible for particle movement. Many large magnitude turbulence events are of very short duration and therefore do not impart a sufficient amount of sustained force on the particle to cause dislodgement. Rather, sustained, non-peak (but still sufficiently large) turbulent events provide a better likelihood of causing particle movement. This concept, referred to as impulse, is defined as the product of the magnitude and duration of a turbulent event:

$$Impulse = I = \int_{t_1}^{t_2} F(t)dt = \langle F \rangle T \tag{12}$$

With the relative impulse event magnitude given by:

$$I = \int_{t_1}^{t_2} u^2(t)dt = \langle u^2 \rangle_i T_i \tag{13}$$

(Celik et al, 2010). An impulse event begins when the force exerted on the particle by the fluid, $F(t)$, is larger than the critical force for particle movement, $F_{D,cr}$. The duration of the event, T, is calculated as the length of time that $F_{D,cr}$ is exceeded. $\langle F \rangle$ is the time-averaged force over T, and $\langle u^2 \rangle$ is the time-averaged squared streamwise velocity. The duration of an individual event can be described as the length of time that u^2 exceeds u_{cr}^2, as illustrated by the shaded area in Figure 1.

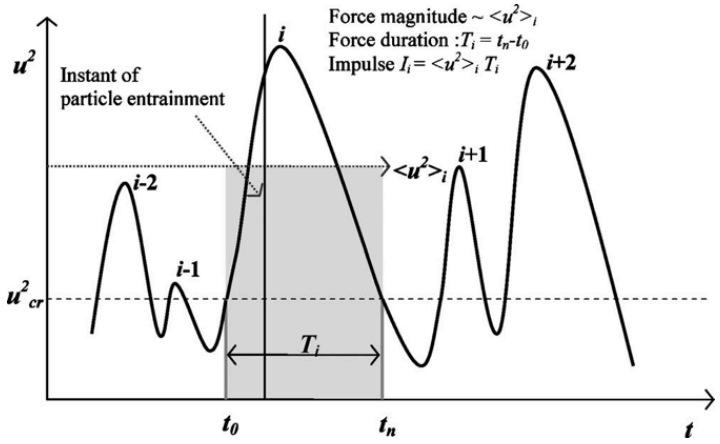

Figure 1: Illustrative description of impulse events (Celik et al, 2010)

For a highly exposed particle, the drag forces acting on the particle are generally much larger than lift forces and therefore are assumed to be the dominant force causing entrainment (Celik et al, 2010). The drag force exerted on a sphere by a moving fluid can be estimated as:

$$F_D = \frac{1}{2}\rho u^2 C_D A \tag{14}$$

(Celik et al, 2010) where C_D is the drag coefficient and A is the projected surface area perpendicular to the streamwise flow. Typically, drag coefficients are estimated from experiments in still water and are generally too low for use in sediment transport equations. For a spherical particle under natural bed conditions an average C_D value of 0.76 is recommended (Schmeeckle et al, 2007). The critical drag force for a fully exposed spherical particle can be calculated using:

$$F_{D,cr} = f_v W_s \left[\cos(\beta)\frac{X}{Z} - \sin(\beta)\right] \tag{15}$$

(Celik et al, 2010) where the hydrodynamic mass coefficient, f_v, is calculated as $[1 + 0.5(\rho/\rho_s - \rho)]$, W_s is the submerged weight of the particle, ρ_s is the density of the particle, ρ is the density of water, β is the bed slope, and X and Z are the lever arms parallel and perpendicular to the bed (herein referred to as X_{arm} and Z_{arm}, respectively) for a spherical particle resting in the pocket of identically sized bed of spheres, as shown in Figure 2.

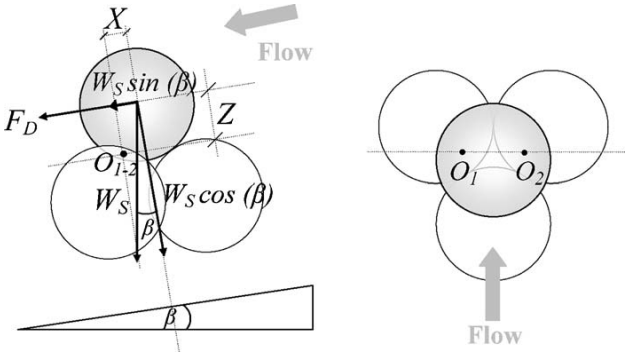

Figure 2: Drag and gravitational forces acting on spherical particle. Side view (left) and top view (right). (Celik et al, 2010)

Impulse events can be equivalently defined using the critical squared velocity, u_{cr}^2. By combining Equations 14 and 15, an estimate of the critical velocity at the onset of particle movement can be made using:

$$u_{cr}^2 = \frac{2}{\rho C_D A} f_v W_s \left[\cos(\beta)\frac{X}{Z} - \sin(\beta)\right] \tag{16}$$

(Celik et al, 2010). To test the concept of impulse in initiating sediment mobility, Diplas et al (2008) and Celik et al (2010) designed experiments to provide synchronized measurement of particle location and turbulent velocities acting on a single, fully exposed particle. These synchronized measurements were completed using laser Doppler velocimetry (LDV) for high-resolution measurement of the velocities acting on the particle, and a laser for high-resolution detection of movement, ranging from minor rocking to complete dislodgement. Flume experiments for both researchers were completed using uniform flows with a 12.7 mm Teflon sphere resting on a rough bed of densely packed spheres. The results of these experiments established the approximate minimum impulse event required for particle movement in the specific configuration used. Most significantly, the need to consider both the magnitude and duration of turbulent events was clearly established in their work. As shown in Figure 3, a total of 1465 experimental runs indicated that a minimum impulse threshold is present at approximately 0.0035 m^2/s for the sphere used in their study. Solid (black) circles represent turbulent events that were sufficient to cause sediment transport, with the vast majority being located above the dotted line, indicating that movement occurred. Open (gray) circles indicate that no movement occurred. This figure demonstrates a strong correlation between the impulse event, given by $\overline{u^2}T$, and the movement of individual particles whereas $\overline{u^2}$ alone is insufficient in determining movement potential.

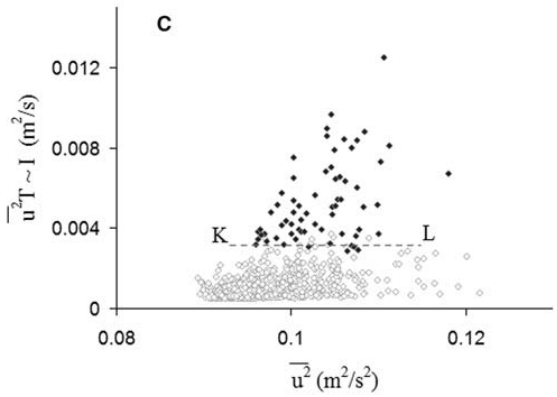

Figure 3: Transport as a function of impulse and velocity. Solid (black) sphere indicate movement occurred. (Diplas et al, 2008)

The development of the impulse concept provides a potentially substantial addition to a mechanistic understanding of particle entrainment in turbulent fluid flow.

2.4 Flow dynamics over non-uniform bed

Natural rivers are characterized by complex bed features, such as riffles and pools, which produce non-uniform flows. The entrainment, transport and deposition of sediments are responsible for the morphology and self-maintaining processes that occur along river beds (de Almeida and Rodriguez, 2011). An appreciation and understanding of the spatial and temporal distribution of turbulence in non-uniform flows is necessary to accurately estimate the sediment transport potential. Applying transport relationships developed for uniform flows to non-uniform conditions has been noted to produce poor results (Nelson et al, 1995). Under non-uniform conditions, turbulent fluctuations do not scale with the bed shear stress and therefore cannot be relied upon for an accurate prediction of sediment transport potential. More specifically, under non-uniform flows the production and dissipation of turbulence are unbalanced, causing localized regions dominated by large coherent turbulent structures that can significantly alter the local sediment transport potential (Nelson et al, 1995).

Riffle pool sequences create an undulating bed profile consisting of alternating sequences of deep pools and shallow riffles and provide energy dissipation, water aeration and grade control protection (Newbury and Gaboury, 1993). Riffle pool sequences are noted for their unique ability to remain stable and persist

under a wide range of flows, including large floods when many other bedforms are eroded (Church and Jones, 1982). Riffle pool sequences are found in low to moderate bed slopes with good floodplain access and have a meandering alignment. Substrate material is primarily comprised of fluvial gravels, but can range from sand to cobbles. Riffles generally occur within straight reaches of the channel and consist of coarse sediments, whereas pools occur within bends and consist of finer sediments. Pool spacing naturally occurs at approximately every five to seven channel widths, as shown in Figure 4 (Keller and Melhorn, 1978). Interestingly, the natural formation of riffle pool sequences has been noted following anthropogenic channel straightening and construction of a uniform gradient. Under these stressed conditions, riffle pools re-formed at the original spacing prior to construction (Newbury and Gaboury, 1993).

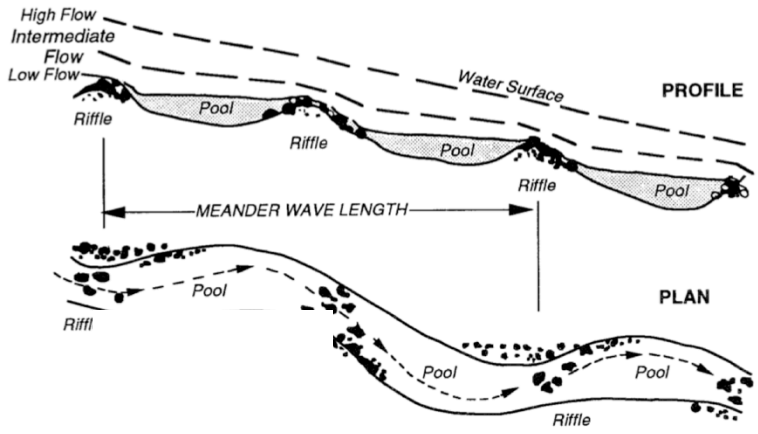

Figure 4: Riffle pool sequence (Newbury and Gaboury, 1993)

The natural formation and morphology of non-uniform bed forms are controlled by selective sediment transport, or sorting, with turbulence playing a central role. The study of turbulence structures in rough, non-uniform flow has been limited, with the first comprehensive study completed by Kironoto and Graf (1995) in a tilting laboratory flume. Parameters analyzed included normalized streamwise and vertical turbulent intensities (u'/u^* and v'/u^*, respectively) and normalized Reynolds shear stress given by:

$$\tau_R^+ = -\overline{u'w'}/u^{*2} \tag{17}$$

Using these parameters, an understanding of the imbalance in turbulence generation and dissipation under accelerating and decelerating flow condition can be quantified.

For decelerating flows, such as at the pool head where the flow depth increases, a positive pressure gradient is created resulting in a convective deceleration of flow (CDF). These conditions produce an abundance of turbulence and increased τ_R values relative to uniform flow conditions with the peak turbulence intensities occurring at a pronounced distance above the bed. Conversely, for accelerating flows, such as at the pool tail where the flow depth decreases, a negative pressure gradient produces a convective acceleration of flow (CAF). This creates an overall suppression of the turbulence resulting in reduced τ_R values with a local maximum near the bed. A summary of results from Kironoto and Graf (1995) are provided below in Figure 5, where the solid line represents uniform flow conditions and δ represents the distance above the bed where the maximum velocity is achieved.

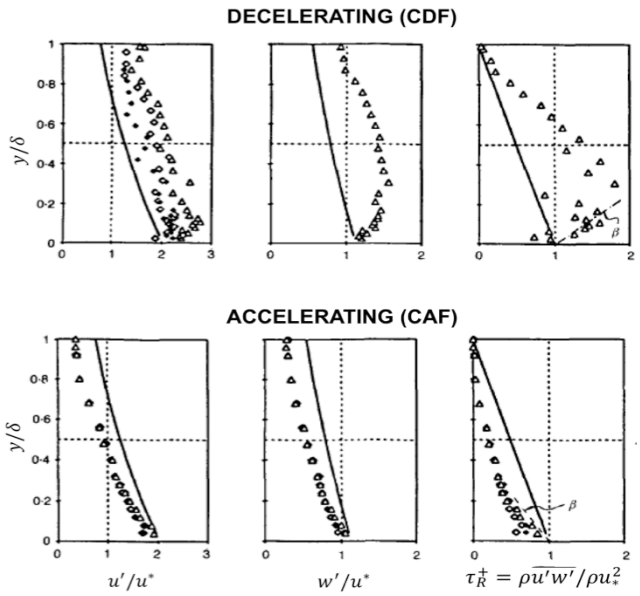

Figure 5: Turbulence intensities and Reynolds stresses for decelerating flow (top) and accelerating flow (bottom). Modified from Kironoto and Graf (1995).

MacVicar and Rennie (2012) expanded the understanding of turbulence distribution in accelerating and decelerating flows using a laboratory flume with a straight pool with fully turbulent, subcritical flows. Increased turbulence intensities and τ_R values were noted in the CDF zone, as well as lateral convergence of the flow, producing a 'core' of high velocities toward the centre of the pool above the bed and decreased velocities in the near-bed region. The result of this 'core' was large turbulent sweeps ($u' > 0, w' < 0$) directed toward the sidewalls of the flume. At the downstream end of the pool in the

CAF zone, flows diverged outward toward the flume walls along with an increase in the near-bed velocities (Figure 6).

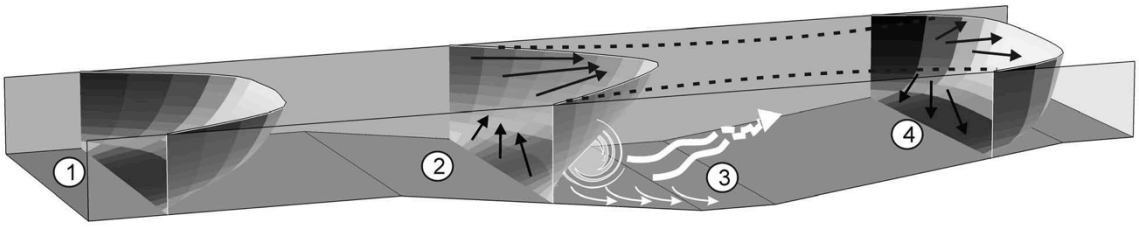

Figure 6: Turbulence distribution in a pool. Black arrows indicate mean velocity vectors and white arrows indicate turbulence produced in the CDF zone. (MacVicar and Rennie, 2012)

Within the CDF zone, turbulent sweeps act toward the sidewalls in the pool head zone and are hypothesized to strengthen the effect of the 'core'. This effect produces a feedback mechanism of higher turbulence intensities at the pool head and increased near-bed CAF at the tail of the pool. These complex interactions may provide an improved understanding of the formation, self-maintenance and particle sorting within pools. More generally, this research demonstrates the complex, turbulent conditions present in non-uniform flows that must be accounted for to accurately estimate the mobility of sediment particles as well as the overall sediment transport rate.

2.5 Research Gaps

Sediment transport remains an active area of research. Recent studies focusing on the role of turbulence in estimating sediment mobility, especially in non-uniform flows, represent an important advancement. The difficulty in collecting high-precision simultaneous measurement of fluid velocities and particle location continues to be a significant barrier to understanding the precise mechanics of sediment mobility. The ability to identify the precise hydraulic conditions that cause an individual particle to become mobile has eluded researchers for decades. The development and testing of the concept of impulse indicates a potentially pivotal advancement in sediment transport studies. The work completed by Diplas et al (2008) and Celik et al (2010) offers a promising parameter for examining the direct link between hydrodynamic conditions and particle mobility. Several opportunities for advancement are available for building on the work of these researchers. Firstly, the spatial distribution of impulse events within a non-uniform bed has not been examined. Secondly, the experimental set up of Diplas et al (2008) and Celik et al (2010) used a

laser-based instrument to detect the precise instant of particle movement. Therefore, no information regarding the trajectory or mode of entrainment of a transported particle can be ascertained using this set up. New experimental approaches are required in an effort to fill these important research gaps. Velocity profiling instruments, such as the VII, offer a promising method for collecting high-resolution three-dimensional velocities in the near bed region, but require testing to confirm their suitability in turbulence studies. As will be discussed in Chapter 3, new data filtering programs are required for spike detection, replacement and cell quality classification to ensure that high quality time series are available for subsequent analysis. The use of image analysis in tracking sediment particles is seen as a promising approach, but no standardized tracking program is readily available for the nature of laboratory experiments required. Therefore, the development of an automated tracking program for possible synchronization with the VII is required and will be discussed in Chapter 5.

Chapter 3
DESPIKING VELOCIMETRIC DATA USING 2D ARMA MODELS

**This chapter is written as an original article that is proposed for submission to an academic journal in the field of sediment transport or fluid mechanics.*

3.1 Introduction

Velocity profiling instruments capable of measuring high-resolution, three-dimensional fluid velocities have greatly advanced hydrodynamic studies. The ability to record velocities at sufficiently high spatiotemporal resolutions enables the measurement of turbulence at the scale it is generated and dissipated. Ultrasonic Doppler velocity profilers (e.g., MetFlow's UVP-DUO™) and acoustic Doppler velocity profilers (e.g., Nortek AS's Vectrino II™ and SonTek's ADP) calculate fluid velocities by measuring the Doppler shift of acoustic backscatter in the fluid. In turbulent flows, a wide range of differently sized coherent structures may span multiple sampling cells and persist for long durations. The passage of these coherent structures through the sampling column is expected to be associated with highly correlated time series in adjacent cells, whereas cells separated by increasing spatial distances are expected to be less correlated. Similarly, low sampling frequencies reduce the correlation between consecutive velocities, particularly if the sampling frequency is larger than the smallest scales of turbulence (Lane et al, 1998). An inherent consequence of Doppler-based velocity measurements is the inclusion of noise within the velocity signal arising from many sources including: Doppler white noise, velocity ambiguity (aliasing), shear stresses within sampling volumes and the effect of micro-scale turbulence (Hurther and Lemmin, 2001). Excessive noise and erroneous spikes in a velocity time series can cause bias in the mean and turbulence statistics (Cea et al, 2007). Filtering algorithms are required to classify the data quality and to detect and replace spikes in each cell.

The filtering of velocimetric data collected by profiling instruments requires three separate, but interrelated steps: spike detection, spike replacement and cell quality classification. Many approaches are available for each of these steps but may perform poorly due to inherent limitations and drawbacks. Firstly, erroneous spikes can be detected in the time series using a detection algorithm such as: minimum/maximum threshold, acceleration threshold (Cea et al, 2007), phase-space threshold (Goring and Nikora, 2002) and a wavelet packet decomposition approach (Razaz and Kawanisi, 2011). These

approaches are discussed in greater detail below. Four main limitations are noted with these detection methods: (1) with the exception of wavelet package decomposition, neither the spatial nor temporal location of a spike within the time series are considered; (2) the cutoff parameters are a function of the data being despiked and the number of required iterations and updates to the cutoff parameter are poorly defined; (3) detection and replacement of spikes are decoupled from each other; no information used in spike detection is transferred to the replacement procedure; (4) despiking is completed for a single time series in isolation of adjacent cells. With the prevalence of high spatiotemporal resolution profilers and the coherent structure of turbulence, valuable information within the time series is being unused. Secondly, after a spike is detected the problem becomes how to handle it. In most filtering methods, replacement is seen to be of secondary importance to detection. Typically, replacement is completed with simple arithmetic calculations using observations in the immediate temporal vicinity of the spike (Razaz and Kawanisi, 2011). This is noted to cause a reduction in the representative variance of the time series. While this consequence may be negligible when replacing a small number of spikes, it may unduly affect the estimation of turbulent statistics when a large number of observations are replaced (Lane et al, 1998). Lastly, the quality of data in the sampling cells must be classified to determine that a recorded time series meets minimum quality requirements and is approximately representative of the fluid velocities. Common classification methods include: cell location within sampling column, signal correlation, noise intensity, number of detected spikes and cross-correlation between adjacent cells (Lane et al, 1998; Hurther and Lemmin, 2001; Cea et al, 2007). With the exception of the final method, these methods rely solely on information within an individual cell and do not make use of data in adjacent cells. Cross-correlation between adjacent cells provides a simple estimate of the similarity between these cells, but is perceived to only make limited use of available data that can assist in classifying data quality.

The use of high-frequency and high-spatial density sampling instruments in turbulence studies produce highly correlated velocity signals in the temporal and spatial domains. Spatial correlations exist between adjacent sampling cells when coherent turbulent structures span multiple sampling cells. Similarly, temporal correlations are produced when a coherent structure persists for multiple observations within a time series. A method for quantitatively describing the velocity signals specifically using these correlative properties is offered by autoregressive moving average (ARMA) models. These models offer a parsimonious description of linear, stochastic processes using a set of autoregressive (AR) and moving average (MA) coefficients and a white noise term. Models are denoted by $ARMA(p,q)$ where p is the order of the AR component and q is the order of the MA component. The AR terms describe the linear

dependence of p preceding (herein referred to as 'lagged') observations on a current observation and the MA component describes the dependence of q lagged error terms on a current observation. Unlike other filtering approaches, ARMA models can describe and explain the velocity signal and account for the natural variance that is present due to turbulent fluctuations. Within this study the use of ARMA models were examined for quantitatively describing a time series and aiding in the filtering of data. An analysis of model coefficients in the filtering of velocimetric data is discussed, including the role of turbulence scales and sampling location.

The aim of the current research was to develop a new method for filtering high-resolution data from profiling instruments using ARMA models. A series of new algorithms, written in Matlab™, are described and illustrative results are provided. The algorithms were designed to perform the three interrelated tasks of spike detection, spike replacement and cell quality classification. The criteria for the method were that:

1. Spike replacement must preserve the statistical properties of the representative data
2. Spike detection must have a cutoff parameter that is independent of the data itself
3. Spike detection, replacement and cell quality classification must be coupled together

This chapter is organized to provide a background discussion of velocity profiling instrument technology and limitations of available algorithms for spike detection, spike replacement and cell quality classification. The methods section discusses ARMA model selection and fitting, spike detection, spike replacement, classifying cell quality, additional data quality considerations that were required to address unique situations and the experimental procedure for data collection is discussed. Illustrative results of the filtering algorithms are presented and discussed.

3.2 Background

3.2.1 Velocity profiling instrumentation

Acoustic Doppler velocity profiling (ADVP) instruments have become commonplace in laboratory-scale hydrodynamic studies requiring high-resolution measurement of fluid velocities. These instruments are capable of measuring three-dimensional velocities over a sampling profile and are well suited for laboratory-scale hydrodynamic studies requiring high-resolution measurement of fluid velocities. Such

instruments, including the Vectrino II (VII), calculate fluid velocities by transmitting acoustic pulses from the central transmitter and measuring the Doppler shift of the backscattered signal picked up by four receiver probes. For the VII, velocities are collected for a series of sampling bins (herein called 'cells') within the sampling column at a frequency of up to 100 Hz. Cell sizes within the sampling column are adjustable from 1 to 4 mm to produce a sampling column up to a maximum of 35 mm high (Figure 7).

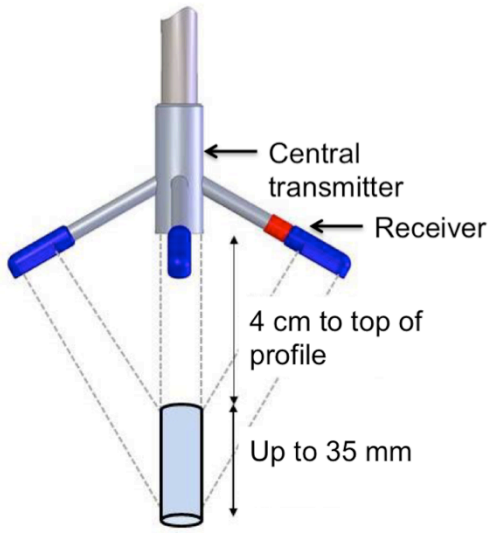

Figure 7: Vectrino II probe head (Nortek AS, 2013)

An inherent drawback of the VII is that the signal strength is not constant over the full 35 mm sampling profile. The signal-to-noise ratio (SNR) provides an estimate of the signal strength within each sampling cell and is roughly parabolic over the sampling range, extending from approximately 40 mm to 75 mm below the central transmitter. Due to the geometry of the transmitter probes, a so-called 'sweet spot' is created at approximately 50 mm below the central transmitter, where peak SNR values occur and data quality is typically at its maximum (Nortek AS, 2012). A range of good quality data is centered around the 'sweet spot' and extends from approximately 40 mm to 65 mm below the central transmitter. Cells at the extremities of the sampling profile are more likely to be removed from the data set due to being poor quality, contain a large number of spikes or not representative of the measured hydraulic conditions.

In addition to measuring three-dimensional fluid velocities, the VII also offers a bottom depth measurement feature with a sampling frequency of up to 10 Hz. This feature uses acoustic signals to

estimate the distance between the central transmitter and a bottom surface, to a maximum of 0.35 m (Nortek AS, 2013). The bottom depth is estimated as the surface with the strongest reflected signal and is generally associated with the first solid surface encountered by the transmitted pulses.

3.2.2 Spike detection

For all filtering methods and flow regimes discussed in this chapter, the velocity time series are assumed to be i) nonseasonal (lack cyclical variations over measurement duration) ii) homoscedastic (constant variance over time) iii) no persistence (no external shocks or disturbances) and iv) stationary over the duration of the time series (constant mean and variance over time). Four common methods are considered for the detection of spikes:

1. Minimum/maximum threshold (Cea et al, 2007):

$$u_{min} = \bar{u} - \sqrt{2\ln N}\sigma_u \tag{18}$$

$$u_{max} = \bar{u} + \sqrt{2\ln N}\sigma_u \tag{19}$$

where $u_{\min}$ and $u_{\max}$ are the minimum and maximum thresholds are defined using the mean velocity ($\bar{u}$), standard deviation (σ), total number of observations in the time series (N) and the streamwise velocity component (u). Data falling outside of the defined range are considered erroneous and replaced in a separate algorithm.

2. Acceleration threshold (Cea et al, 2007) using:

$$a_{x,i} > k_g g \; and \; u_i > \bar{u} + k_\sigma \sigma_u \tag{20}$$

$$a_{x,i} < -k_g g \; and \; u_i < \bar{u} + k_\sigma \sigma_u \tag{21}$$

The acceleration of a particle in the flow is calculated as $a_i = (u_i - u_{i-1})/\Delta t$ with the maximum acceleration of a particle assumed to be proportional to, and the same order of magnitude as, gravitational acceleration given by $a_{max} = k_g g$. Constants k_g and k_σ are defined by the user with suggested calculation methods provided by Cea et al (2007) and Goring and Nikora (2002).

3. The most common method for spike detection is phase-space threshold as developed by Goring and Nikora (2002) (referred to as 'GN'):

$$\lambda_u \sigma = \sqrt{2lnN}\sigma \tag{22}$$

where λ_u is the universal threshold and is used to calculate the length and orientation of the axes defined by the raw data, first and second derivatives in a three-dimensional ellipsoidal cloud. All data within the limits of the cloud are considered good quality and those outside are considered to be spikes. The universal threshold is updated at the beginning of each iteration with the user defining the maximum number of iterations.

4. A detection method developed by Razaz and Kawanisi (2011) using wavelet packet decomposition to improve the spatial and temporal detection of spikes. An alternative method of calculating the universal threshold where d_i is the wavelet basis is given by:

$$\lambda_u \sigma = 1.4826\langle \left| d_{1,i} - \bar{d} \right| \rangle_i \sqrt{2lnN} \tag{23}$$

3.2.3 Spike replacement

For a single-point spike detected at observation *i* in the time series *u*, common replacement methods include (Goring and Nikora, 2002; Razaz and Kawanisi, 2011):

- Replace with preceding good data point, $u_i = u_{i-1}$
- Replace with two preceding data points, $u_i = 2u_{i-1} - u_{i-2}$
- Linear interpolation across spike, $u_i = (u_{i-1} + u_{i+1})/2$
- Replace with the mean of signal, $\bar{u}$
- Smoothed estimate using a third-order polynomial
- Best linear predictor using autoregressive models

The first three methods have the undesirable effect of reducing the representative variance in a time series. The fourth technique, replacement with the mean, can produce new spikes during localized departures from the mean (Lane et al, 1998). The fifth technique, using a polynomial, has been noted to generate deep troughs in the time series that are not in visual agreement with the local velocities (Razaz and Kawanisi, 2011). The final method, proposed by Razaz and Kawanisi (2011), fits a parsimonious

model to the 60 observations preceding a detected spike and uses the best linear predictor method (minimum mean squared error) to generate a replacement value at the erroneous observation. While this method is seen as a significant advancement in improving the justifiability of replacement values, the model order is variable and must be determined before each replacement, resulting in a lack of computational efficiency and inconsistency in the replacement algorithm. Additionally, as with the other methods, the detection and replacement are decoupled from each other.

Several existing replacement options for grouped spikes were considered, including:

- Replacement across the spike with a single estimated value
- Step-by-step forecasts across each observation within the spike
- Generation of synthetic velocity time series for flagged observations

Replacement with a constant value has been noted to produce a flattening of the velocity signal and therefore adversely affects the estimation of turbulence statistics (Goring and Nikora, 2002). Step-by-step forecasting relies on replaced values to generate new replacement estimates and potentially magnifies the uncertainty in generating replacement values. The use of synthetically generated data is promising, provided that replacement terms include a random noise term based on the local velocity signal. Failure to adequately account for representative noise in the signal has been noted to produce a relatively smooth set of replacement values that can reduce the variance in the signal (Razaz and Kawanisi, 2011).

3.2.4 Cell quality classification

Several existing methods are available for classifying cell quality, including:

1. Cell range – sampling cells at the upper and lower extremities of the profiling array generally have lower SNR values, of lower quality and may be eliminated from analysis.
2. Signal correlation – the Doppler shift of successive acoustic pulses are expected to be highly correlated. The correlation of these signals can be used to provide an indication of data quality. Lane et al (1998) recommends a threshold of at least 70% for the average correlation in a time series or that each correlation value must be greater than this threshold.
3. Cross-correlation between adjacent cells – adjacent sampling cells are expected to be highly correlated due to the spatiotemporal coherent structure of turbulence. The cross-correlation of the velocity signals in adjacent cells can be used to evaluate data quality within the cells.

4. Signal noise using redundant vertical velocity profiles – for instruments with two simultaneously measured vertical velocity signals, the noise between the two signals can be used as an indication of data quality (Hurther and Lemmin, 2001).
5. Detected spikes threshold – the number of detected spikes within a time series can be used as an indication of cell quality. The replacement of a large number of observations causes measured velocities to be replaced with synthetic data and thereby reduces the representativeness of the time series.

3.2.5 Autoregressive Moving Average (ARMA) models

ARMA models were popularized by the work of Box and Jenkins (1976), and have been extensively used in modeling economic trends and hydrological processes (Hipel and McLeod, 1994), but their use in hydrodynamic studies has been extremely limited. ARMA models describe a current observation as a function of preceding observations and error terms as well as a white noise term. A modeled velocity using a general ARMA(*p,q*) model is given by:

$$y_t = \emptyset_1 y_{t-1} + \emptyset_2 y_{t-2} + \cdots + \emptyset_p y_{t-p} + \theta_1 a_{t-1} + \theta_2 a_{t-2} + \cdots + \theta_q a_{t-q} + a_t \qquad (24)$$

Where y_t is the velocity at time *t*, $\emptyset_1, \emptyset_2, \ldots, \emptyset_p$, are the AR parameters at *lag 1, lag 2, ..., lag p* and $\theta_1, \theta_2, \ldots, \theta_q$ are the MA parameters at *lag 1, lag 2, ... , lag q* represents the random error term at observation *t*. The random error or residual, a_t, at each observation represents the difference between the recorded velocity and the expected value calculated by the ARMA model. A pure AR model is indicated by setting *q* to zero to generate an ARMA(*p*,0) or AR(*p*) model. Similarly, a pure MA model, ARMA(*0,q*) or MA(*q*) is produced by setting *p* to zero.

In the study of dune formation in sand beds, Yalin (1972) notes an attenuating oscillatory pattern in the turbulent velocity signal and a corresponding dampening effect in the autocorrelation function, corresponding to a pure AR model with a small number of coefficients. Clifford et al (1992) notes a second order AR model, AR(2), is most statistically appropriate for describing turbulent velocities at a small distance above a coarse gravel bed of a riffle pool sequence. In other words, each current observation can be most parsimoniously described as a function of the two proceeding observations and a white noise term. An AR(2) model is given by:

$$y_t = \emptyset_1 y_{t-1} + \emptyset_2 y_{t-2} + a_t \qquad (25)$$

Where y_t is the velocity observation at time *t*, $\emptyset_1$, $\emptyset_2$ are the AR parameters at lag 1 and lag 2, and a_t is a white noise error term at observation *t*. Richards (1979) and Robert et al (1993) considered the application of AR(2) models for describing a velocity time series and observed a pseudo-oscillatory relationship given by:

$$\emptyset_1^2 < -4\emptyset_2 \tag{26}$$

This pseudo-oscillatory relationship produces a linear trend and an upper boundary between the $\emptyset_1$ and $\emptyset_2$ coefficients, as seen in Figure 8.

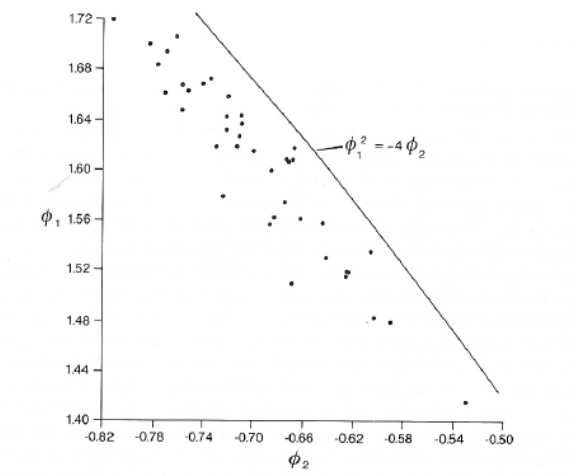

Figure 8: Pseudo-oscillatory relationship between ϕ1 and ϕ2 coefficients (Robert et al, 1993)

3.3 Methods

The developed methodology for filtering velocimetric data is comprised of four steps: pre-screening data for minimum quality requirements, spike detection, spike replacement and cell quality classification. With the exception of pre-screening all steps use ARMA models. The methods are designed for velocity profiling instruments with high-density sampling resolutions where neighboring sampling cells are within tight spatial densities (e.g., 1 mm for the VII). The overall progression through the filtering program is shown in the flowchart in Figure 9. Detailed discussion of algorithm steps are provided in the following sections.

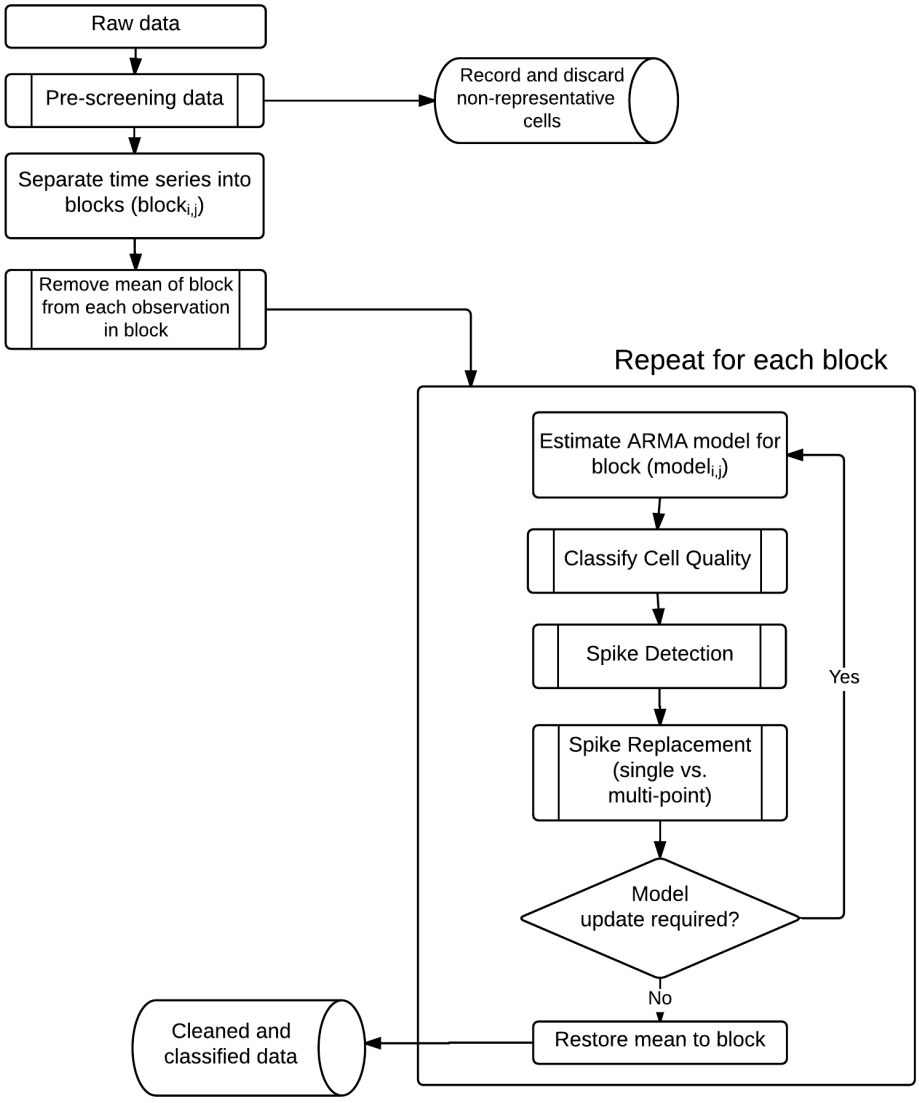

Figure 9: Overall sequence of filtering algorithm

3.3.1 Pre-screening data

To avoid fitting an ARMA model to exceedingly poor quality data that is not representative of a velocity signal and of no practical value to despiking, a preliminary filtering step was developed to ensure minimum quality requirements are met. The need for this step was identified in response to 'corrupted' velocity signals where a single velocity value erroneously persists for many observations. Figure 10

illustrates this occurrence where velocities in a sampling cell slightly above the bed equal to exactly 0.0 m/s ten times more commonly than any other velocity value. Additionally, the mean of this cell is significantly less than in any nearby cell. This phenomenon appears to be associated with a combination of low SNR values, cells at the extremities of the sampling profile and cells in the inner layer of the flow.

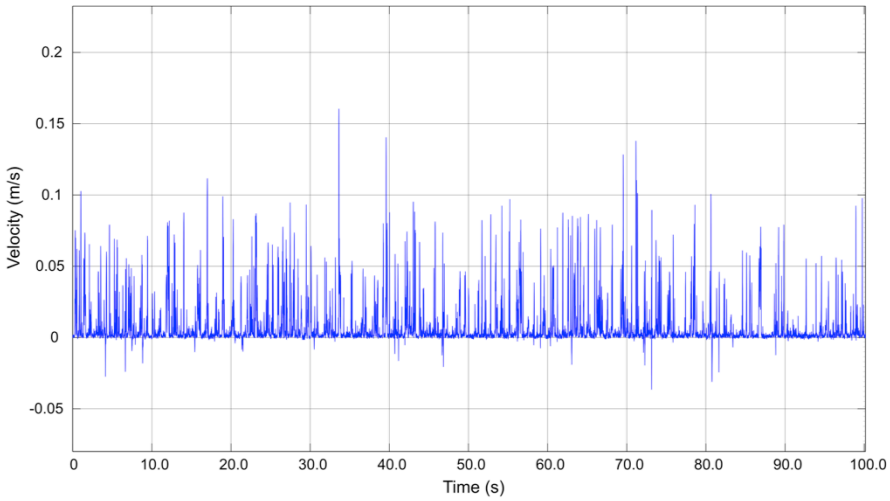

Figure 10: Corrupted velocity signal

To account for such occurrences, a simple algorithm compares the percentage of recorded velocities that share the exact value of the mode to a user-definable maximum threshold, C_{mode}. If C_{mode} is exceeded then the entire cell is flagged as unsuitable for fitting an ARMA model and excluded from further analysis. A description of all variables and coefficients and recommended values used in this chapter are provided in Table 1.

3.3.2 General application of ARMA models

The four velocity components (streamwise, lateral and redundant vertical profiles) are independently filtered using ARMA models. Each time series is broken into sets of smaller segments (herein called "blocks") and the mean is removed from each observation in the block. The number of observations in each block is given by C_{LB}. The block number is given by i (i = 1, 2, 3 … N_{blocks}) and the sampling cell number is given by j (j = 1, 2, 3 … N_{cells}). An individual block of data is indicated by $block_{i,j}$ and the ARMA model estimated for each block is given by $model_{i,j}$. The first block for all cells ($block_{1,1}$ to

$block_{1,Ncells}$) is fully despiked before advancing to the second block for all cells ($block_{2,1}$ to $block_{2,Ncells}$), and so on until the final block for the final cell is reached.

The construction of an ARMA model consists of three steps: determining the model order, estimating model coefficients, and confirming the fit using diagnostic checks (Hipel et al, 1977). To determine the model order, an autocorrelation function (ACF) and partial autocorrelation function (PACF) can be used. An ACF describes the linear dependence between lagged observations in a time series. Similarly, the PACF measures the linear dependence between the error terms at lagged observations. For a pure AR(p) model to be valid, the PACF must truncate after p lags to below a defined confidence interval and the ACF must gradually attenuate for a large number of lags. The use of an AR(p) model indicates that each velocity value can be adequately described as a linear function of a limited number of preceding observations, plus a white noise term, a_t, to account for random noise in the signal. For a pure MA(q) model to be valid, the converse conditions must be true with the ACF truncating and the PACF gradually attenuating. After the model order is determined, model coefficients are estimated using maximum likelihood techniques such that the mean-squared error (MSE) is minimized. Computer software packages, such as Matlab™ and R™, offer built-in computationally efficient commands for estimating the optimal values for model coefficients. For the selected model order and coefficients to be valid, residuals must be independent, homoscedastic, normally distributed and exhibit no seasonality (Hipel et al, 1977). The residual autocorrelation function (RACF) offers a simple, but effective method for examining the whiteness of model residuals, by plotting the ACF of the model residuals calculated using the estimated model. If these requirements are not adequately met, a more complex model or transformations of the data may be required (Hipel et al, 1997; Box and Jenkins 1976). In the interest of model parsimony, computational efficiency and the ability to analyze model coefficients it is desirable to identify a single model order that can be consistently used throughout the filtering algorithm for all velocity components under a wide range flow conditions. Therefore, the goal of diagnostic checking for this method is to confirm the *general* validity of the selected model order and associated coefficients.

To determine the model order for the velocity data collected in this study, an illustrative example of the ACF and PACF are provided for a representative segment of data, $block_{1,5}$. This block of data was collected downstream of an increase in the flow depth, over a rough bed and in the near-bed environment. The ACFs for the streamwise (X), lateral (Y) and redundant vertical velocities (Z1 and Z2) are provided (Figure 11).

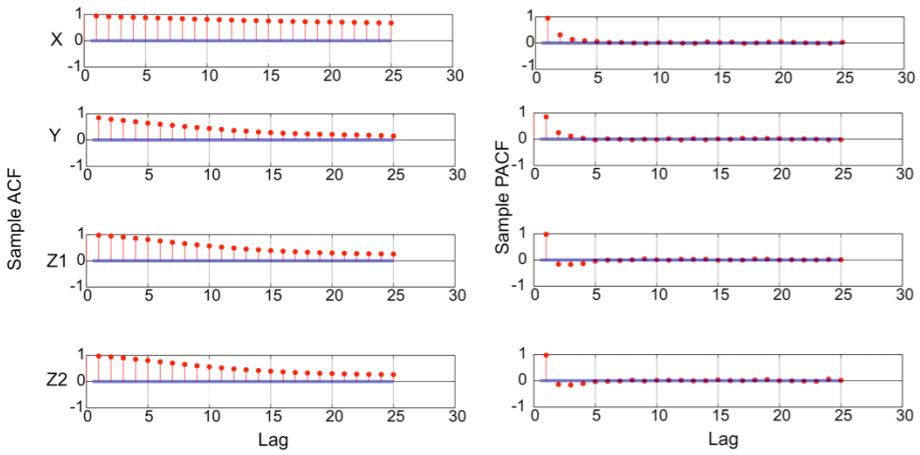

Figure 11: ACF (left) and PACF (right) for u, v, Z1 and Z2 velocity components

For all velocity components in the above figure, the ACFs gradually attenuate and the PACFs truncate after a small number of lags. Although there is minor variability, general agreement with an AR(2) model is established. The RACF of the residuals (Figure 12) is calculated using the AR(2) model for the streamwise velocities in block$_{1,5}$ and indicates a lack of seasonality and independence of the residuals, thereby confirming the model order selection.

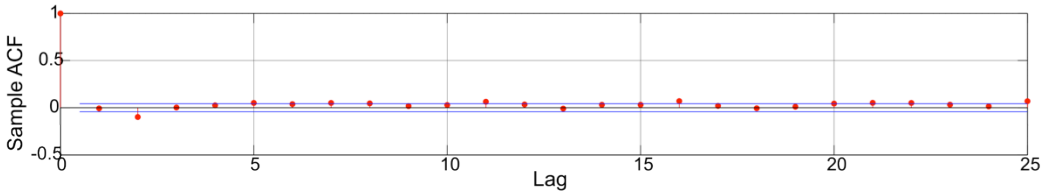

Figure 12: RACF for streamwise velocity component

Therefore, AR(2) models are assumed to be valid for modeling the velocimetric data available in this study.

3.3.3 Spike detection

A properly estimated ARMA model for each block of data is expected to provide a high-quality description of the data with approximately half of the estimated y_t values being nominally greater than the

recorded velocity and the other half being nominally lower. Spikes in the data are indicated by locations where the expected velocity estimated by $model_{i,j}$ is significantly different than the recorded velocity, which produces a large residual value. In other words, large residuals indicate a significant departure from the expected value estimated using the lagged observations. The coherent structure of turbulence appears as spatial correlations between adjacent time series and as temporal correlation within a time series. Therefore, when the model for a given block is applied to data in a spatially adjacent block, the residuals at each observation are expected to be nearly identical. The ARMA models for the adjacent upper and adjacent lower cells ($model_{i,j-1}$ and $model_{i,j+1}$, respectively) are used in conjunction with the model developed for the target cell ($model_{i,j}$), thereby providing up to three measurements of the residuals at each observation in the target time series, $block_{i,j}$. Both single point and multipoint spikes can be detected using the developed procedure.

For a properly fit model and a block of data with no spikes present, all residuals are expected to be small and approximately normally distributed. A large residual will cause a departure from the assumption of normally distributed residuals due to a large value in one of the tails of the distribution. Using this information, it was hypothesized that the kurtosis of the model residuals would be a reliable and consistent indicator of spikes within the data. Kurtosis is the fourth-order moment of a data set and describes the shape of the peak and size of the tails in a distribution, with a normal distribution having a kurtosis of three. The use of kurtosis in outlier detection, especially in velocimetric data, has been extremely limited (Ferguson, 1961; Kelley et al, 1992). However its use is promising since it is computationally simple and allows the representative randomness in a turbulent time series to be preserved. A similar method for detecting spikes in a raw data sets using the third-order moment, skewness, has been proposed by Heymann et al (2012), but does not address the problem of replacement.

The developed spike detection procedure using ARMA models and kurtosis of the residuals is described below and outlined in the illustrative flowchart in Figure 13.

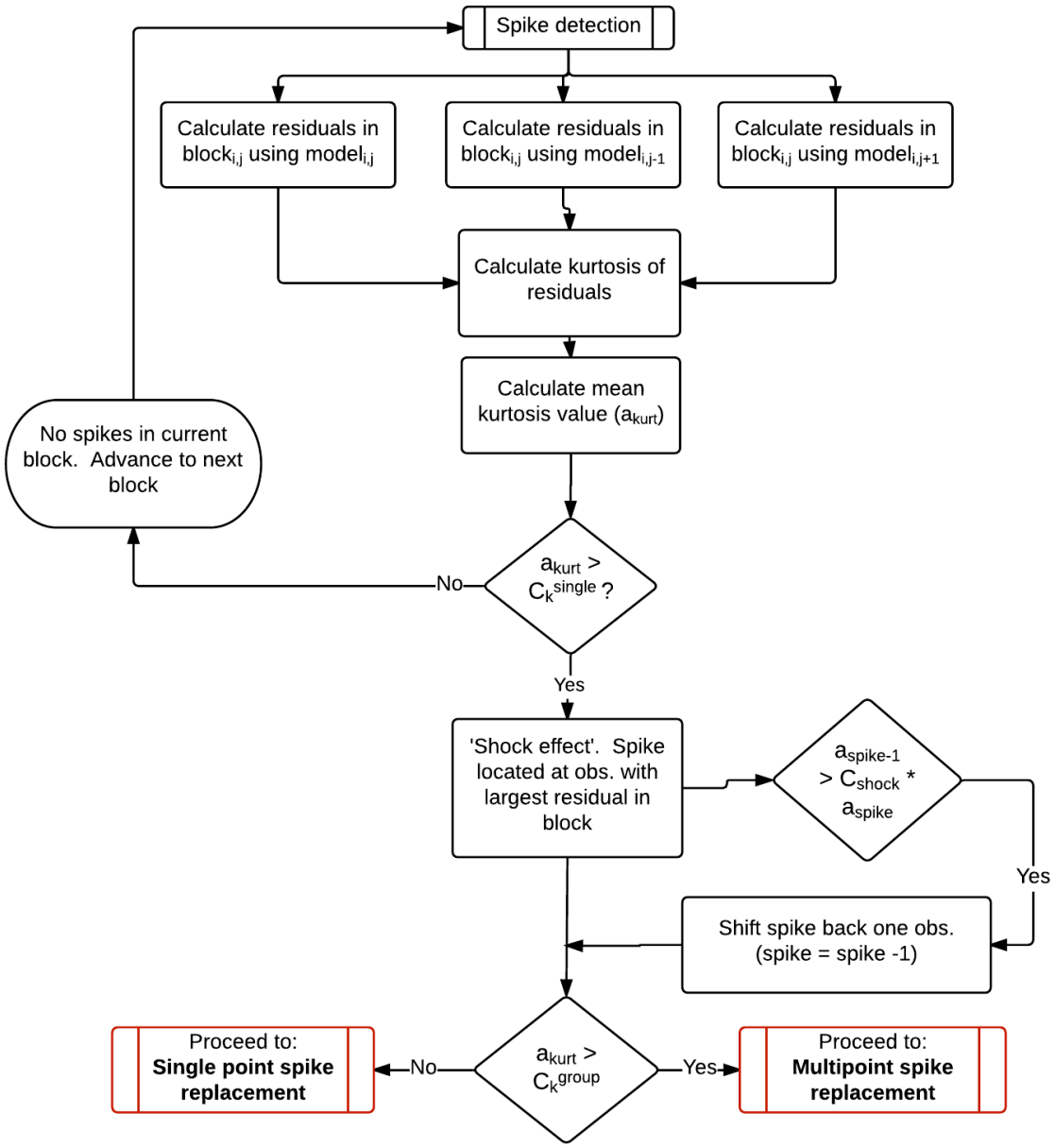

Figure 13: Spike detection sequence

Using the calculated kurtosis value of the model residuals, a preliminary estimate of the type of spike present (single or multipoint) is made, with large kurtosis values potentially associated with multipoint spikes. Spikes are detected and replaced until the kurtosis is iteratively reduced below a cutoff threshold.

Separate algorithms are used to determine the spike location and replacement values. For example, detecting spikes in the first block of data for cell 5 ($block_{1,5}$) would proceed as follows:

1. Calculate residuals ($a_{1,5}$) at each velocity value in using $model_{1,5}$.
2. Where available, calculate residuals ($a_{1,4}$) using upper adjacent $model_{1,4}$.
3. Where available, calculate residuals ($a_{1,6}$) using lower adjacent $model_{1,6}$.
4. Calculate the mean kurtosis value of residuals, a_{kurt}, as the mean of $a_{1,5}$, $a_{1,4}$ and $a_{1,6}$.
5. If a_{kurt} is less than C_k^{single} then no spikes are present in the current block; advance to $block_{1,6}$ and return to the first step. If a_{kurt} exceeds C_k^{group}, check for possible multipoint spike. Otherwise, a single point spike is assumed to be present.

When $C_k^{single} < a_{kurt} < C_k^{group}$ a single point spike is initially assumed to be present in the block. In the vast majority of cases, the spike is located at the observation with the largest magnitude residual. However, it has been observed that specific combinations of ϕ_1, ϕ_2 and lagged velocity terms (including the true large magnitude spike) may generate a larger residual term at the observation immediately after a spike, rather than at the true spike. To overcome the possibility of this scenario (referred to as 'shock effect' in the flowchart) a test has been added to the proposed procedure: if the residual at the observation immediately before the detected spike is within at least a given threshold percentage (C_{shock}) of the detected maximum residual, then the spike location is shifted back in time to the earlier large residual. Replacement of the spike is then handled through the appropriate replacement algorithm.

When a multipoint spikes is present in a block of data, a_{kurt} is generally very large. Therefore, testing for the presence of a multipoint spike is completed when kurtosis exceeds C_k^{group}. A multipoint spike, or grouped spike, occurs when at least two successive observations are considered spikes and is indicated by two large magnitude residuals with opposite signs indicating the limits of the group. For example, when a good quality velocity signal abruptly enters a large, negative magnitude grouped spike (Figure 14), a large negative residual is produced at the first observation in the group.

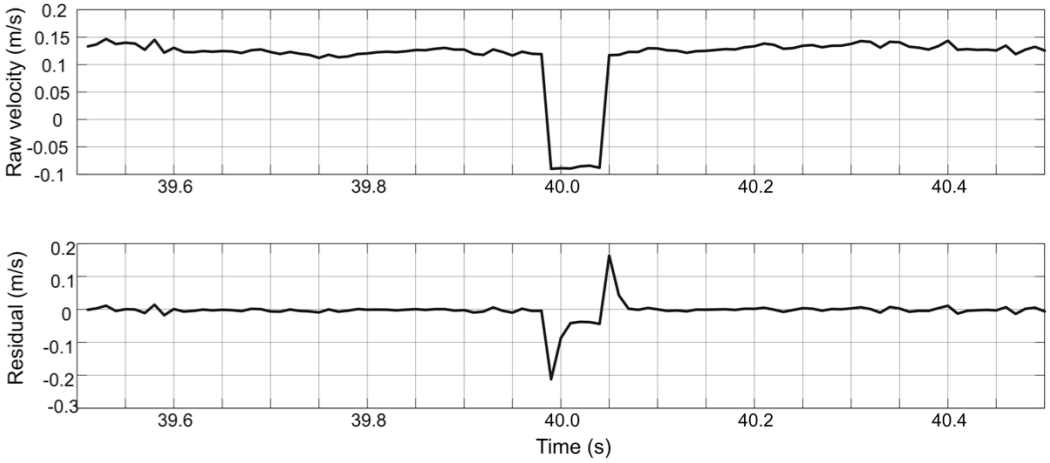

Figure 14: Multipoint spike (top) and corresponding residuals (bottom)

For the first good quality observation immediately after spike (at time 40.05 seconds), a large positive magnitude residual is calculated. Once the location of the largest magnitude residual is determined, the algorithm scans the residuals in the temporal vicinity (to a maximum of C_{scan} observations) of the spike for a comparably large oppositely signed residual that is within a defined percentage, C_a^{group}, of the maximum detected residual. If such a residual is found, then the observations between the oppositely signed residuals are flagged as members of a multipoint spike and replaced with the multipoint replacement algorithm discussed below. If such a residual is not found, then no grouped spike is present and the algorithm reverts to replacement as per the single point spike method.

3.3.4 Spike replacement

The replacement value for a single point spike is assumed to equal the best linear predictor estimated using the estimated ARMA model. Simply put, a spike is replaced with a value such that the error term is eliminated. Details of the procedure for both single point and multipoint spikes are outlined in the flowchart in Figure 15.

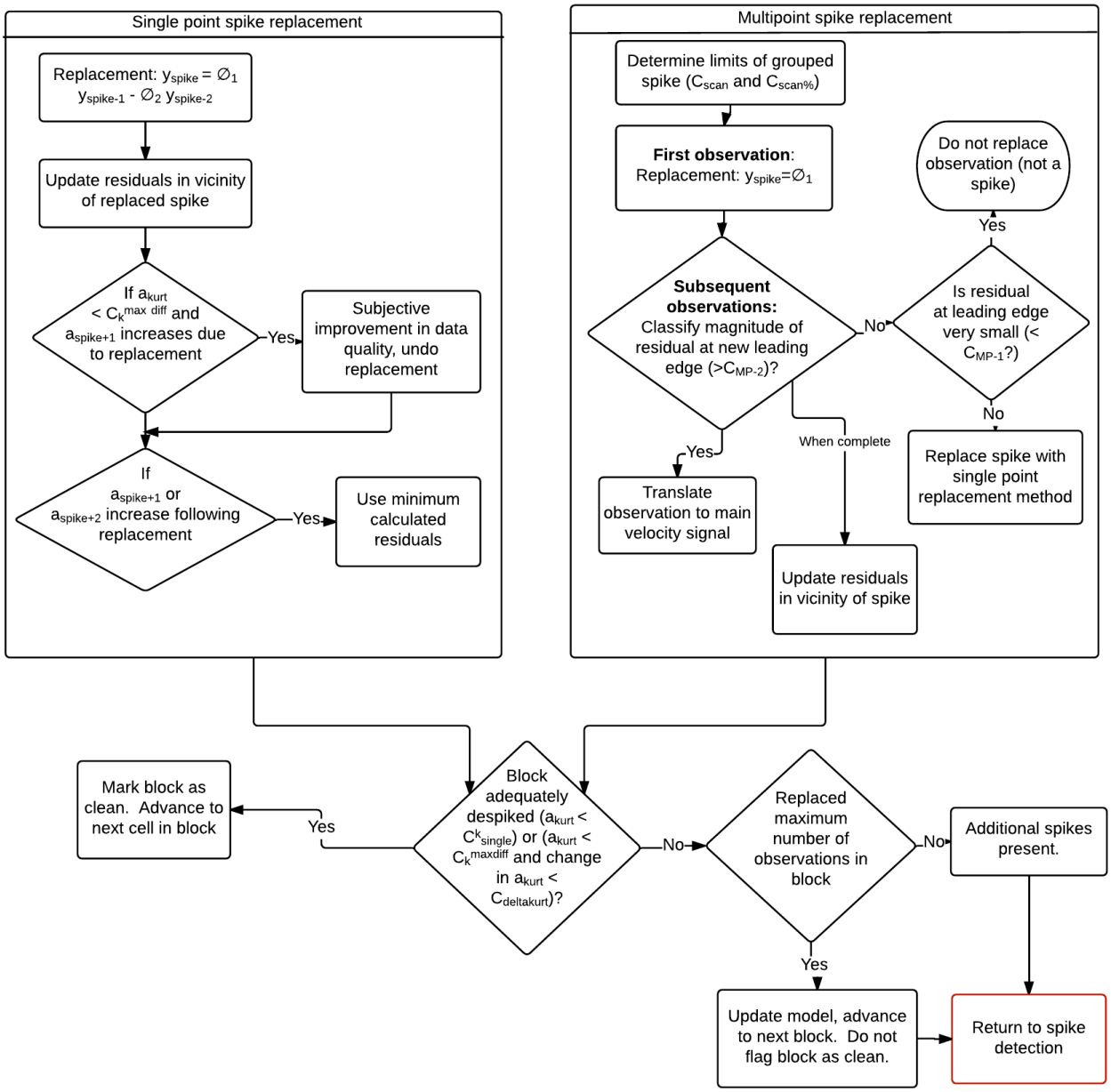

Figure 15: Spike replacement sequence

For a general AR(2) model the replacement value is estimated using the lagged velocity terms and $\emptyset_1$ and $\emptyset_2$ coefficients such that:

$$y_t = \emptyset_1 y_{t-1} - \emptyset_2 y_{t-2} \quad (27)$$

The inclusion of a white noise term has not been deemed necessary for estimating the replacement value. However, future version of the algorithm can be modified to include an option for the user to decide if an a_t term should be included. It is expected that a_t would be normally distributed.

Existing replacement options for multi-point spikes were deemed inadequate. A new method, translation to the main velocity signal, is hypothesized to be a promising method. This method assumes that data within the grouped spike provides a reasonable starting point for estimating replacement values within the group. This hypothesis is based on observed phase-wrapped data where the velocity signal is abruptly and distinctly translated by an approximately constant magnitude from the main signal. Representative information about the true velocity signal, especially the differences between successive velocities, is contained within phase-wrapped data. Using this method, the first observation at the 'leading edge' of the spike is replaced using the same procedure as a single point spike since lagged observations are assumed to be of high quality. For subsequent observations in the spike, it is hypothesized that there is valuable information contained within the group. The original residual at the original leading edge, given by $a_{MP-lead}$, is used as a threshold for determining which subsequent observations within the grouped spike provide potentially valuable information for replacement. The new leading edge of the multipoint spike is incrementally replaced and the residuals are updated after each iteration. When the residual at the new leading edge is within a threshold percentage, C_{MP-2} (defined as a large percentage of $a_{MP-lead}$), the observation is translated to the main velocity signal by a value equal to $a_{MP-lead}$. When the residual at the new leading edge is less than C_{MP-1} (defined as a small percentage of $a_{MP-lead}$), the original velocity value is considered acceptable and no replacement is required. If the residual at the new leading edge is between C_{MP-1} and C_{MP-2}, replacement of the observation is required but the original recorded velocity offers no valuable information and is replaced with the method used for a single point spike. Once all members of the grouped spike have been replaced, the kurtosis of the residuals is recalculated and the presence of additional spikes, including within the recently replaced multipoint spike, are tested until the kurtosis within the block is reduced to below C_k^{single}.

3.3.5 Cell quality classification

A cell quality classification procedure was developed using ARMA models. This procedure is based on the assumption that the velocity time series for sampling cells in close proximity should be highly correlated due to the spatiotemporal coherent structure of turbulence. It is hypothesized that block of data

in a time series can be reasonably described by the models for the blocks immediately above and below the given cell. Therefore, when a model from an adjacent block is applied to the data in a target cell, the estimated residuals are expected to be similar to the residuals estimated using the model developed for the target cell. An abrupt increase in the residuals may indicate a poor quality cell within the array. To classify the quality of a cell, only the first block of data for each cell is used and is assumed to be representative of the remaining blocks for the cell. The flowchart below (Figure 16) and the illustrative example below describe the developed procedure.

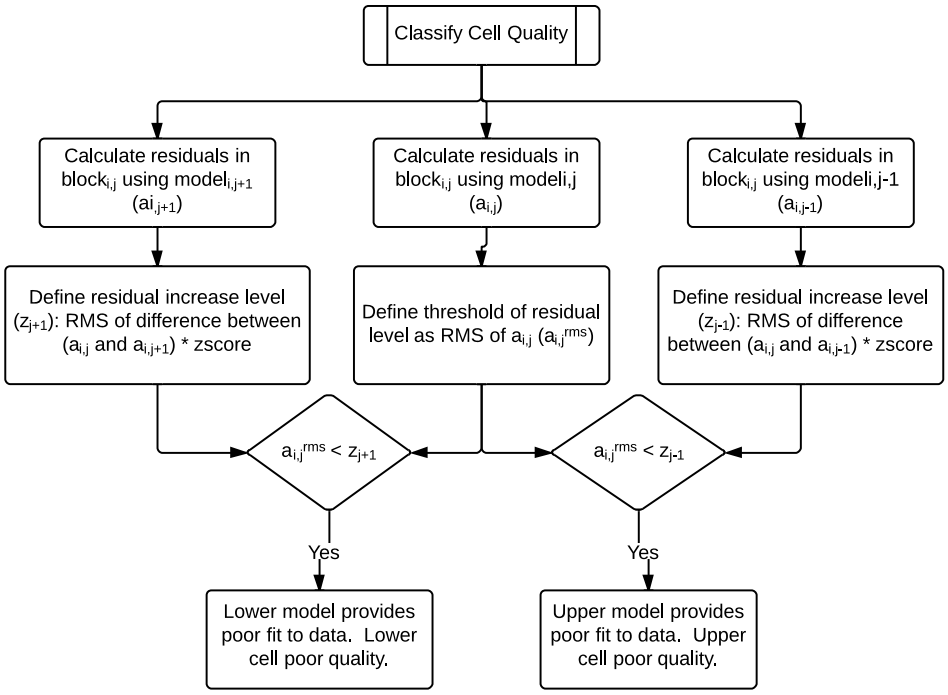

Figure 16: Cell quality classification sequence

For example, classifying the quality of data in the first block for the fifth cell ($block_{1,5}$) uses the model for that block ($model_{1,5}$), the upper block ($model_{1,4}$) and the lower block ($model_{1,6}$) and would proceed as follows:

1. Calculate model residuals ($a_{1,5}$) at each observation in block using $model_{1,5}$
2. Define the root-mean-square (RMS) intensity of the representative noise in the velocity signal as:

$$a_{1,5}^{rms} = rms(a_{1,5})$$

3. Where available, calculate residuals ($a_{1,4}$) by applying upper $model_{1,4}$
4. Where available, calculate residuals ($a_{1,6}$) by applying lower $model_{1,6}$
5. Calculate RMS of the difference between estimated residuals using $a_{1,4}$and $a_{1,6}$ compared to $a_{1,5}$:

$$\Delta a_{1,6}^{rms} = rms(a_{1,5} - a_{1,6})$$

$$\Delta a_{1,4}^{rms} = rms(a_{1.5} - a_{1,4})$$

6. Calculate the cutoff criteria that corresponds to a defined area of the residuals using z-scores:

$$z_6 = \Delta a_6^{rms} * C_z$$

$$z_4 = \Delta a_4^{rms} * C_z$$

7. A cell is considered to be poor quality when either of the following conditions is true:

$$a_{1,5}^{rms} < z_6 \text{ OR } a_{1,5}^{rms} < z_4$$

As a conservative measure it is recommended that if the cell immediately above the bottom cell is found to be poor quality then the bottom cell is flagged as poor quality. Similarly, if the cell immediately below the top cell is found to be poor quality then the top cell is automatically flagged as poor quality.

3.3.6 Additional data quality considerations

The primary mechanism by which $block_{i,j}$ is considered filtered is when a_{kurt} is reduced below C_k^{single}. However, in some data sets there may be a large amount of noise in the velocity signal that cannot be precisely modeled by the ARMA model and causes a persistently elevated a_{kurt} value. While it is theoretically possible to constantly replace the largest detected residual until the kurtosis of the residuals is reduced to below C_k^{single}, it is undesirable to excessively filter a data set by replacing representative noise in the signal. Therefore, provided that the a_{kurt} is below a given threshold, $C_{\Delta k,max}$, the relative change in kurtosis of the residuals between successive replacements may be used as a secondary cutoff threshold for data quality, as illustrated in the bottom of the flowchart in Figure 15 at the decision point '*Block adequately despiked?'*. When the change in kurtosis of the residuals between successive replacements is less than $C_{\Delta k}$, and a_{kurt} is less than $C_{\Delta k,max}$, the block is considered filtered, and replacement of the remaining minor spikes are forgone in favour of preserving the representative noise in the velocity time series.

The use of a single ARMA model for $block_{i,j}$ may cause poor quality spike detection and replacement if the model was estimated using poor quality data, such as when numerous large spikes are present. Therefore, a maximum percentage of observations within each block, C_{RM} are replaced using a given model before it is updated using the partially despiked data, as shown in Figure 15 with the decision point '*Replaced maximum number of observations in block (C_{RM})?*'. Since the models from adjacent cells are used in the detection and replacement algorithms, once C_{RM} is reached for $block_{i,j}$, the algorithm advances to $block_{i,j+1}$, but later returns to the partially despiked block using the updated model for the next iteration of despiking. This step ensures that high quality models are always used to detect and replace spikes.

3.3.7 Experimental apparatus

Velocity measurements were collected in a laboratory hydraulic flume using a VII velocity profiler. Data sets from 42 near-bed sampling locations with increasing flow depths, producing a range of turbulence scales, were used for initial testing of the procedure (Figure 17). Each time series was three minutes long with a sampling rate of 100 Hz and sampling cells sized of 2 mm.

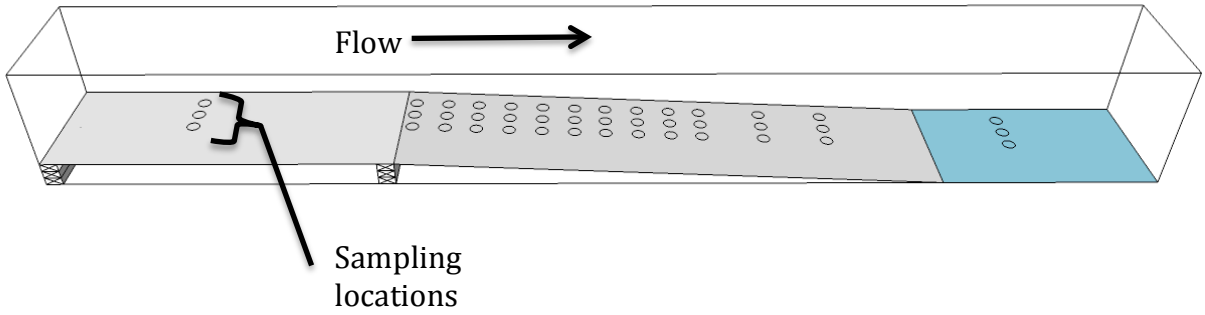

Figure 17: Sampling locations within flume

A representative streamwise velocity profile collected downstream of the change in flow depth is used as an illustrative example for the ARMA model fitting procedure and results.

3.4 Results

Tests were completed with the developed ARMA filtering method algorithms to determine the ability to detect and replace spikes and classify the data quality of individual sampling cells. The results are discussed below. A brief description of all coefficients used in the filtering program and recommended values are provided below in Table 1. All recommended values were empirically determined and have consistently performed well for a wide range of sampling conditions including turbulent flows. A brief analysis of the spatial distribution and relationships between the ϕ_1 and ϕ_2 coefficients for the proposed AR(2) models is also provided.

Table 1: Filtering algorithms coefficients and recommended values

Paramater	Description	Recommended Value
General		
C_{LB}	Length of block	2500
C_{mode}	Pre-screening data, maximum number of observations that share mode of each block	2.5%*C_{LB}
a_{kurt}	Kurtosis of model residuals calculated within a given block	N/A
C_{RM}	Coefficient, replacement maximum. Update models when dirty/overused	2%*C_{LB}
Detection		
C_k^{single}	Kurtosis - cutoff	4
$C_k^{max\_diff}$	Maximum kurtosis value for secondary cutoff condition using incremental difference in kurtosis ($C_{\Delta k}$).	6
$C_{\Delta k}$	Delta kurtosis cutoff	10% * C_k^{single}= 0.4
C_k^{group}	Potential grouped spike cutoff threshold	5*C_k^{single} = 20
C_a^{shock}	'shock-effect' coefficient	50%
C_a^{group}	Cutoff for grouped spike residuals	80%
C_{scan}	Number of observations to scan back/forward to	20
$C_{scan\%}$	"Look-around" condition for grouped spikes - other large residual in near vicinity	80%
Replacement		
$a_{MP\text{-}lead}$	Residual value at original leading edge of multipoint spike	N/A
$C_{MP\text{-}1}$	Coefficient, multipoint translate, low threshold: For smaller residuals where residual is between upper and lower bounds, the observation is replaced with the 'single point' replacement method	20%
$C_{MP\text{-}2}$	Coefficient, multipoint translate, high threshold: For observations at approximately the same level within the multipoint spike, translation of the observation to the main velocity signal is permitted	80%
Cell Quality		
C_z	z-score corresponding to percentage of area comparing areas of residuals	95% of area, or 1.96

The performance of filtering raw velocimetric data with both the GN phase-space threshold filter and the developed ARMA filtering program are provided. Although spike detection and replacement are coupled together in the ARMA program, results from each step are shown separately to illustrate their individual performance. To highlight the locations where a spike was detected with the GN method, the estimated linear interpolation replacement across the duration of the spike is shown. Replacement values estimated using ARMA models are shown for the corresponding spikes detected with the ARMA procedure.

3.4.1 Spike detection

An illustrative example of a simple, single point spike is provided in Figure 18. Both the GN and ARMA methods accurately detect the large negative spike located at 59.86 seconds. The GN method flags the interval from 59.84 to 59.88 seconds for replacement, whereas ARMA flags only the single point at the true spike. The 'spreading' of the error to include additional observations surrounding the spike causes additional, representative velocities to be unnecessarily replaced. Using the ARMA method, this spike is the third detected within the block of data and is associated with a kurtosis value of 98.8 prior to replacement. Therefore, the replacement algorithm initially assumes a grouped spike. However, no oppositely signed residuals are found in the vicinity of the spike, and the algorithm advances to the single point replacement technique.

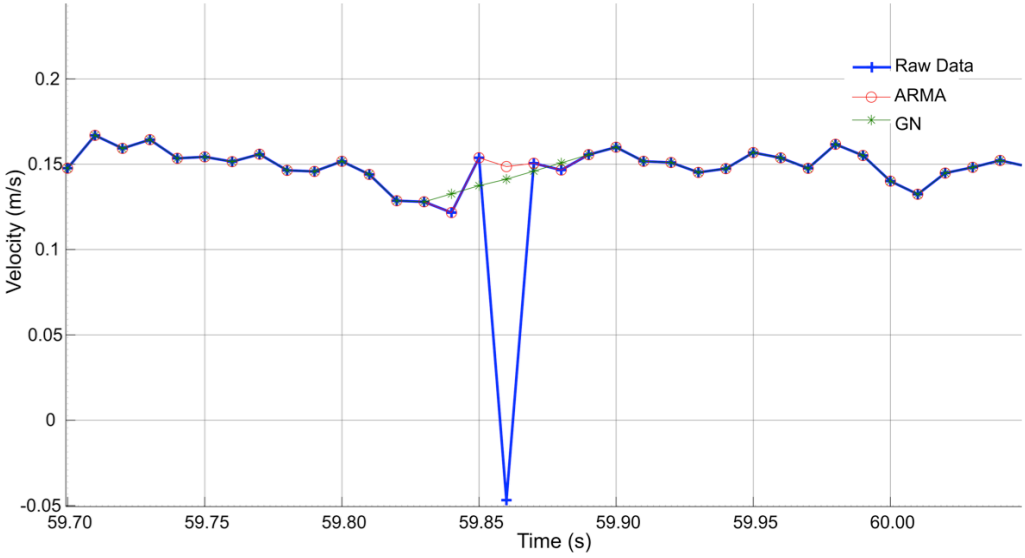

Figure 18: Single point spike detection

A simple, multipoint spike spanning two velocity values is provided in Figure 19. Both the GN and ARMA detection methods accurately detect the spike from 169.54 to 169.60 seconds. In the same manner as the single-point spike, the GN method flags good quality data on both sides of the spike for replacement, whereas the ARMA model only replaces the two poor quality velocities.

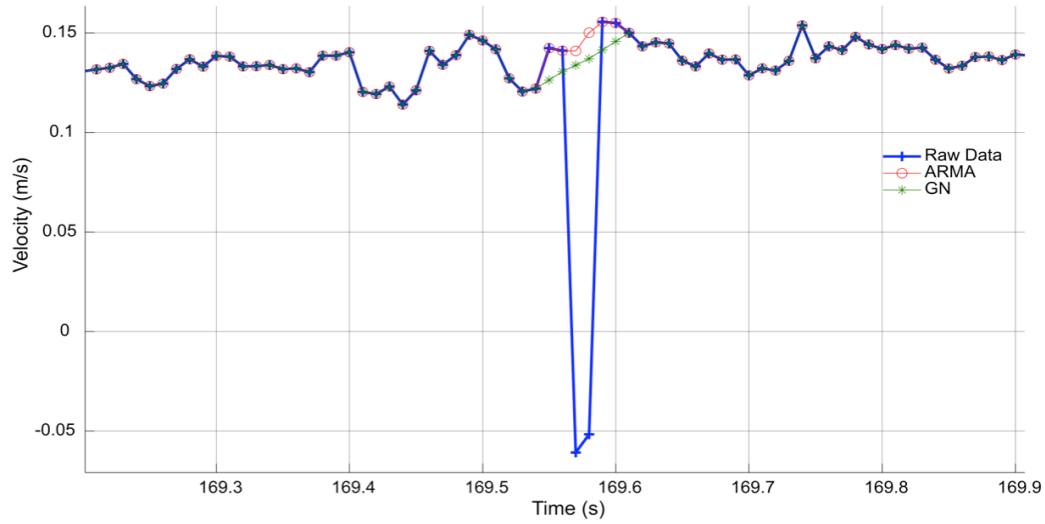

Figure 19: Multipoint spike detection

For the case of a multi-point spike preceded by a single point spike (Figure 20), both methods accurately detect the spikes. However, good quality data between the two spikes from 66.54 to 66.56 seconds is flagged for replacement by the GN filter. The kurtosis value of the residuals is equal to 124.7 and therefore flagged as a multi-point spike for replacement from 66.57 to 66.64 seconds, exclusive of the single point spike at 66.53. The replacement of the observations from 66.53 to 66.56 seconds is unnecessary as it is likely that these observations are representative of the true velocity conditions.

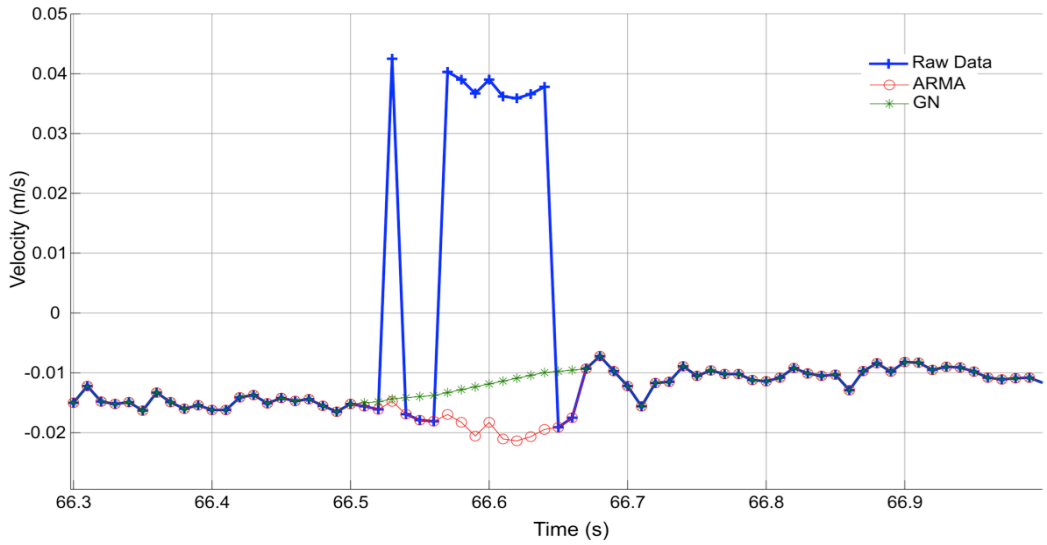

Figure 20: Complex, multipoint spike detection

The GN filter is noted to erroneously detect good quality data as spikes (Figure 21). This phenomenon appears to be associated with localized, rapid departures from the main velocity signal, such as when a coherent turbulent structure quickly passes through the sampling volume. The result of this localized departure is a cluster of observations being located outside the ellipsoid of good quality data and are falsely flagged as spikes. The ARMA method does not detect these observations as spikes and no replacement is conducted.

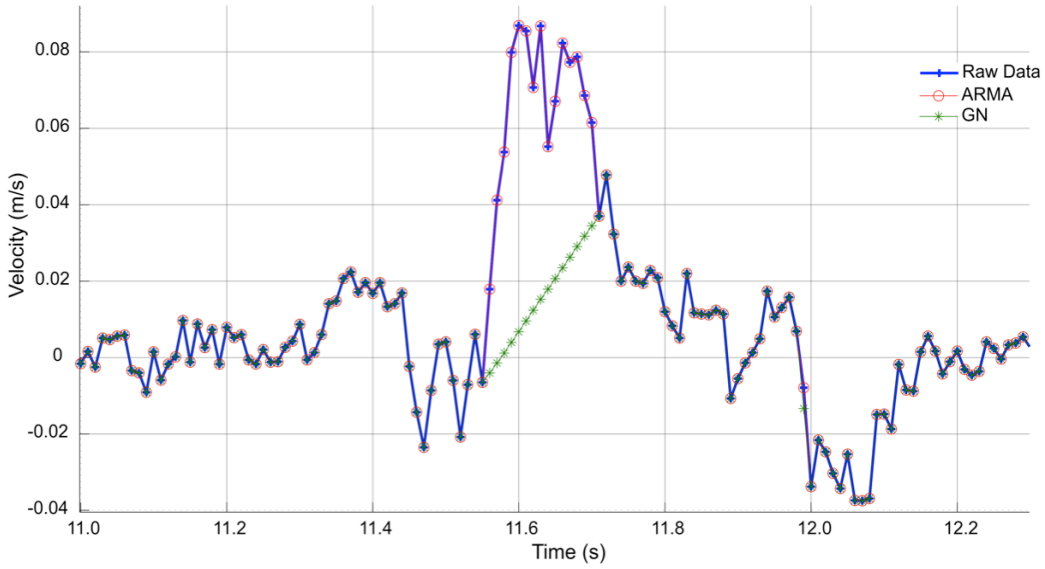

Figure 21: Elevated velocities spike detection

3.4.2 Spike replacement

The replacement of spikes is commonly seen to be of secondary importance to detection and is evidenced by less advanced replacement techniques (Razaz and Kawanisi, 2011). However, the chosen replacement method can have a significant effect on turbulence statistics and estimates of the mean velocity. An appropriate replacement method should generate replacement values that are visually congruent with local velocities and ensure that the turbulence statistics are preserved. Many replacement algorithms, such as linear interpolation, act to reduce the variance in the signal. This effect is magnified by the 'spreading' effect noted with the GN detection algorithm. The use of four different replacement alternatives is tested in this section: replacement using ARMA models, linear interpolation, replacement with the preceding

point and a third-order polynomial. With the exception of the ARMA procedure, all spikes are detected using the GN filter.

In the illustrative example below, only the ARMA method produces a replacement value that is indistinguishable from the surrounding velocity signal, while preserving representative random noise in the signal (Figure 22). For linear interpolation and replacement using the preceding good data point, a straight signal is produced across the replacement, eliminating the representative, localized noise in the signal. Replacement with a third-order polynomial produces a local maximum velocity and is followed by a monotonic decrease across the detected spike.

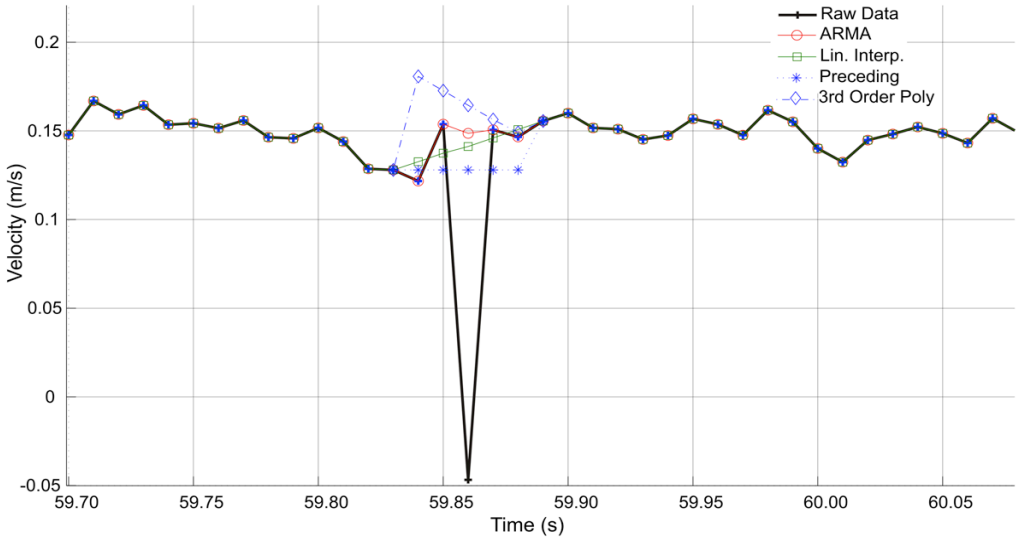

Figure 22: Single point spike replacement

Following replacement of the spike at 59.86, the kurtosis drops to 96.3, indicating that additional spikes are detected and replaced in the block.

Similar patterns among the replacement alternatives are noted with multipoint spikes. In the example below (Figure 23) the third-order polynomial successfully generates noise across the replaced values and can be argued to be in visual agreement with the local velocity signal. Replacement with the preceding data point produces a flat velocity signal and an abrupt increase in the velocities at the end of the spike as the velocity returns to the main velocity signal at 169.61 seconds.

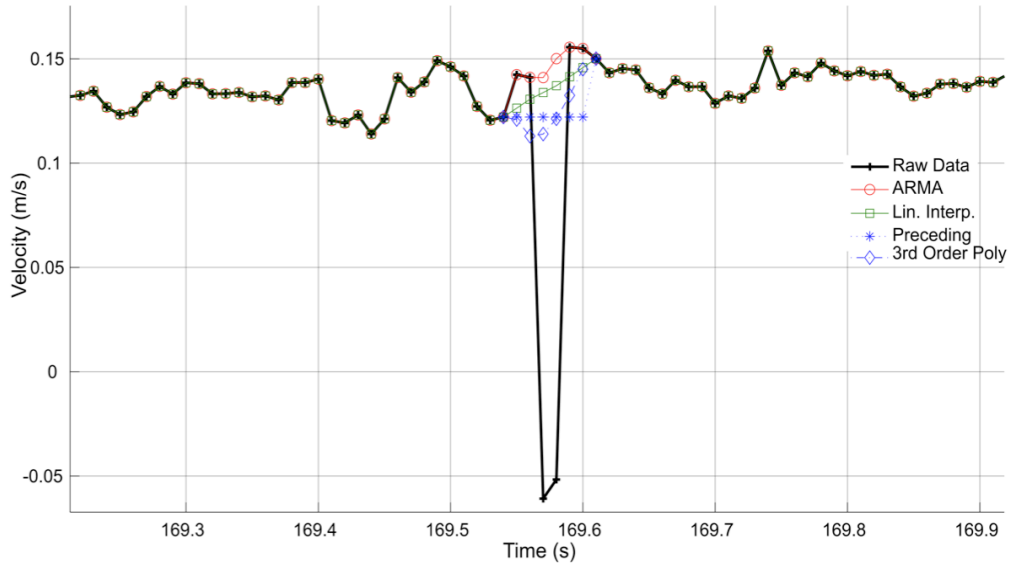

Figure 23: Multipoint spike replacement

The hypothesis that valuable information may be contained in recorded observations in a grouped spike was tested (Figure 24). In this example, the leading edge of the grouped spike is replaced on an observation-by-observation basis by translating the velocities to the main signal by a constant value, $a_{MP-lead}$. Although it is unknown if this translation restores the true velocity signal, the replaced values are in visual agreement with the local velocity signal and the noise within the velocity signal is at a comparable intensity to the noise surrounding the replaced spike, ensuring that turbulent statistics are preserved. Replacement with the third-order polynomial produces wildly invalid estimates across the detected spike and introduces new spikes into the data; any improvement to the overall velocity signal is highly questionable. Replacement with linear interpolation or the preceding point produces visually appealing estimates, but eliminates the local variance across the replaced spike.

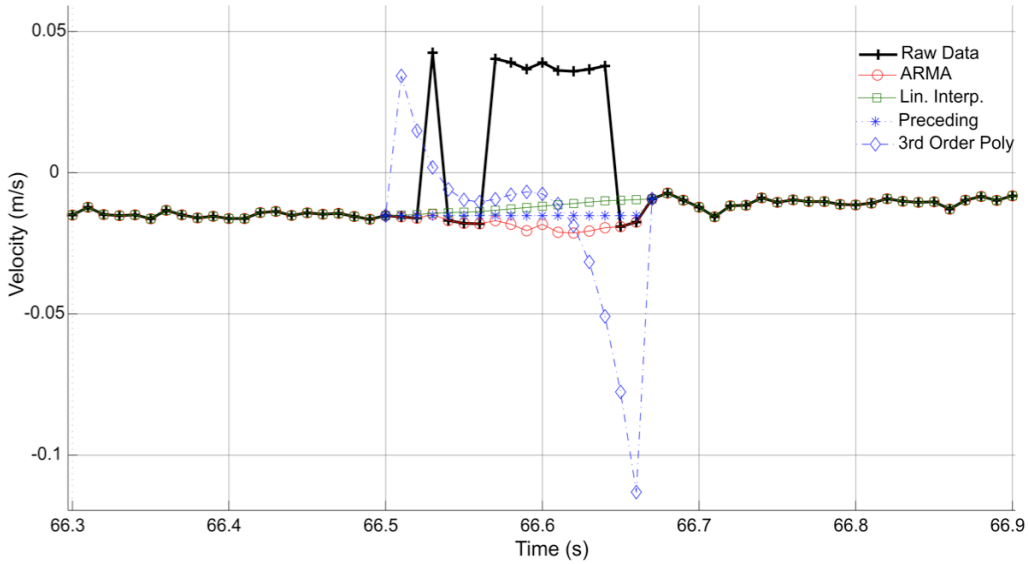

Figure 24: Complex, multipoint spike replacement

Due to the erroneous detection of spikes during a localized departure from the main velocity signal (Figure 25), replacement occurs across good quality observations, with each replacement option producing significantly different results. All three options result in a reduction in the variance within the velocity signal and produce results that are clearly not in visual agreement with the local velocity signal.

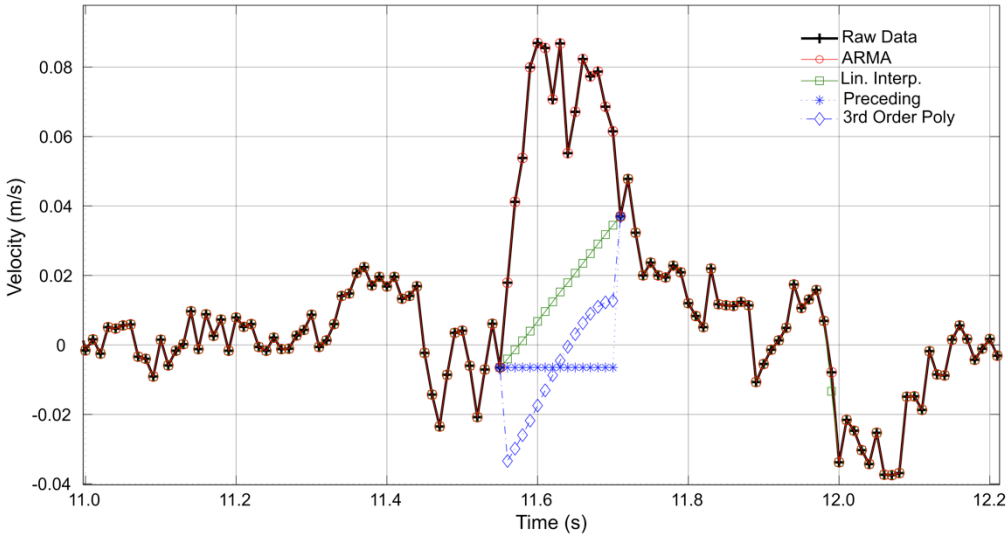

Figure 25: Elevated velocities spike replacement

3.4.3 Kurtosis as cutoff indicator

The use of the kurtosis of the model residuals (a_{kurt}) as a cutoff indicator for data quality is tested. It is hypothesized that as large magnitude residuals are flagged as spikes and subsequently replaced, a_{kurt} is reduced. Given that the residual values at each observation within a block are calculated using an ARMA model, it is expected that the distribution of the residuals will be approximately normal. Kurtosis of a normal distribution is equal to three. Therefore, for a 'cleaned' block of data containing no spikes, a_{kurt} is expected to be slightly larger than three to account for natural noise within the velocity signal. In this section it is tested if a single, universal threshold, C_k^{single}, can be defined for use in filtering velocimetric data. A representative sampling cell from the centerline location upstream of the change in bed slope at the 'sweet spot' of the VII consisting of eight consecutive blocks of data was selected to illustrate the relationship between a_{kurt} and the number of spikes replaced. Within each block, the value of a_{kurt} was recorded following each replacement event until a lower plateau of a_{kurt} was observed (Figure 26).

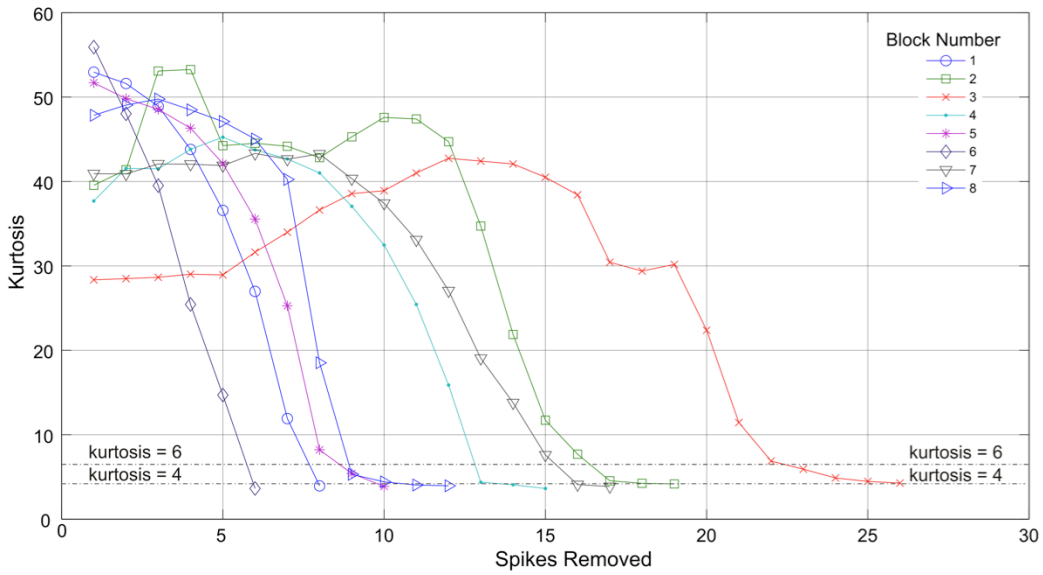

Figure 26: Kurtosis of model residuals during replacement events

Two critical observations are made regarding defining a cutoff threshold. Firstly, when a_{kurt} was reduced to below four, the detected spikes were low magnitude and highly subjective and any benefit gained from replacement was questionable. Secondly, defining C_k^{single} as a universal, minimum cutoff indicator appears valid, and is approximately equal to four as indicated by the plateau reached near this

value. This generally corresponds to the condition when large, highly distinguishable spikes had been replaced and successive replacements provided minimal, but still worthy, improvement in the overall data quality of the block (see Figure 27 and Figure 28 for examples). This observation provided the motivation for establishing the $C_{\Delta k}$ parameter whereby small, incremental reductions in the kurtosis of the residuals can act as a secondary cutoff indicator, provided that a_{kurt} is below an upper threshold, $C_k^{\max\_diff}$, which has been empirically estimated to be approximately equal to six.

The relationship between raw velocity, model residuals, and a cleaned block of data is provided for two representative examples. The examples correspond to $block_{5,1}$ and $block_{5,3}$ in Figure 26. Using $block_{5,1}$ from the same velocity data set described above, a total of eight spikes are replaced before a_{kurt} is reduced to below C_k^{single}. Initially, a_{kurt} is approximately 53.0 and therefore the spike is tested for possible inclusion within a multipoint spike. However, no large oppositely signed residuals are found, and therefore the first spike is replaced as a single point spike. This procedure is completed for the remaining six spikes in $block_{5,1}$ until a_{kurt} is reduced to 3.94. In Figure 27 below the raw velocity time series, initial residuals and the cleaned time series for $block_{5,1}$ is provided. The numbers inside red boxes indicate the sequence that the spikes were detected.

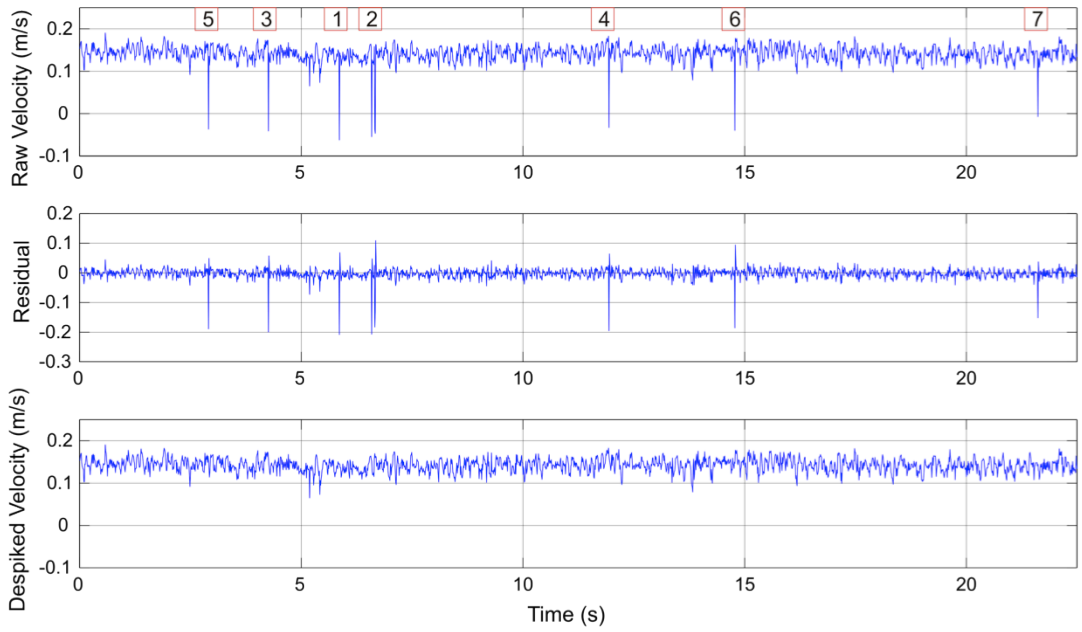

Figure 27: Multiple replacements in $block_{5,1}$. Raw data (top), model residuals (middle) and cleaned signal (bottom)

For $block_{5,3}$, the ARMA algorithm estimates that 26 spikes are present (see Figure 26 and Figure 28) comprised of 20 single-point spikes and 4 multi-point spikes. In this block the effect of incremental improvements during later spike replacements is apparent after spike 21 when a_{kurt} incrementally decreases from 6.27, 5.31, 4.83, 4.49 and 4.15 and ultimately 3.80 thereby indicating the block is cleaned. It is interesting to note that a_{kurt} temporarily increases after approximately the fifth replacement due to replacement of several large magnitude negative spikes that cause elimination of associated positive residuals and produces an asymmetrical distribution. However, once multiple negative residuals are removed, the kurtosis rapidly decreases as the symmetry is restored. Additionally, it can be seen that the cleaned time series preserves a representative level of noise in the velocity signal. For example, replacement of the final spike (spike 26 at t = 46.5 seconds) is a relatively small magnitude spike, but is perceived to be worthy of replacement. Following replacement of this spike, a_{kurt} is reduced to below C_k^{single} and $block_{5,3}$ is considered cleaned.

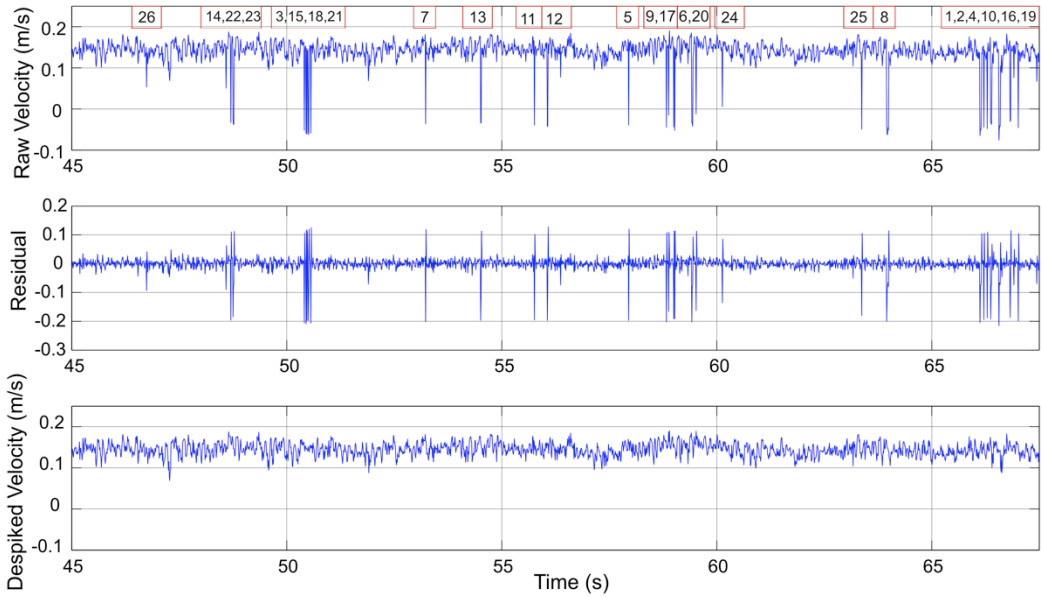

Figure 28: Multiple replacements in block$_{1,3}$. Raw data (top), model residuals (middle) and cleaned signal (bottom).

3.4.4 Model coefficients

An analysis of the relationships between the AR(2) model coefficients is explored in this section. Relationships between ϕ_1 and ϕ_2 coefficients for each block of data are examined to determine if valuable information about the structure of modeling a turbulent velocity signal and data quality can be obtained. An analysis of this nature was completed by Robert et al (1993) noting a pseudo-oscillatory pattern and a strong correlation between model coefficients such that $\phi_1^2 < -4\phi_2$, without consideration of the spatial sampling location. A comparison of the relationship between the estimated coefficients for a total of 104 blocks of data when the 'sweet-spot' of the VII was located at approximately 3 and 11 cm above the bed, respectively (Figure 29). An increase in the flow depth occurs at approximately 1.05 m downstream from the reference datum and extends to 3.05 m. Closed red circles indicate sampling blocks located within the 'sweet spot' of the instrument and open blue circles represent coefficients for all other cells.

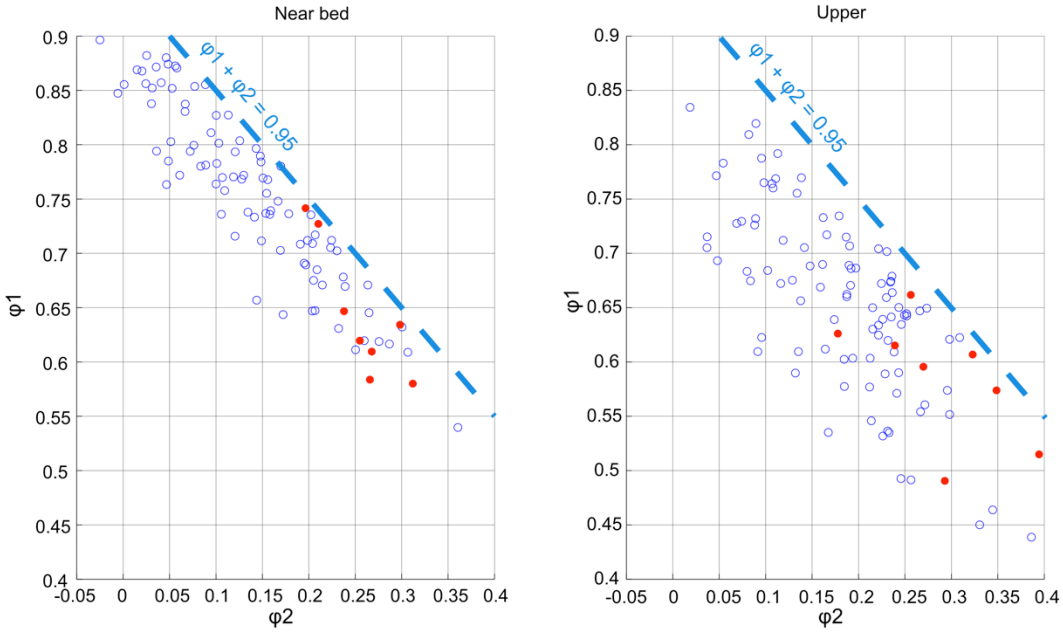

Figure 29: Relationship between ϕ1 and ϕ2 coefficients. At bed (left) and above bed (right)

As seen in the above figure, there is an upper boundary at approximately $\phi_1 + \phi_2 \approx 0.95$, and a weakly defined lower boundary, depending on the probe height. This observation is similar to Robert et al

(1993), indicating that upper boundary is present in the data, albeit with a significantly different relationship. There is no clear pattern for the relationship between 'sweet spot' blocks and other blocks.

The 'tightness' of the relationship between ϕ_1 and ϕ_2 is estimated using the R^2 value for a line fit of best fit of the data. For all blocks at a given sampling location, the relationship between ϕ_1 and ϕ_2 was plotted and the R^2 value was calculated (Figure 30). The spatial distribution of the median ϕ_1 and ϕ_2 values for blocks within the 'sweet spot' are provided. Squares to the left of the dotted line (axis 'a') represent near bed sampling locations measured at increasing lateral distances from the sidewall up to the centerline of the flume at x = 0.1, 0.2 and 0.3 m. Squares to the right of the dotted line (axis 'b') represent sampling locations at increasing vertical distances above the bed with the 'sweet spot' at 0.05, 0.1 and 0.15 m above the bed.

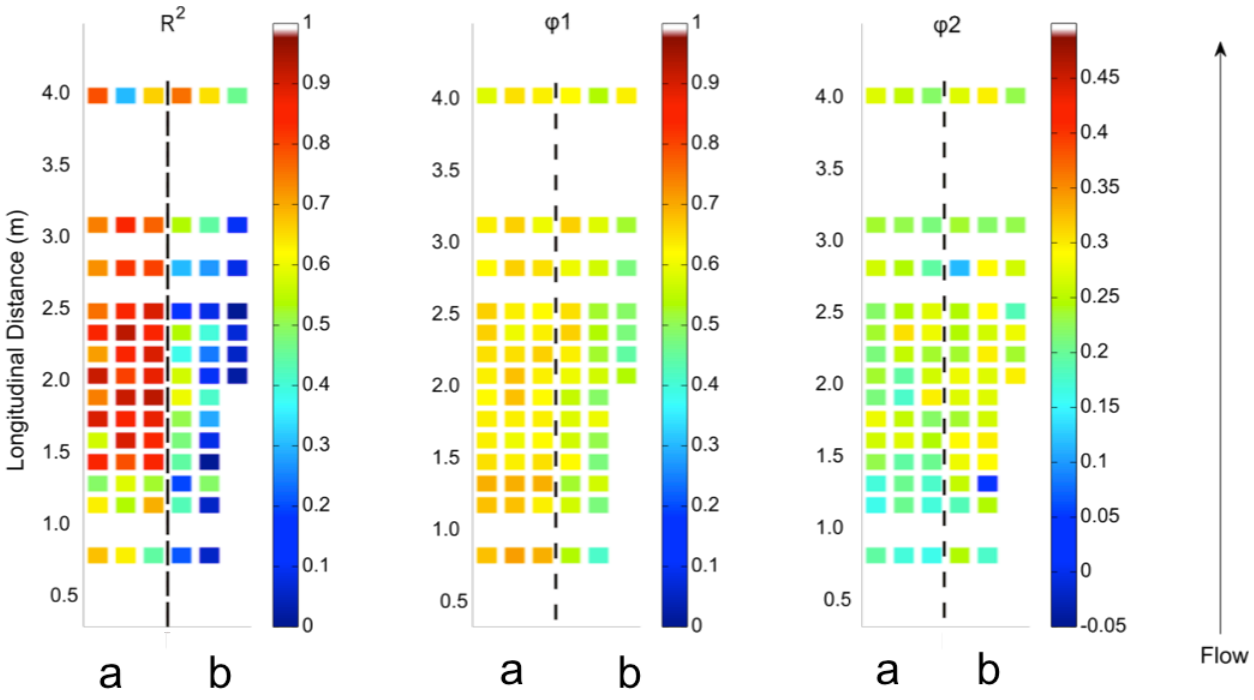

Figure 30: Spatial Distribution of R^2, ϕ1 and ϕ2. Horizontal axis 'a' represents lateral sampling location and horizontal axis 'b' represents vertical sampling locations along centerline.

As expected, ϕ_1 coefficients are much larger than the ϕ_2 coefficients, indicating velocities at y_t are more strongly correlated with observations at y_{t-1} than at y_{t-2}. Although no patterns are apparent in the ϕ_1 coefficients at near bed locations, the coefficient gradually decreases at greater heights above the bed.

The significance of this, if any, is unknown. The R^2 values are highest at near bed locations. Furthermore, the highest R^2 values occur downstream of the increase in flow depth, where coherent turbulent structures are known to be strongest. Therefore, it is suspected that due to coherent structures, the similarity between temporally and spatially adjacent blocks produces less variability in the relationship between the ϕ_1 and ϕ_2 coefficients and thus greater R^2 values.

The spatial and temporal distribution of the ϕ_1 and ϕ_2 coefficients at a single sampling location was examined. Using a block length of 600 observations, the ϕ_1 and ϕ_2 coefficients were determined for each block of data for all sampling cells within the profile. Velocity data from the near-bed, centerline sampling location approximately 0.20 m downstream of the transition to the deceleration of flow was used (Figure 31). Cell 1 is at the top of the sampling profile whereas cell 13 is at the bottom of the profile.

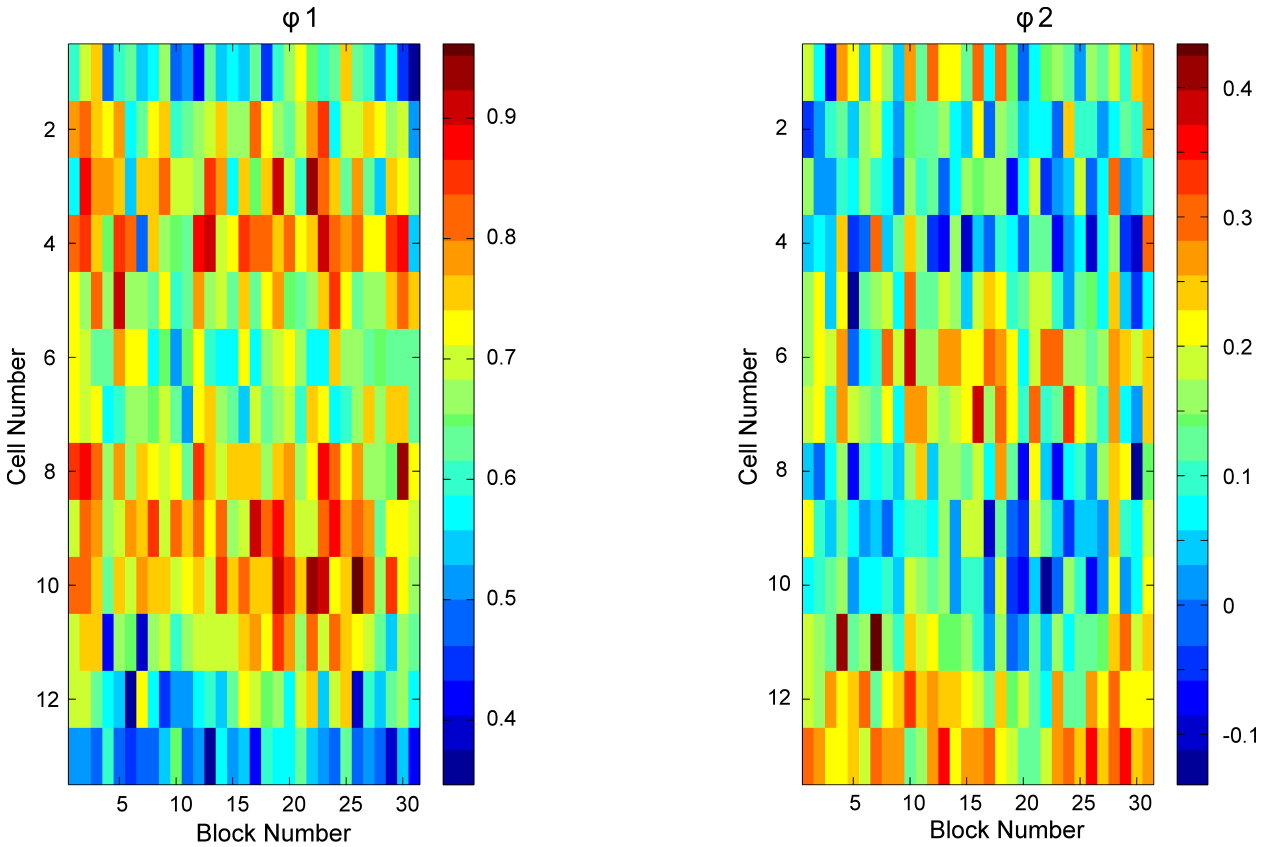

Figure 31: Spatial and temporal distribution of ϕ1 (left) and ϕ2 (right) coefficients at a single sampling location

This figure indicates that a spatiotemporal correlation exists within each coefficient and between the two coefficients. For example, a group of elevated ϕ_1 coefficients is centered around block 22, cell 10 with values generally above 0.8. A similar grouping of low ϕ_2 coefficients occurs at the same location and time. It is also of interest to note that the ϕ_1 coefficients in cell 13 are significantly lower than in cell 12 immediately above and this trend persists for all 31 blocks of data.

Chapter 4
IMPULSE AND SEDIMENT MOVEMENT

This chapter describes the developed methods and results of laboratory-scale experiments investigating the role of impulse in sediment mobility. The goals of this method are to develop an understanding of the spatial distribution of turbulent structures and determine the role of bed slope, particle size and specific gravity in sediment mobility and impulse events.

Seven bed slope/flow rate configurations were used in a laboratory hydraulic flume. Six of the experiments were completed at low flow conditions with local bed slopes ranging from -2.7^{o} to $+2.7^{o}$ relative to the overall bed slope. No direct measurements of sediment movement were made during these experiments. The collected data is analyzed to determine the spatial distribution of impulse events along a sampling reach under varying bed slopes and a theoretical analysis is completed to study the effect of particle size and specific gravity in sediment mobility. A seventh experiment was completed for a detailed study on the concept of impulse and sediment mobility using a single bed slope at a high flow and a single particle of interest. The high flow condition was selected to produce a wide range of sediment transport potentials within the sampling reach, with the test particle moving instantaneously in some areas of the experimental section of the flume and not at all in other sections. A minimum of 42 near-bed, high-resolution, three-dimensional sampling events were completed for each bed slope/flow rate configuration.

4.1 Flume experiments

A flume at the University of Waterloo's Fluid Mechanics laboratory measuring 15.5 m long, 0.6 m wide and 0.5 m deep was used for all flume experiments (Figure 32). The flow rate was controlled using a gate valve on the main inlet pipe supplying the headwater tank.

Figure 32: Laboratory flume used for experiments

Six different bed slope configurations were constructed in the flume to produce zones of convective acceleration of flow (CAF) and convective deceleration of flow (CDF), such as the CDF configuration shown in Figure 33. Three CAF zones with local bed slopes of -0.9^o, -1.8^o, -2.7^o relative to the overall bed slope (denoted by CAF1, CAF2 and CAF3, respectively) and three CDF zones with downward bed slopes of +0.9^o, +1.8^o and +2.7^o (denoted CDF1, CDF2 and CDF3, respectively) were constructed in the flume. The required bed slopes were created by placing wooden blocks under the PVC sheets. Small diameter plastic tubing was wedged in the gap between the edge of the sheet and the flume sidewall to minimize the potential for water to flow underneath the PVC sheets. A sampling grid was created in the flume to provide systematic measurement locations for velocity sampling events. A reference datum was established 1 m upstream of the entrance to the bed slope change and all streamwise locations were measured relative to this datum. Lateral grid points were at 0.1, 0.2 and 0.3 m (centerline) from the flume sidewall (Figure 33).

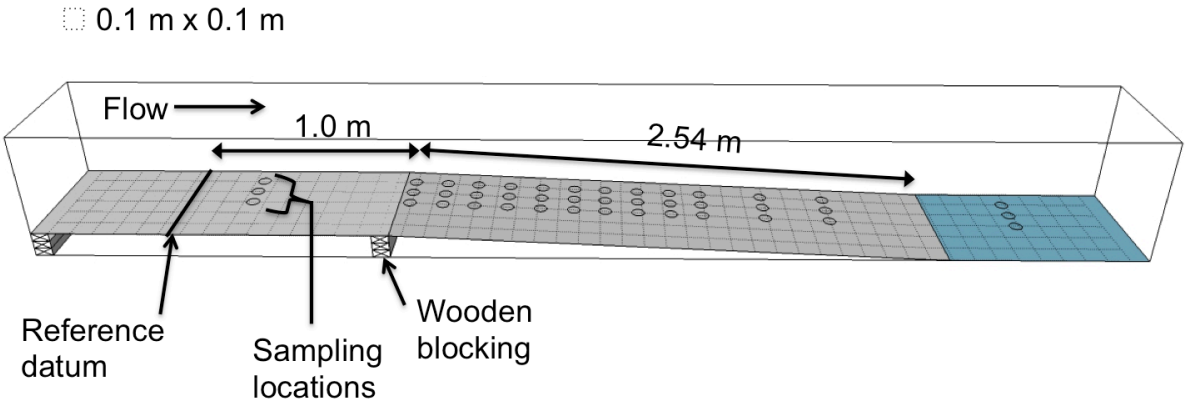

Figure 33: CDF flume configuration and sampling locations

For the seventh flume experiment requiring a sediment particle, a one-inch (25.4 mm) diameter Teflon™ sphere with a specific gravity of 2.3 (Celik et al, 2010), similar to that of natural sediments, was used (Figure 34). The particle was fully exposed to the flows to isolate the role of velocities causing sediment movement and to avoid the potential influence of particle shielding, particle imbrication, particle orientation and particle shape. Two PVC sheets (2.4 m by 0.6 m) with a layer of 2 mm sand grains adhered to the surface were used to provide a rough bed surface in the flume when required. Loose sand was placed at the transition between the PVC sheets and the permanent flume bottom and at the gap between the two sheets to create a natural transition (Figure 34).

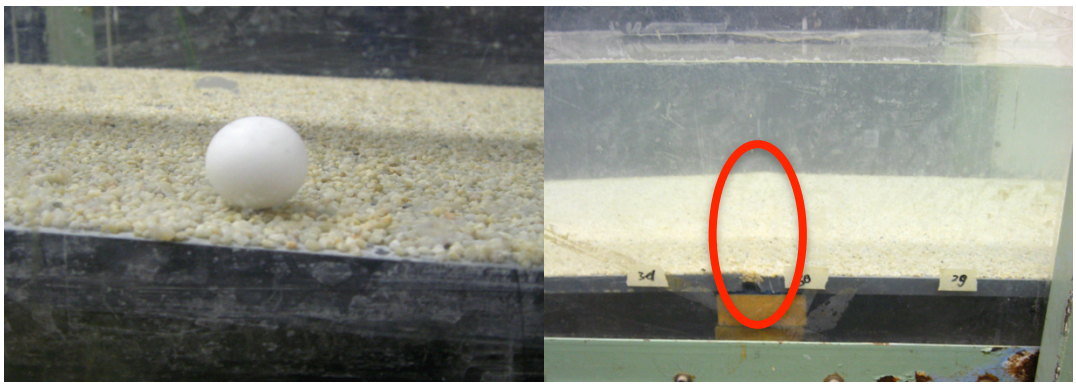

Figure 34: Spherical particle and sand grains on PVC sheets (left) and loose sand covering transition between sheets (right)

A summary of hydraulic parameters for the seven sets of experiments are provided in Table 2. For the six CAF and CDF experiments, the 'sweet spot' of the VII was positioned at approximately 10% of the flow depth for the first sampling event at each grid location. All sampling events were three minutes in duration with a sampling frequency of 100 Hz and a cell size of 2 mm. For the first six experiments a constant flow depth of approximately 0.30 m was maintained within the pool. For the seventh experiment, CDF2-H, (CDF2 bed configuration under high flow conditions), the flow rate was increased to study the role of turbulence in sediment movement. To calculate the flow rate, Q, the 'sweet spot' sampling cell at the centerline sampling location closest to 60% of the flow depth at was used. It is assumed that the velocity as 60% of the flow depth can be used to estimate the mean velocity at each lateral location within the channel. All other calculations requiring a velocity use the 'sweet spot' cell for the near-bed sampling event. $F_{r,entry}$ and $R_{e,entry}$ are the Froude number and Reynolds number estimated upstream of the ramped section, respectively. $F_{r,exut}$ and $R_{e,exit}$ are measured downstream of the ramped section. The shear velocity upstream and downstream of the ramp are given by u^*_{entry} *and* u^*_{exit}, respectively. The ratio of the channel width, W, to the water depth, Z, are given at the entry and exit locations, indicated by W/Z_{entry} and W/Z_{exit} respectively.

Table 2: Hydraulic conditions

Zone	*Q (m^3/s)*	*u^*_{entry} (m/s)*	*u^*_{exit} (m/s)*	*$R_{e,entry}$*	*$R_{e,exit}$*	*$F_{r,entry}$*	*$F_{r,exit}$*	*W/Z_{entry}*	*W/Z_{exit}*
CAF1	0.017	0.0051	0.0062	1.4E+04	1.6E+04	0.05	0.08	2.0	2.5
CAF2	0.016	0.0052	0.0066	1.5E+04	1.5E+04	0.06	0.09	2.0	3.0
CAF3	0.009	0.0026	0.0055	7.3E+03	9.5E+03	0.03	0.08	2.0	3.9
CDF1	0.019	0.0064	0.0040	1.6E+04	1.6E+04	0.08	0.06	2.4	1.9
CDF2	0.018	0.0071	0.0042	1.7E+04	1.5E+04	0.10	0.06	3.0	2.0
CDF3	0.017	0.0095	0.0039	1.7E+04	1.6E+04	0.14	0.06	3.9	2.0
CDF2-H	0.040	0.0344	0.1480	4.29E+04	4.14E+04	0.440	0.207	0.450	0.239

Velocity time series from the CDF2-H configuration consisting of 42 near bed velocity time series were analyzed to determine the spatial distribution of the mean velocity (U), shear velocity (u^*), dimensionless shear or Shields parameter (τ^*), normalized Reynolds stress ($\tau_R^+ = -\overline{u'w'}/(u_o^*)^2$) and the maximum impulse (I_{max}) at each sampling location. The parameters U, u^*, τ^* and τ_R^+ are common parameters used in estimating the potential for sediment transport, whereas impulse represents a new method that accounts for turbulent fluctuations in the fluid. The Clauser fitting procedure is used to calculate u^* with mean velocities from the six sampling cells surrounding the 'sweet spot' of the VII including the two cells

immediately above, and three cells below the 'sweet spot'. A κ value of 0.4, k_s value of 2 mm and B_r equal to 0.0 were used. The selection of a B_r value of 0.0 was selected to produce maximum u^* in regions where movement is known to occur.

The concept of impulse was tested for its potential to better understand the spatial distribution of turbulent structures under non-uniform flow conditions and the mobility of sediment particles. Although a direct link between turbulent forces and the movement of individual particles cannot be established with the proposed experiment procedure, a correlative technique will be used to better understand this relationship. This procedure consists of estimating the impulse events within a time series and classifying the movement of sediment particles. All impulse events were calculated using the streamwise velocity data from the VII's 'sweet spot' sampling cell in the near-bed environment. A two-step process was used to calculate the magnitude of individual impulse events in a time series. Firstly, the critical velocity, u_{cr}^2, was calculated using the physical properties of the particle and its arrangement on the bed, as per Equation 16. Secondly, the u^2 values of the velocity time series were calculated and compared to u_{cr}^2. The magnitude of the impulse event was then calculated as the product of u^2 and the event duration. The simplification of using a time averaged u^2 value, as shown in Equation 13, was not used because the measured velocities correspond to the instantaneous forces imparted on the particle, rather than a time-averaged estimate. Rather, the original integral definition was used for the duration of the impulse event:

$$Impulse = \int_{t_1}^{t_2} u_i^2 T_i \tag{28}$$

An impulse event begins when u^2 exceeds u_{cr}^2 (at time t_1) and persists until u^2 is reduced to below u_{cr}^2 (at time t_2). All impulse events were calculated for a hypothetical 25.4 mm sphere with a specific gravity of 2.3, Z_{arm} equal to the radius of the sphere (12.7 mm) and X_{arm} of 0.45 mm and a drag coefficient of 0.76 (Schmeeckle, 2007). A constant definition of the horizontal lever arm length, X_{arm}, was not made due to difficulties in accurately measuring this value for the rough bed conditions used. Table 3 summarizes the critical conditions necessary for a single impulse event to be initiated at a given sampling location when X_{arm} is assumed to be equal to the radius of the bed sand grains (1 mm).

Table 3: Critical force and velocities for 25.4 mm Teflon sphere

Zone	*β*	F_{Dcr} *(N)*	u^2_{cr} *(m^2/s^2)*
CAF1	-0.9	0.0143	0.0627
CAF2	-1.8	0.0166	0.0729
CAF3	-2.7	0.0190	0.0833
CDF1	0.9	0.0096	0.0420
CDF2	1.8	0.0072	0.0317
CDF3	2.7	0.0048	0.0212
CDF2-H	1.8	0.0072	0.0317

For example, under CAF1 configurations, when a single u^2 value in the velocity time series exceeds 0.0627 m^2/s^2, an impulse event is initiated. When u^2 reduces below this value, the individual impulse event has ended. The minimum required u^2_{cr} and $F_{D,cr}$ exerted on a particle is greatest for the CAF3 bed configuration, and smallest for CDF3, indicating that the minimum force required to move a particle under an adverse slope is greater than under positive slope conditions as expected.

The movement of the Teflon sphere was classified based on its observed behaviour at different locations. Observed behaviours ranged from immediate, strong movement to delayed movement with particle rocking to no movement. The sphere was placed on the bed at each grid point location and its behaviour was visually observed and described during a three minute observation period. If the precise positioning at a grid point (i.e. within a few millimeters) was a significant factor in movement, this behaviour was noted and minor relocation of the particle was permitted and an additional observation period was completed. A ranking classification was developed to quantitatively describe the movement behaviour of the sphere (Table 4).

Table 4: Particle movement behaviour

Rank	Dislodgement	Rocking	Location Sensitivity
1	Never	None	No
2	Never	Light	No
3	Never	Moderate	Minimal
4	Eventual, variable	Heavy	Moderate
5	> 120 seconds, variable	Heavy	Moderate
6	> 60 seconds, variable	Heavy	Highly
7	10 - 60 seconds	Heavy	Minimal
8	Few seconds	No	No
9	Nearly instantaneous	No	No
10	Instantaneous	No	No

Once the behaviour of the particle was classified, the particle was removed from the flume to allow for undisturbed velocity measurements with the VII. Due to the temporal separation between particle movement observation and velocity measurement, a direct link between specific turbulent velocities and particle movement could not be established using this method.

4.2 Results

4.2.1 High flow rate conditions

All results for hydraulic variables are presented for the 'sweet spot' cell located at approximately 10% of the flow depth above the bed. Three lateral sampling locations at each downstream interval were used: 0.1, 0.2 and 0.3 m from the sidewall of the flume (Figure 35). The transition to the CDF zone begins 1.05 m downstream of the reference datum.

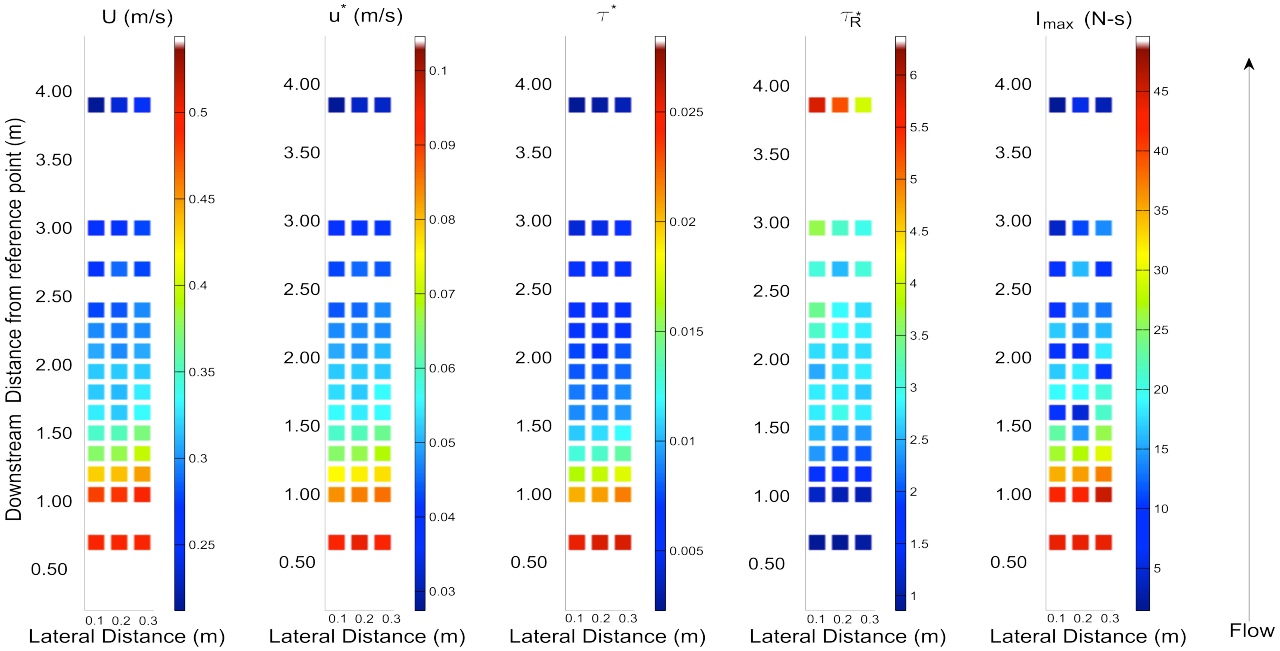

Figure 35: Spatial distributions for CDF2-H sampling configuration a) mean velocity b) shear velocity c) dimensionless shear stress (Shields parameter) d) normalized Reynolds stress and e) maximum impulse

Parameters U, u^* and τ^* exhibit similar spatial patterns within the sampling reach. All three parameters reach local maximums upstream of entry to the CDF zone at x = 0.7 m downstream of the datum,

reaching 0.490 m/s, 0.0345 m/s and 0.025 respectively, and at the first sampling location within the CDF zone at x = 1.05 m (0.483 m/s, 0.0335 m/s and 0.021 respectively). These three parameters consistently decrease through the CDF zone, reaching a minimum at the downstream end and within the uniform section. As previously discussed, the shear stress, τ, is directly proportional to the shear velocity, u^* and therefore is expected to linearly decrease as the flow expands. When considering the dimensionless shear stress, τ^*, the highest potential for movement occurs in the vicinity of the entry to the CDF zone. A τ^* value greater than 0.05 is generally cited as the threshold for movement (e.g., Wong and Parker, 2006) suggesting that movement is not expected at any location. However, the calculated values are only slightly less than threshold conditions at the upstream entry and exhibit the expected linear decline through the CDF zone.

The production of large coherent turbulent structures within the CDF zone are not accounted for in the calculation of τ^* and therefore a complete understanding of the conditions that cause sediment movement cannot be made using τ^* alone. The normalized Reynolds stress, τ_R^+, provides a measure of the bulk turbulence intensity in the fluid. A strong negative correlation is shown between τ_R^+ and u^*, illustrating a decoupling between these two parameters in the CDF zone. τ_R^+ gradually increases through the CDF zone, from approximately 1.1 to 3.6 over the length of the CDF. At the sampling locations in the uniform section (downstream of x = 3.9 m), τ_R^+ reaches a local maximum of 5.8. This demonstrates that these two parameters are not equally valid for estimating sediment movement potential when turbulent conditions are present. The distribution of I_{max} is slightly more variable than other parameters, but high magnitude events are generally noted downstream of the entry to the CDF zone reaching approximately 45.1 N-s at x = 1.05 m and quickly reduce to approximately 25.8 N-s at x = 1.50 m. It is weakly shown that except in the transition zone immediately downstream of the entry to the CDF zone, I_{max} values are slightly lower along the centerline of the flume, compared to sampling locations closer to the flume walls.

An illustrative example is provided for identifying impulse events within a velocity time series using data from the centerline sampling location in the uniform flow section downstream of the CDF zone at x = 3.90 m (Figure 36). A hypothetical 25.4 mm sphere with a specific gravity of 2.3, C_D equal to 0.76 and a X_{arm} length of 1 mm is used, producing a u_{cr}^2 value of 0.0375 m^2/s^2 as indicated by the dotted red line in the figure.

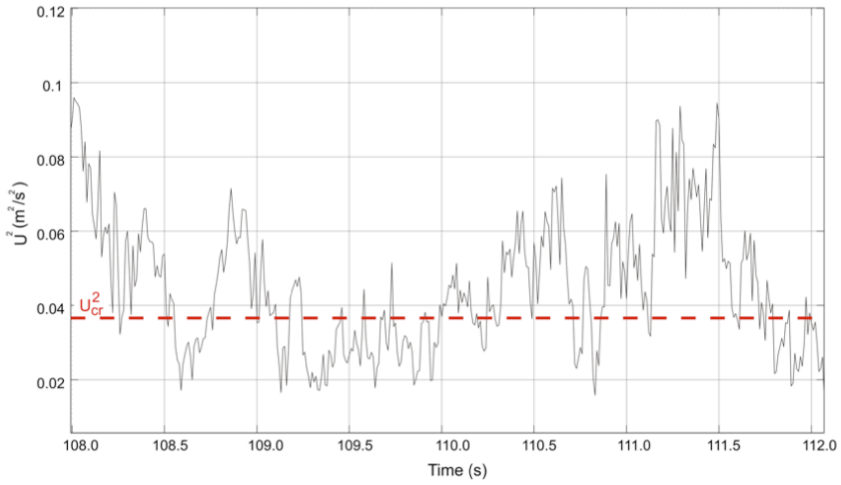

Figure 36: Identification of impulse events within u^2 time series

Many small magnitude events are noted within the u^2 time series, such as at t = 109.75 seconds, where u_{cr}^2 is exceeded for only one observation (1/100th second) and the magnitude of the exceedance is relatively small. A more significant impulse event with a larger magnitude and longer duration is noted for example at t = 111.2 to 111.6 seconds. It must be reiterated that this example is from the downstream location within the uniform flow section where impulse events are relatively small. For the majority of sampling locations with the CDF zone, u_{cr}^2 is exceeded for long durations (up to, and including the entire 180 second sampling duration) and therefore do not provide an illustration of multiple impulse events with varying magnitudes. Regardless of the number of individual impulse events, the calculation of impulse events remains identical.

The production of large impulse events requires high magnitude velocities that persist for long durations. Under the bed slope and flow rate configuration used for CDF2-H, a total of 115 impulse events are estimated at all locations in the flume using the 42 near-bed 'sweet spot' velocity time series. A range of velocities and durations are noted at the various sampling locations (Figure 37 – left). To illustrate the u^2 values, the mean squared velocity ($<u^2>$) for the duration of each impulse event is shown. The distribution of velocities and durations for the low flow CDF2 configuration, consisting of a total of 4409 impulse events, is provided as an illustrative comparison (Figure 37 – right).

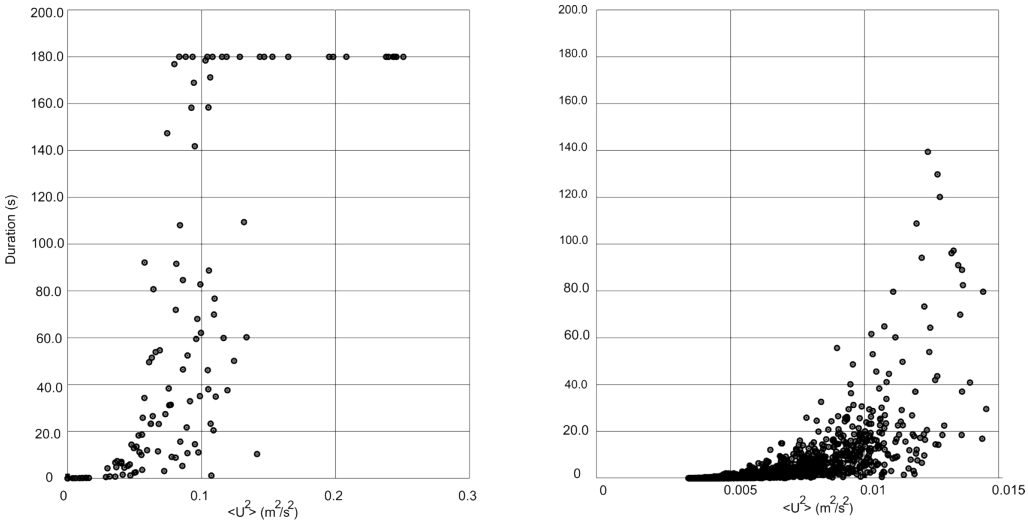

Figure 37: Duration and intensity of impulse events for CDF2-H (left) and CDF2 (right)

For the CDF2-H configuration it is noted that at 23 sampling locations, the impulse event persists for the entire 180 second sampling duration. These sampling locations are near the entry to the CDF zone, where the recorded velocities are consistently greater than u_{cr}^2. Sampling locations further downstream are associated with a wide range of impulse event durations, from a fraction of a second up to the entire sampling duration. Under low flow conditions, CDF2, no single impulse event persists for the entire 180 second sampling duration, and the maximum impulse events are approximately one order of magnitude less than for the CDF2-H flow rate.

To determine the spatial distribution of the movement potential at each sampling location in the flume for the CDF2-H, results of the movement rankings were examined. Using the ranking system developed in Table 4, the movement behaviour at each sampling location is summarized in Figure 38.

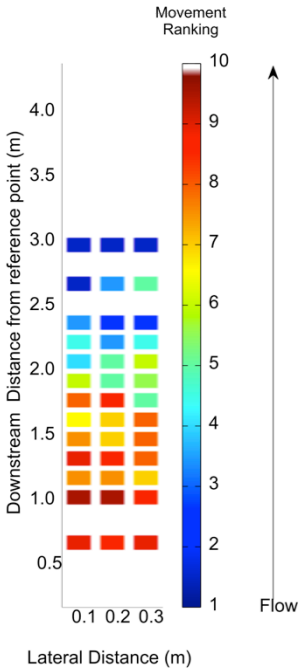

Figure 38: Movement rankings for CDF2-H

The movement rankings generally decrease through the CDF zone. The highest movement potentials are noted immediately downstream of the entry to the CDF at x = 1.05 m where movement occurs instantaneously. Upstream of the bed slope change, the flow depth is shallower and the mean velocity is slightly higher. Specifically, the average of the three near-bed lateral *U* values at x = 1.05 m is approximately 0.4863 m/s and at x = 1.05 is minimally higher at 0.4874 m/s. The region of strong, rapid movement extends to a downstream distance of approximately x = 1.80 m, with strong movement rankings persisting slightly further downstream away from the centerline of the flume. The zone characterizing conditions near the point of incipient motion for the particle of interest extends from approximately x = 1.80 m to x = 2.10 m. Downstream of this location the movement rankings are significantly lower and movement was either not observed, or occurred infrequently.

To determine which parameters most accurately estimate sediment transport potentials, a visual analysis of the scatter plots was completed to compare the movement rankings and the five hydraulic variables (Figure 39). All scatter plots are presented for the CDF2-H conditions.

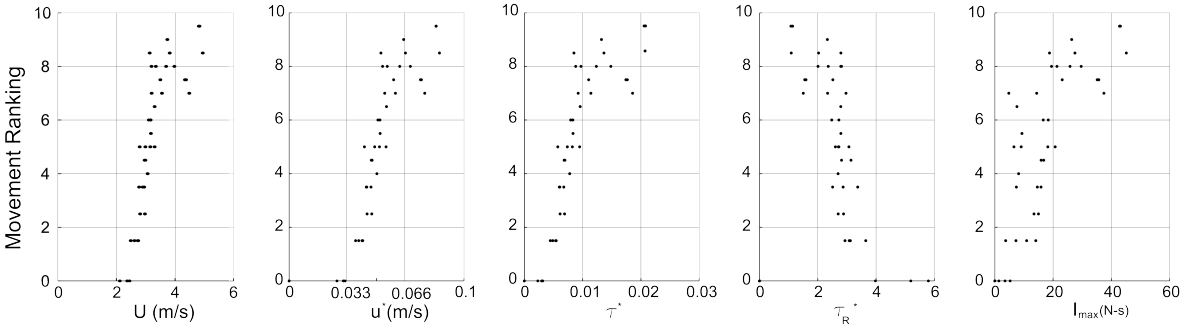

Figure 39: Correlation between movement ranking and a) mean velocity b) shear velocity, c) dimensionless shear stress d) normalized Reynolds stress and e) maximum impulse for CDF2-H configuration

As can be seen in Figure 39a, there is a linear relation between mean velocity and movement ranking. As expected, this demonstrates that *U* can be used as a general indicator of sediment movement capability, whereby larger velocities are typically associated with greater transport potentials. It is noted that for rapid movement (ranking greater than 7), the mean velocities range significantly from approximately 0.31 to 0.49 m/s and therefore mean velocity alone cannot provide a precise estimator of movement potential. The correlation between u^* and movement ranking indicate a similar general linear relationship and provides an additional general indication of sediment transport potential. Correlation between movement and τ^* indicates a similar linear trend, with greater τ^* values generally associated with larger movement potentials. Rapid movement rankings are associated with τ^* values ranging from approximately 0.008 to 0.021. These τ^* values are well below the expected value for the onset of motion (Wong and Parker, 2006), but the use of τ^* for predicting sediment mobility is generally confirmed. The negative correlation between u^* and normalized Reynolds stress implies a decoupling between these two parameters due to turbulence and significantly limits its ability to accurately predict transport potentials. Although *U*, u^* and τ^* can be used as general indicators of sediment transport potential, neither account for turbulence within the velocity time series. The correlation between normalized Reynolds stress, τ_R^+, and movement rankings are provided in Figure 39c. A generally negative correlation is noted, implying that rapid movement occurs during low τ_R^+ conditions. The strength of this correlation is diminished due to the normalization of τ_R^+ by ${u_o^*}^2$, causing increased turbulence intensities to be offset by a reduction in the mean shear stress.

Figure 39d shows the relation between $I_{\max}$ and the movement ranking at each sampling location. A general positive correlation is noted in the data; the highest impulse events are associated with the largest

movement rankings. The three largest impulse events (45.1, 43.1 and 42.8 N-s) are associated with the high movement rankings, 8.5, 9.5 and 9.5 respectively. This indicates that the large I_{max} values are associated with the highest potential for sediment movement. However, the relationship does not appear to be linear in nature. For example, I_{max} values below approximately 15 N-s are associated with a wide range of movement rankings, ranging from no movement or rocking to eventual movement. Similarly, for rapid movement, the distribution of impulse events is significant, with values ranging from 4.8 to 45.1 N-m. The significance of these observations are unknown at this time, but strongly indicate the need for additional laboratory testing.

4.2.2 Low flow rate conditions

Various impulse analyses for the six bed slope configurations under low flow conditions are presented in this section, including the specific role of bed slope, particle size and specific gravity with respect to impulse. The calculation of impulse events in a time series using the u_{cr}^2 estimate in Equation 16 accounts for the local bed slope. However, for the purpose of this analysis, a constant u_{cr}^2 is used for all configurations to allow for a consistent comparison to be made regarding the magnitude and spatial distributions of impulse events as a function of the bed slope. An arbitrarily selected u_{cr}^2 value of 0.0005 m^2/s^2 for a 25.4 mm Teflon particle was used for all bed slope configurations. Using this minimum threshold value, the theoretical impulse events were calculated within the velocity time series from the 'sweet spot' cell at each sampling location. The spatial distribution of maximum impulse events for CDF1, CDF2 and CDF3 bed slopes are provided in Figure 40.

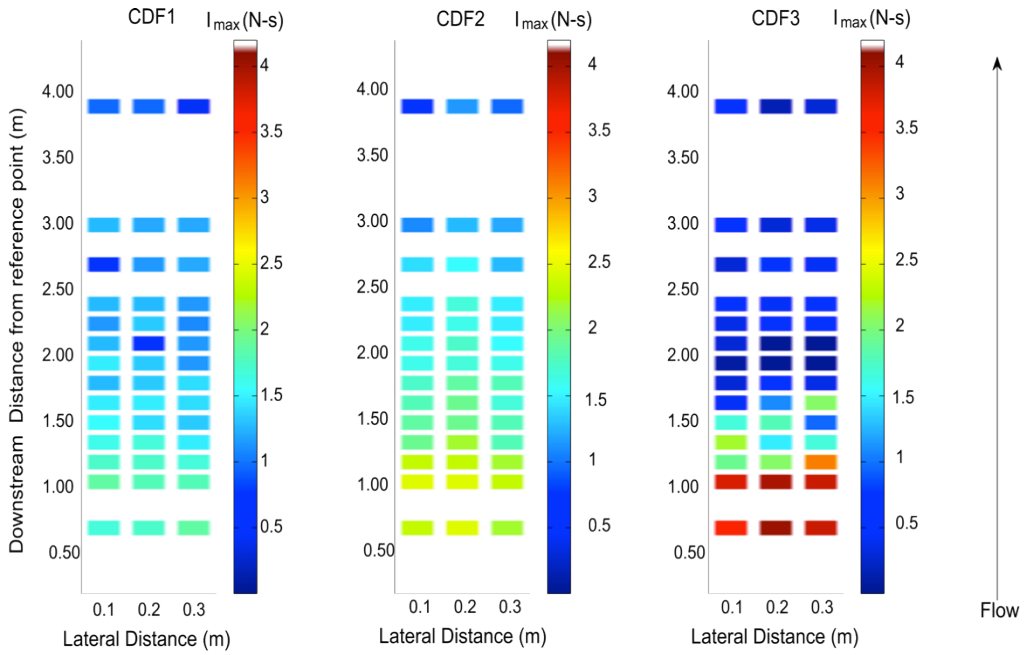

Figure 40: I_{max} distribution for CAF conditions with fixed u^2_{cr}

Under fixed u_{cr}^2 conditions it can be seen that the largest magnitude impulse events occur in the CDF3 bed configuration, reaching a maximum of approximately 3.9 and 4.0 N-s immediately upstream and downstream of the change in bed slope, respectively. For all configurations, the largest magnitude events occur near the upstream entry to the CDF zone, and rapidly decrease after a short distance. The rate of impulse event attenuation is most rapid under the steepest bed slope. For example, for CDF3, a 61% reduction in I_{max} (from an average of approximately 3.85 to 1.49 N-s) occurs in the upstream 0.45 m of the sampling reach. For CDF1 and CDF2, the relative reduction within the same distance is only approximately 10% and 24% respectively.

When the u_{cr}^2 value is not fixed and reflects the local bed slope, u_{cr}^2 values of 0.0052, 0.0043 and 0.0033 m^2/s^2 for CDF1, CDF2 and CDF3 respectively, are estimated. Under low flow conditions, only very small particles are estimated to be mobile, and therefore this analysis should be considered as an illustrative example only and not necessarily representative of natural conditions. A constant particle size and X_{arm} length were selected to produce a range of I_{max} events for all three bed slopes. All calculations are completed for a hypothetical 2 mm Teflon sphere with a X_{arm} length of 0.1 mm. The spatial distribution of I_{max} at each sampling location is provided in Figure 41.

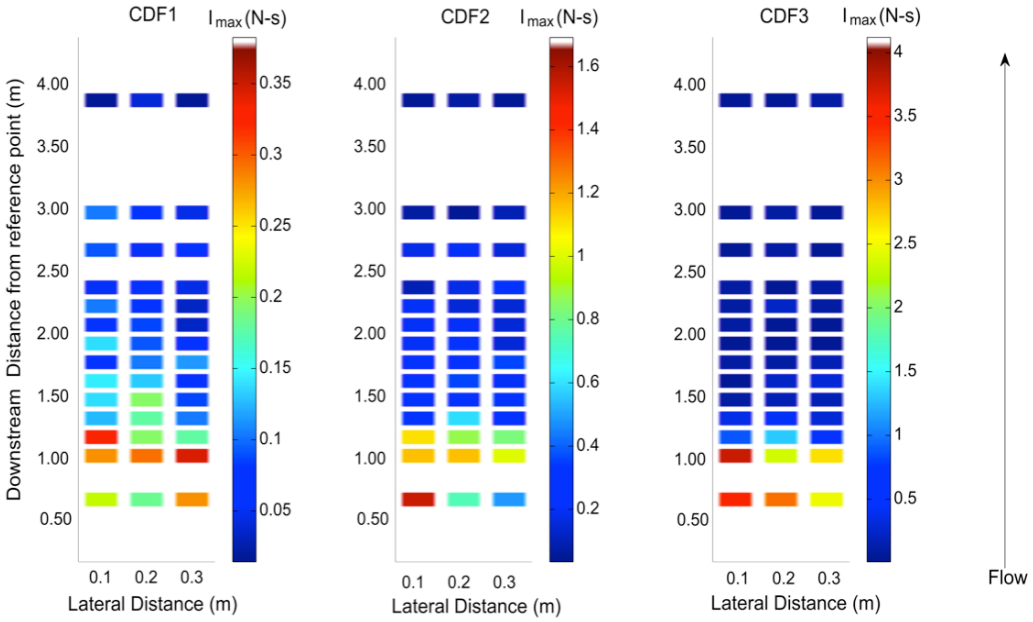

Figure 41: I_{max} distribution for CDF conditions with variable u^2_{cr}

As can be seen in the above figure, the largest impulse events occur in the steepest bed slope, CDF3 near the transition to the CDF zone. Similar to the fixed u_{cr}^2 analysis, it is noted that the steepest bed slope is associated with the most rapid attenuation in the magnitude of impulse events, with an abrupt decline immediately downstream of the first sampling location in the CDF at x = 1.05 m. For the CDF1 configuration, near bed impulse events slowly dissipate and the magnitude of I_{max} at x = 1.50 m is within 50% of the overall maximum I_{max}.

Similar to the CDF bed slope, an analysis of the impulse event distribution under CAF conditions was completed when an equivalent fixed value of u_{cr}^2 of 0.0005 m^2/s^2 was selected (Figure 42).

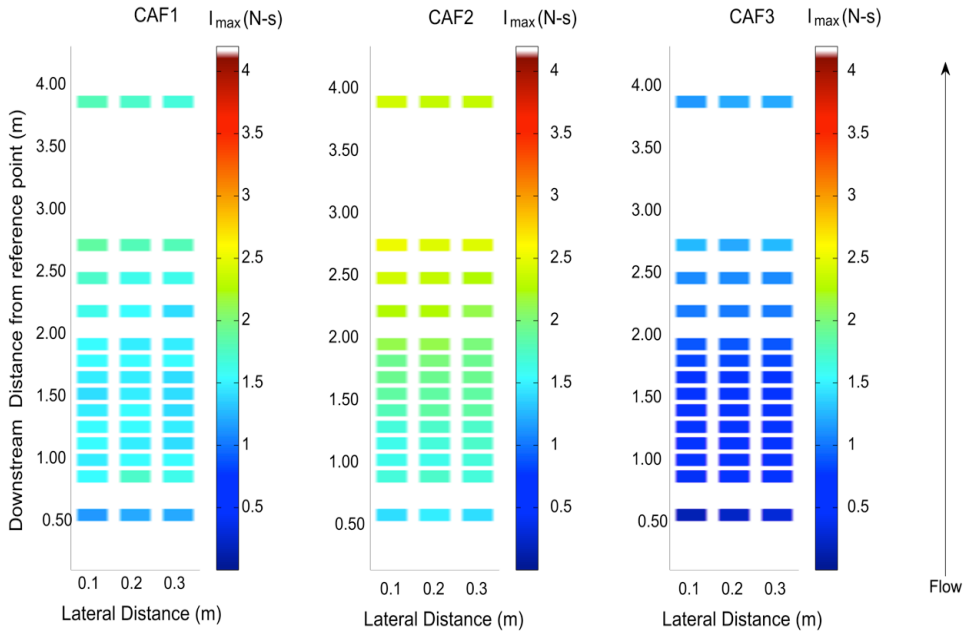

Figure 42: I_{max} distribution for CAF conditions with fixed u^2_{cr}

Under CAF conditions, the I_{max} values are significantly less than under CDF conditions. Detailed data analysis revealed anomalies in the velocimetric data for CAF3 with inconsistent estimated flow rates at different measurement locations. Therefore, interpretation of the results for CAF3 should be handled cautiously. I_{max} values increase from CAF1 to CAF2 conditions, reaching a maximum of approximately 2.6 N-s, near the downstream end of the CAF zone and into the uniform flow section. For all CAF configurations, the I_{max} values consistently increase within the CAF zone. The I_{max} values are slightly larger near the sidewall of the flume, compared to the centerline sampling locations.

Similar to CDF analysis, u_{cr}^2 was varied to reflect the local bed slope under CAF conditions. The resulting u_{cr}^2 values for CAF1, CAF2 and CAF3 are estimated to be approximately 0.0072, 0.0081 and 0.0091 m^2/s^2, respectively for a particle size of 2 mm and X_{arm} length of 0.1 mm. The spatial distribution of I_{max} for each bed configuration is provided in Figure 43.

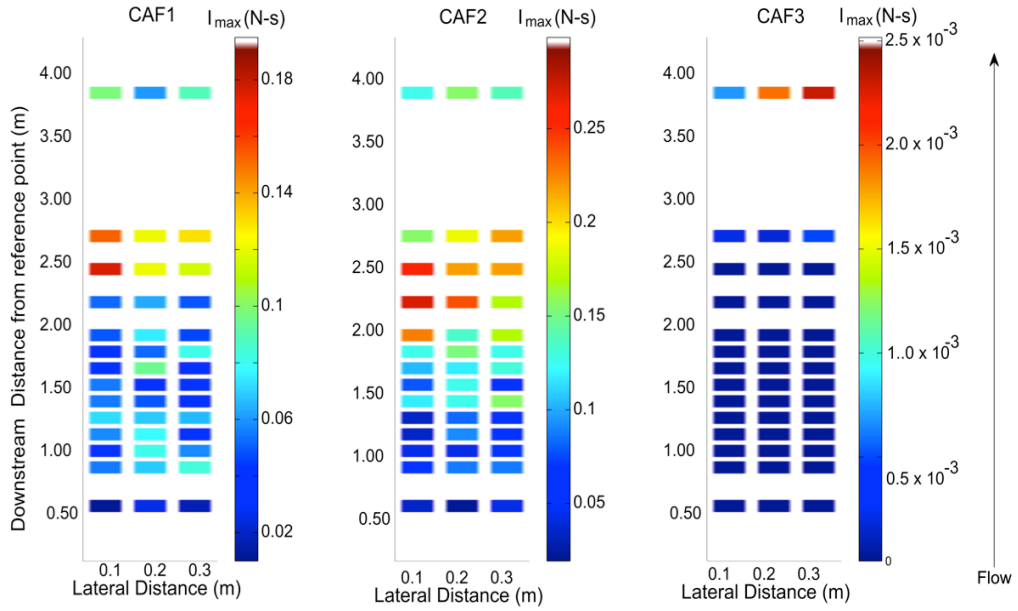

Figure 43: I_{max} distribution for CAF conditions with variable u^2_{cr}

Under variable u_{cr}^2 conditions for the CAF configurations, the impulse events are much smaller than for CDF conditions, with CAF1 producing the most significant impulse events. For CAF1, an I_{max} of approximately 0.17 N-s is estimated near the downstream end of the ramp (x = 2.7 m) where the flow depth approaches a local minimum.

4.2.3 Theoretical sediment mobility considerations

The second set of analysis for the low flow conditions examines the role of particle size in estimating the magnitude and spatial distribution of impulse events. The selective movement of sediments causes particle sorting within bed structures, such as riffle pools, which can significantly affect the local hydraulics and produce feedback mechanisms within bed structures. A theoretical analysis of the collected data was completed to determine the maximum impulse estimated for a range of particle sizes at different longitudinal sampling locations. Near-bed centerline sampling locations at x = 1.05, 1.35, 1.65, 1.95 and 3.00 m downstream of the datum were used and I_{max} is estimated for spherical Teflon particles with diameters ranging from 1 to 20 mm (Figure 44). u_{cr}^2 was not fixed in this analysis and reflects the local bed slope. A X_{arm} length equal to approximately 1/25th of the particle diameter is used. For example, with a 25.4 mm particle, a 1 mm X_{arm} length is used.

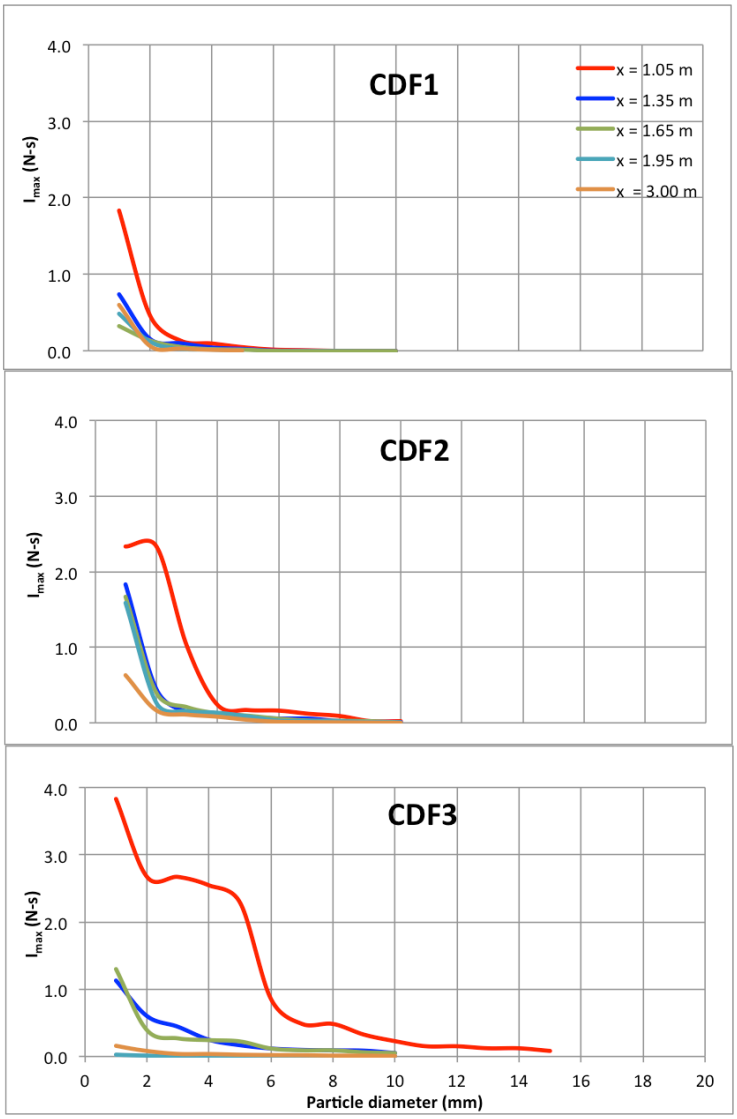

Figure 44: I_{max} values for range of particle sizes for CDF bed configurations

From these figures, three main observations are noted. Firstly, the maximum impulse events are produced during CDF3 bed slope conditions, indicating that turbulence generation is proportional to the bed slope. Secondly, the maximum I_{max} values are produced immediately downstream of the bed slope transition as indicated by the largest impulse events occurring at x = 1.05m. Lastly, the range of particle sizes that produce impulse events is greatest for the CDF3 configuration. Specifically, it is estimated that spherical particles up to approximately 12 mm in diameter will be associated with impulse events and potentially transported under the assumed bed geometry conditions.

The third analysis required for the low flow conditions is determining the role of specific gravity in estimating impulse events. A set of theoretical calculations were made using CDF bed configurations and specific gravities ranging from 1.05 to 4.5 and a X_{arm} length of 2/25 mm (0.08 mm) was used for all calculations. Impulse magnitudes at the entry to the change in bed slope (x = 1.05 m) and at the downstream end (x = 3.0 m) are shown in Figure 45. Calculations for intermediate locations are omitted for clarity, but I_{max} values are noted to be consistently less than 1.0 N-s for all specific gravity values.

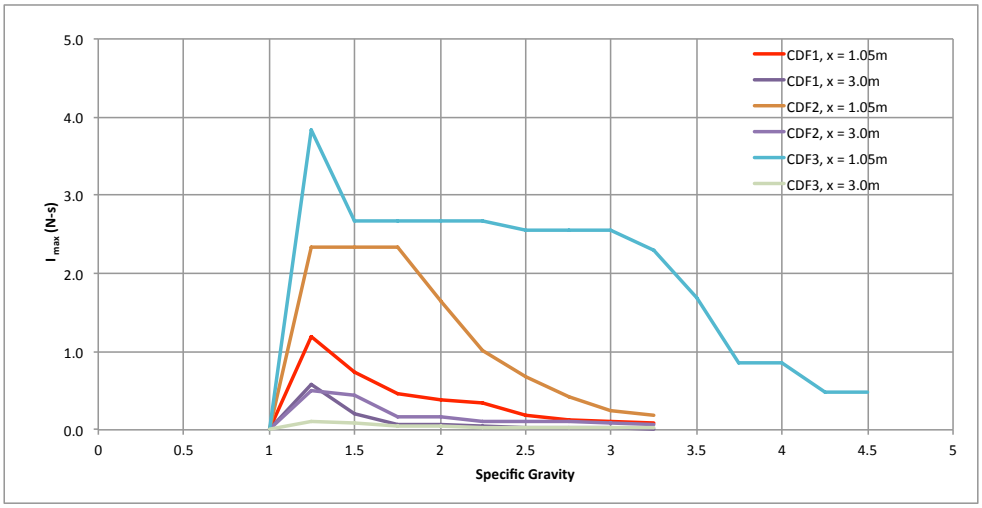

Figure 45: Maximum impulse events as a function of specific gravity

As illustrated in Figure 45, specific gravity is an important factor in determining the magnitude of impulse events and should be considered when the specific gravity of a particle is significantly different than typical sediments. The maximum impulse event is produced for the CDF3 configuration at x = 1.05 m reaching approximately 3.9 N-s. The largest impulse events are associated with specific gravity values of approximately 1.25 at all sampling locations. As expected, low density particles are the most mobile due to their lower gravitation weight, and the largest I_{max} values are produced immediately downstream of the bed slope configuration where turbulence production is at a local maximum.

Chapter 5
PROOF OF CONCEPT

Existing experimental methodologies for determining the precise hydrodynamic conditions that cause individual sediment particles to be transported are inadequate and difficult to implement. The use of correlative techniques, such as those discussed in Chapter 4, provide only a coarse understanding of the link between hydrodynamics and particle movement. New approaches are required that allow for high spatiotemporal resolution testing of the concept of impulse in sediment mobility studies, especially when hydraulic conditions are near the point of incipient motion. This chapter provides background information on existing approaches for synchronized measurement of fluid velocities and particle location as well as new developed methods. This new method is presented as a Proof of Concept and outlines the experimental procedures, required equipment and developed computer programs to track particles of interest in an effort to determine the precise impulse events that cause individual particles to be entrained by a fluid.

5.1 Background

A limited number of research approaches have been developed that couple the measurement of fluid velocities and particle location. In their development and testing of the concept of impulse Diplas et al (2008) and Celik et al (2010) used a laser-based system for determining the precise instant that a particle moved. A helium-neon laser beam was directed at a particle of interest with a photodetector receiving plate located behind the particle. The precise instant of particle movement could be detected as an abrupt increase in the voltage received by the photodetector, and was correlated with recorded fluid velocities to determine the hydrodynamic conditions that caused movement. This experimental procedure successfully determined the instant of particle movement, but could not provide any information regarding the trajectory of particle movement. Frey et al (2003) used image analysis techniques for tracking individual sediment particles to determine the grain size distribution and solid discharge of sediment exiting a flume. This experimental procedure consisted of an adjustable, well-lit ramp at the flume exit, and a video camera mounted above the water surface to collect images at up to 15 frames per second (fps). Particles were tracked between successive frames and a separate algorithm estimated the solid discharge rate and the grain size distribution. While this work successfully demonstrated the ability to track individual particles, determining the hydraulic conditions that caused individual particles to move was not

considered. Nelson et al (1995) synchronized LDV image analysis with velocity measurements to study the movement of a coarse sand bed downstream of a backward facing step. Manual analysis of images from a high-speed camera was completed to estimate the number of sediment particles that passed through a small measurement window over a finite duration. The transport rate was correlated with the velocity time series, thereby providing a method for understanding the velocities that cause bulk transport to occur. However, this study did not consider the movement of individual sediment particles, and requires a manually intensive procedure for image analysis. Additional researchers have used image analysis to track individual particles of interest (e.g., Nino et al, 1994; Bohm et al, 2006) but only a limited number have attempted to simultaneously measure the precise turbulent velocities acting on a particle and its movement. The work of Dwivedi et al (2010) and Radice et al (2013) are noted below as some the first significant attempts to directly study this link.

In their study of the hydrodynamic forces that act on polyurethane spheres, Dwivedi et al (2010) used miniature piezometric pressure transducers to measure the forces acting on individual particles. Using a fixed sphere set up, pressure transducers were installed in the upper, upstream and downstream surfaces of a sphere, as well as in the retaining pocket directly below the particle. Particle image velocimetry (PIV) was used to record the streamwise and vertical fluid velocities at a rate of up to 200 Hz. This study demonstrated the importance of large sweeps in particle mobility and most importantly, is the first known attempt to synchronize the measurement of fluid properties and the mobility of individual sediment particles using image analysis. Radice et al (2013) simultaneously measured bed load sediment concentration and fluid velocities. Images recorded with a high-speed video camera were analyzed to determine the quasi-instantaneous bed load sediment concentration over a 3.5 cm x 3.5 cm sampling window. Two synchronized ultrasonic Doppler velocity profilers (UDVPs) were used to measure the streamwise and vertical fluid velocities. Sediment concentrations and velocity time series records were analyzed to determine what fluid movements produce the specific increases in bed load sediment concentration. The results of this study indicated that at low sediment transport rates, sweep events are most important; while at higher flow intensities, the role of sweeps and ejection events were similar.

5.2 Methods

The development of a Proof of Concept for synchronized measurement of fluid velocities and particle mobility consisted of three components. The first, and most basic component used the bottom depth

measurement feature of the Vectrino II (VII) to identify the time associated with particle dislodgement. More specifically, this approach tested the ability of the bottom depth measurement feature of the VII to indicate when a large solid object below the central transmitter of the VII became mobile. The bottom depth record was evaluated to determine if the precise digital timestamp of the particle motion could be determined and subsequently synchronized with the recorded velocity time series. The second component used a video recorded with a compact digital camera for manual particle tracking and the VII for velocity measurements. This method sought to examine whether it is possible to obtain sufficiently precise synchronization between bottom depth measurements, sediment location and velocity measurements in identifying the turbulent velocities that cause particle movement. Manual removal of a thin disc from the VII bottom depth sampling column was used to provide synchronization between video recording and the VII time series. The particle of interest was positioned slightly upstream of the VII sampling column and its location was recorded by the video camera. By advancing to the estimated timestamp, the sphere became mobile in the velocity time series, the approximate velocities that caused particle movement could be identified. The ability of this method to consistently and precisely identify the turbulent velocities associated with particle movement was tested. The third, and most advanced component used a machine-vision camera and automated analysis techniques to determine the precise digital timestamp associated with particle movement for correlation with the velocities recorded by the VII. Testing was completed using a set of tabletop experiments, with a spherical particle slowly rolled across the table while being recorded by the camera. Automated computer programs offering efficient and consistent analysis are tested. Although not explicitly tested, this approach was designed to be transferrable for use within a laboratory flume. The goals of this third component are:

i. High resolution (frame rate) recording of the particle location
ii. Ability to position the VII at any location relative to a particle of interest
iii. Precise synchronization between velocity measurement and the particle location
iv. Automate the most time-consuming data analysis processes such as frame analysis for particle tracking

5.2.1 Bottom depth measurements

To test the bottom depth measurement feature of the VII, a set of five gravel-sized particles with relatively flat top surfaces were selected. The particle heights were approximately 10, 20, 30, 40 and 50 mm (Figure 46).

Figure 46: Gravel particles used in VII bottom depth measurements

A thin metal sheet spanning the width of the flume was placed directly below the VII on the permanent flume bed. A low, constant flow rate and a flat bed were used to minimize turbulent forces within the sampling region. Each experimental run began with positioning the given gravel-sized particle directly below the central transmitter of the VII on the metal sheet (Figure 47).

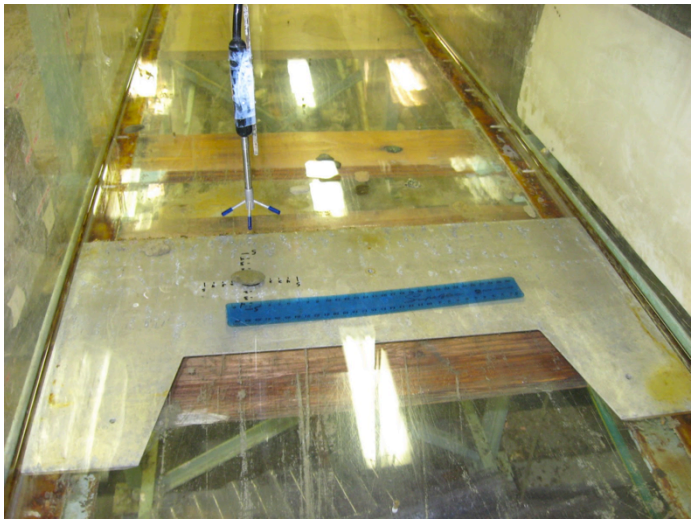

Figure 47: Set up for bottom depth experiments (dry conditions shown)

A thin metal rod was used to slowly slide the particle along the bed of the flume to the outer edge of the VII sampling profile. The particle was then twice gradually slid in and out of the sampling profile. This

procedure was repeated for all five gravel-sized particles, with separate VII recordings of the velocities and bottom depths.

5.2.2 Compact digital camera

Tests using the VII bottom depth measurement, video images and the velocity time series were carried out to determine the ability to obtain the precise velocities that cause particle movement. Within the flume, roughened PVC sheets were laid flat along the bed and the sphere was placed in a fully exposed position on the sheets with no other particles on the bed. The camera was set up outside of the flume and focused on the sphere. Portable lights were used to maximize the contrast between the sphere and the image background. The 'sweet spot' of the VII was positioned one particle diameter upstream and in line with the center of the sphere. A 5 mm metal disc was placed on the bed, directly below the central transmitter of the VII to allow for synchronization between the bottom depth measurements and the recorded video (Figure 48).

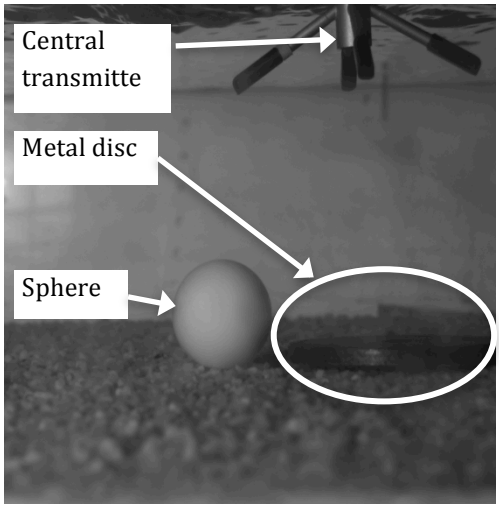

Figure 48: Set up for digital camera method

The flow rate was gradually and incrementally increased so that the sphere was near the point of incipient motion. Once an appropriate flow rate was established and the VII and camera were recording, the metal disc was manually removed using the metal rod (Figure 49).

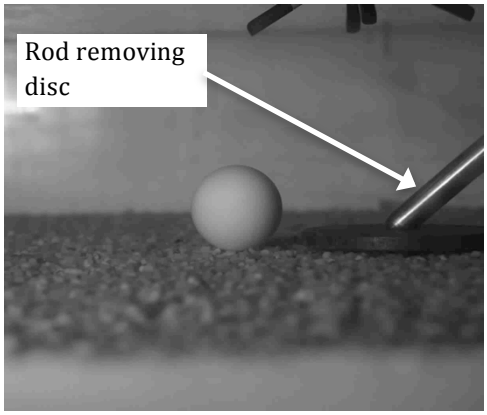

Figure 49: Disc removal with metal rod

If movement of the sphere occurred during or immediately after disc removal, the run was discarded as it was assumed that non-representative conditions caused the sphere to move. If the particle remained in place for at least approximately 20 seconds following disc removal, the run was allowed to proceed and both the VII and the video camera continued recording until the particle was fully dislodged due to natural, representative hydraulic conditions. The digital timestamp associated with disc removal, t_{disc}, was obtained directly from the bottom depth time series. After manual analysis of the video, the duration between disc removal and particle dislodgement ($\Delta t_{disc\text{-}sphere}$) was estimated. By advancing to the timestamp of sphere movement, estimated as ($t_{disc} + \Delta t_{disc\text{-}sphere}$) in the velocity time series, the approximate velocities causing particle movement can be identified.

5.2.3 Machine vision camera

The final component of the Proof of Concept tests the use of a machine vision camera and automated image analysis to obtain precise digital timestamps of particle movement. A machine-vision camera offers high-resolution images, high frame rates and precise digital timestamps of the images as well as the ability to customize the recording procedure for user-specific needs. The Prosilica GT2000™ machine-vision camera by Allied Vision Technologies is a GigE (gigabit Ethernet) camera that offers a frame rate of up to 53.7 fps and a resolution of 2048 x 1088 (Allied Vision Technologies, 2013). The camera is designed to be controlled though third-party software, such National Instruments' Vision Acquisition™ software for use within the LabVIEW™ graphical programming environment. Using this software, images can be continuously acquired and the precise digital timestamp of each image can be recorded. To

determine the precise digital timestamp associated with particle movement, two interrelated LabVIEW programs and a separate Matlab program were developed. Unlike all other methods for studying turbulence and sediment movement in this thesis, testing of this procedure was completed as a set of tabletop experiments under dry conditions. Application of the procedure to a laboratory flume for the tracking of natural sediment particles has not been explicitly tested. The first LabVIEW program controls the camera for image acquisition and records the digital timestamps of each image. In this method, the spherical particle was initially placed on a smooth tabletop surface at the left edge of the camera's field of vision. While recording, the sphere was manually bumped (Figure 50), causing it to roll across the tabletop and exit the far right edge of the frame. Each image is recorded and stored on a desktop computer with a filename reflecting the precise timestamp generated by the computer. Once image acquisition is complete, the program generates a text file with both the timestamp of each image and the corresponding frame number. All timestamps are recorded in the format of HH:MM:SS.sss.

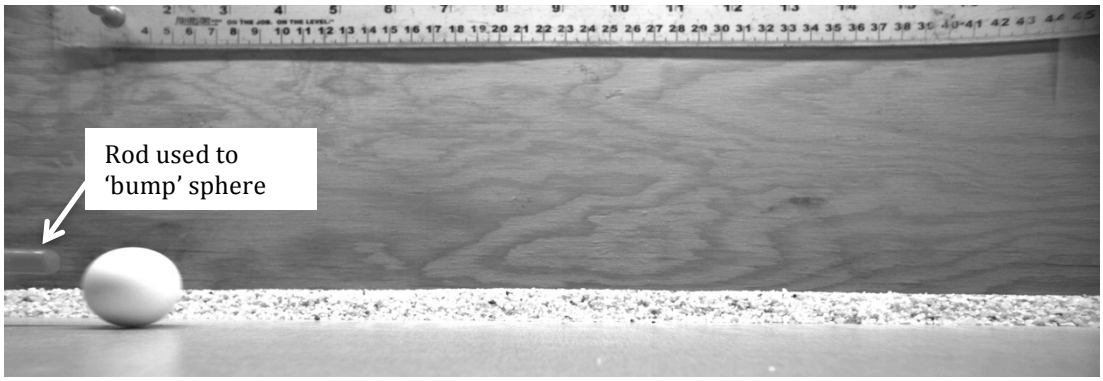

Figure 50: Sediment particle being bumped

The second LabVIEW program analyzes the images to track a selected point (referred to as a 'feature point') within a particle of interest. The first image captured in each experimental run is displayed in a window on the users desktop screen and the user defines the feature point by clicking a point within the particle of interest. The program determines the Cartesian coordinates *(X, Y)*, measured in pixels, of the selected feature point between successive images using Lucas and Kanade's algorithm (National Instruments, 2011). This algorithm uses an optical flow estimation technique to track the displacement of a feature point sharing the same brightness and contrast within a given window of interest between successive images (Lucas and Kande, 1981). After the initial feature point has been selected, no additional action is required by the user during the tracking process. Once all images have been

processed, the program writes the feature point coordinates and digital timestamps for each image to a text file. A Matlab program is then used to process the text files generated by the LabVIEW programs to determine the distance travelled by the sphere between successive frames and most importantly, the digital timestamp associated with initial particle movement. Using the feature point pixel coordinate text file, the distance the particle moves between successive images is calculated using:

$$Displacement\ distance = \sqrt{(x_{i+1} - x_i)^2 + (y_{i+1} - y_i)^2} \tag{29}$$

Where x_i and y_i are the *X* and *Y* pixel coordinates of the feature point in image *i*, respectively. Prior to complete particle dislodgement, minor movement in the feature point coordinates between successive images is expected due to particle rocking as well as apparent movement due to small inaccuracies in the calculated locations. The inclusion of a minimum movement threshold ensures that such events are not falsely detected as movement. For a spherical particle, it is assumed that the particle has been fully dislodged if movement between successive frames is greater than one-quarter of its diameter. To determine the precise timestamp of particle movement, the Matlab program uses the text file containing timestamps and frame numbers to identify the timestamp of the frame immediately prior to movement. This timestamp is saved as a variable for use in velocity analysis programs, such as analysis of a velocity time series to determine which impulse event may have caused particle entrainment.

5.3 Results

5.3.1 Bottom depth measurements

The results of the VII's bottom depth measurement experiments were analyzed to determine the accuracy and ease of use of the VII's bottom depth feature. Selected results of the bottom depth measurements for the 50, 30 and 20 mm particles are shown in Figure 51.

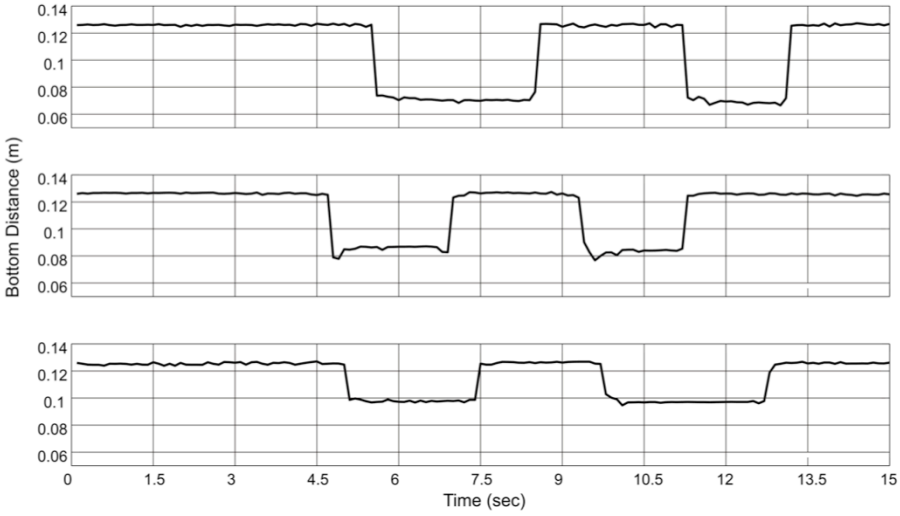

Figure 51: Bottom depth profiles (50, 30 and 20 mm particle heights)

Two important observations are made from these experiments. Firstly, for all particles tracked there is an abrupt and distinct decrease in the bottom depth when the particles were first slid into the sampling column for the 50, 30 and 20 mm particles at 4.7, 4.6 and 5.0 seconds respectively. A corresponding increase in the bottom depth occurs when the particles are slid out of the sampling column at 8.7, 6.7 and 7.5 seconds, respectively. Secondly, the approximate height of the particle removed from the sampling volume can be estimated from the change in the bottom depths before and after removal. The particle heights estimated using the above figure are approximately 55, 35 and 25 mm, respectively, approximately matching the heights measured manually. The results of these experiments indicate that the bottom depth tracking feature of the VII can be relied upon to provide accurate estimates of particle movement within the sampling column.

5.3.2 Compact digital camera

A representative data set, including a video and velocity time series, was used to determine the accuracy of synchronized measurement of particle location and velocity. For this example, a 37 second video consisting of 1124 frames was manually analyzed to determine the time of disc removal and particle movement. It is estimated that the thin metal disc was removed at approximately 7.2 seconds into the video and the sphere moved approximately 27.3 seconds after video recording began. It was not possible

to estimate these durations with greater precision due to the lack of digital timestamps on the image frames. Therefore, it is estimated that approximately 20.1 seconds elapsed between disc removal and particle dislodgement, given by $\Delta t_{disc\text{-}sphere}$. Figure 52 displays a frame captured from the video approximately 0.5 seconds after the sphere is dislodged.

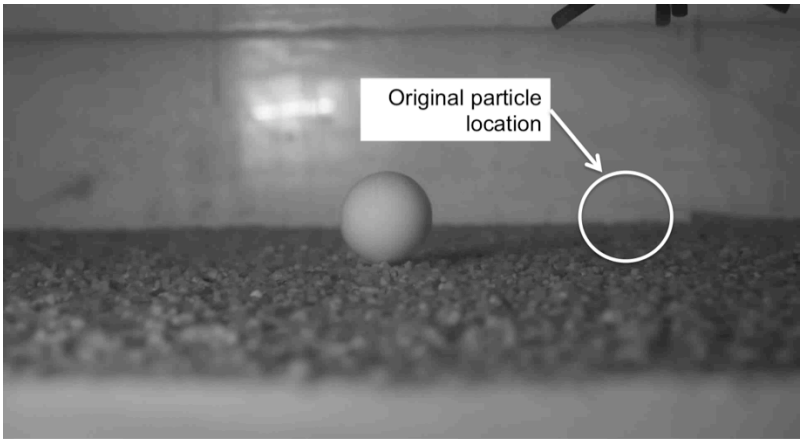

Figure 52: Video frame approximately 0.5 seconds after particle dislodgement

From analysis of the VII's bottom depth time series, removal of the metal disc occurred at approximately 12.80 seconds after recording with the VII began (Figure 53), corresponding to a recorded digital timestamp of 1:35:31:296 PM.

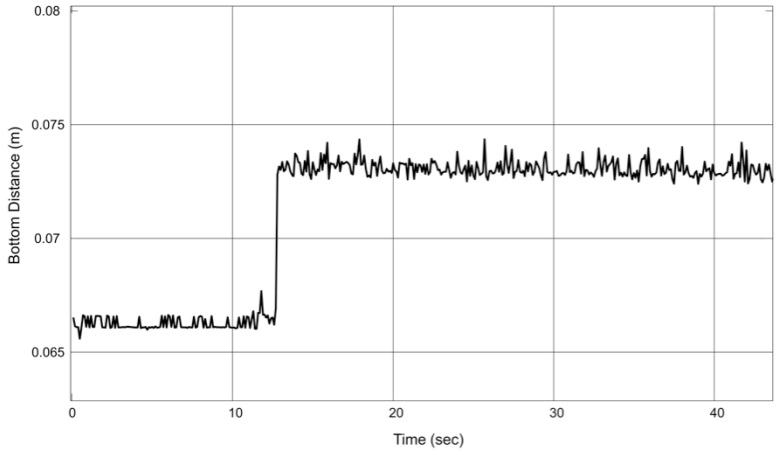

Figure 53: Bottom depth tracking during disc removal

Using the information from the video analysis, particle movement occurs at 32.9 seconds into the VII record (12.8 seconds for VII disc removal + 20.1 second duration given by $\Delta t_{disc\text{-}sphere}$), or at a timestamp of approximately 1:35:44:096 PM. By examining the velocities in the vicinity of this time, a coarse link between particle movement and velocities is established (Figure 54). The solid vertical blue line indicates the approximate time of particle movement. The dotted red line represented the critical velocity estimated for impulse events (0.249 m/s).

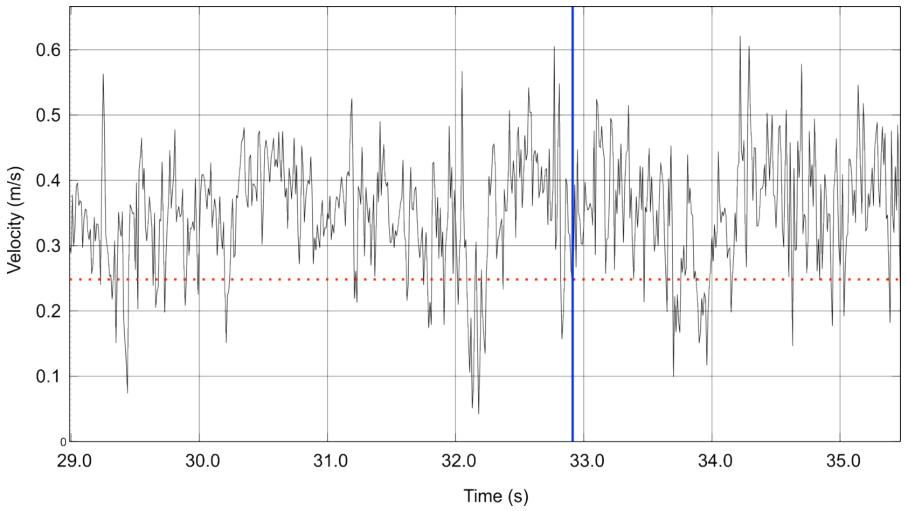

Figure 54: Particle movement estimated to be approximately 32.9 seconds (solid blue line).

From the above figure, it can be observed that particle movement occurs shortly after a region of sustained above average velocities, from approximately 32.2 to 32.7 seconds. To examine the possible correlation between particle movement and coherent turbulent structures, all impulse events within the time series were estimated. For the 25.4 mm Teflon particle with a X_{arm} length of 1 mm, impulse events were calculated for the time series at the 'sweet spot' of the VII (Figure 55). Movement of the particle occurs at approximately 32.9 seconds.

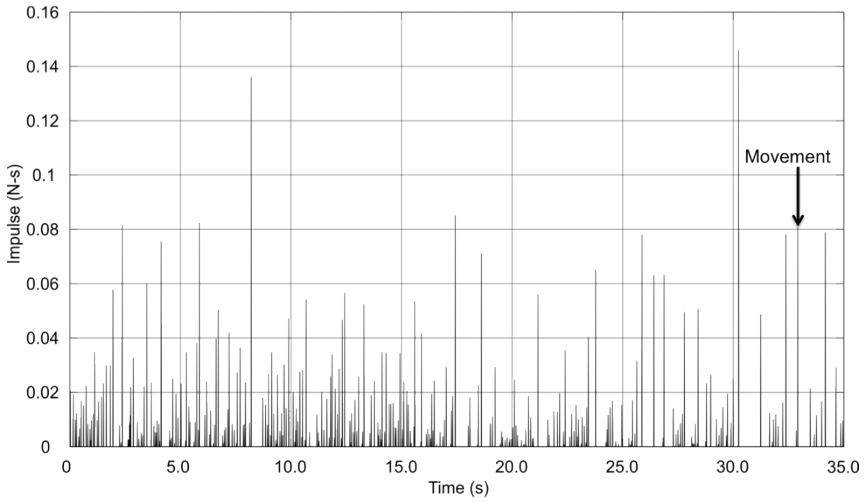

Figure 55: Impulse events in velocity time series

As illustrated in Figure 55, the movement of the particle is associated with a relatively large impulse event, reaching a magnitude of approximately 0.08 N-s. The correlation of movement with this large magnitude impulse event indicates that movement may have been caused by a coherent turbulent structure impacting the sphere. Due to the limited accuracy of precisely determining the duration between disc removal and sphere dislodgement, it is impossible to determine with a high level of confidence the exact velocities associated with particle movement. However, this method provides a preliminary technique for studying the link between sediment transport and turbulent velocities. It is interesting to note that several larger magnitude impulse events occur before final movement (i.e. 7.2, 17.5 and 30.4 seconds), but do not result in full movement of the particle. From an analysis of the video, rocking of the particle is noted at approximately 30.4 seconds, but no movement occurs.

5.3.3 Machine vision camera

This section describes the results of the tabletop experiments using semi-automated LabVIEW and Matlab computer programs to track a particle of interest. An illustrative experimental run tracking a 25.4 mm sphere was selected to illustrate the developed method. The first image was captured at a time of 11:12:46.987 with a recorded filename of IMG_111246.989 (HHMMSS.sss format) and saved in a user-specified folder. The small difference between the digital timestamps generated for the image acquisition and the recorded filename are due to the computer processing time that elapses between acquiring an

image and storing it. For the purpose of this study, these small differences are considered negligible. The digital timestamp, 11:12:46.987 AM and frame number, 1, are temporarily stored to memory and written to a text file when the program is stopped, as well as the timestamp and frame number for all subsequent images.

Figure 56 illustrates the 18 frames relevant to particle movement, including the final frame the particle is stationary (frame 18) and a final frame after the sphere exited the field of vision (frame 36). The 17 frames preceding particle movement are not shown, nor are frames recorded after the particle exited the field of vision. The overlaid square red box highlights the feature point location tracked in each image, with the feature point being at the centre of the box. Particle movement can be visually noted to occur sometime between the second and third frames displayed, corresponding to frames 18 and 19.

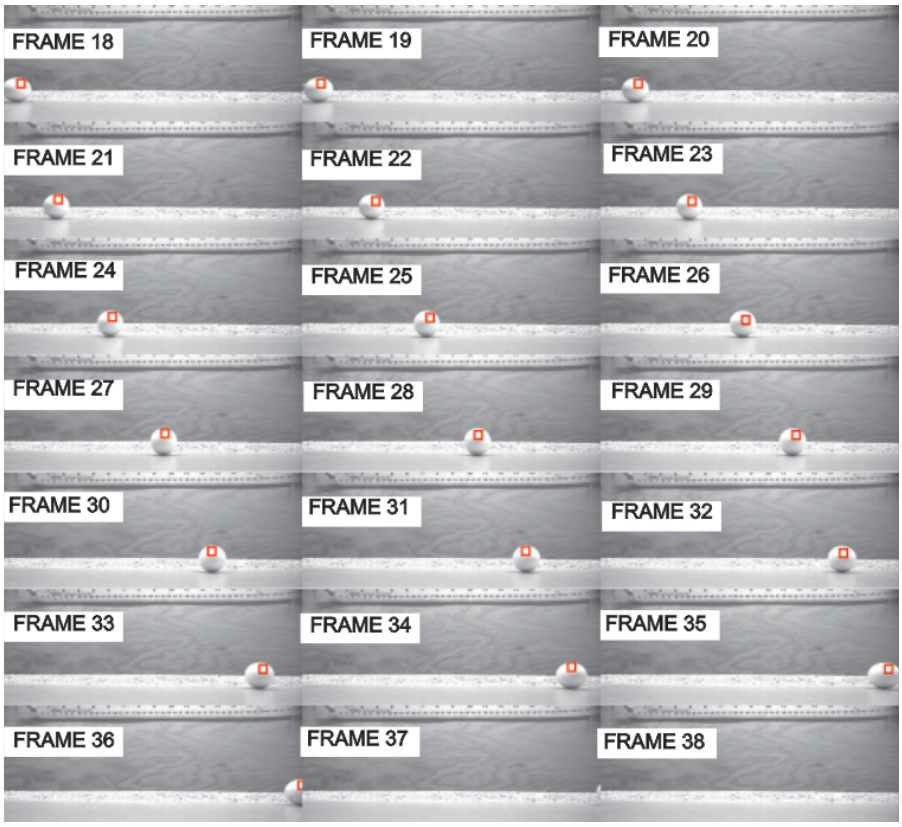

Figure 56: Movement of sphere during tabletop experimental run

The feature point coordinates selected by the user for the first image are (23.651, 529.267), in the upper-right portion of the sphere. The feature point coordinates for all images are recorded to a text file. A summary of relevant feature point coordinates are given in Table 5.

Table 5: Selected feature point coordinates

Frame Number	1	2	3	…	17	18	19	20	21
X (pixels)	23.651	23.609	23.9	…	24.356	50.946	175.638	297.573	410.841
Y (pixels)	539.267	539.935	539.301	…	540.108	540.928	544.017	545.639	549.94
Timestamp (HHMMSS.sss)	111247.169	111247.334	111247.499	…	111249.853	111250.018	111250.183	111250.349	111250.514
Distance (pixels)		0.7	0.7	…	0.3	26.6	124.7	121.9	113.3

The next step is to use the developed Matlab program to determine the distance the feature point moves between two successive images. As can be seen in Table 5, minor movement of the particle occurs between frames 17 and 18. For the 25.4 mm sphere used, the particle diameter corresponds to approximately 202 pixels and therefore the minimum movement threshold is set at a minimum of 50 pixels. The distance the feature point is displaced between frames 17 and 18 is calculated to be approximately 26.6 pixels, and therefore does not exceed the minimum threshold. Between frames 18 and 19 the movement increases to approximately 124.7 pixels indicating that particle movement occurred immediately after frame 18. The timestamp recorded in the text file associated with frame 19 is approximately 11:12:50.183. This variable is stored within Matlab and can be used for algorithms analyzing the VII data.

Although this analysis is preliminary, it successfully proves that the Proof of Concept can be used for particle tracking in a sediment transport study. Highly precise digital timestamps associated with particle movement are reliable for identifying the instant of particle movement. The Proof of Concept procedure developed is fully compatible in a laboratory flume environment with a velocity profiling instrument, such as the VII, positioned immediately upstream of the particle of interest. Furthermore, the outputs of the program have been designed to be fully compatible with the velocity time series format produced by the VII.

Chapter 6
DISCUSSION

This section discusses the suitability of using the newly developed approach for filtering velocimetric data using ARMA models. The results of the flume experiments are also discussed to highlight important findings within zones of accelerating and decelerating flow and the role of bed slope, sampling location, particle size and specific gravity of the sediment. Recommendations for future work to better resolve the impulse events required for particle movement under a range of conditions are presented. The developed Proof of Concept is discussed with respect to providing a methodological procedure for synchronized measurement of fluid velocities and particle mobility.

6.1 ARMA models for filtering velocimetric data

The use of velocity profiling instruments with high spatiotemporal sampling resolutions requires advanced filtering algorithms for spike detection, replacement and classification of data quality in sampling cells. Preliminary testing of the developed filtering method using ARMA models are promising and offer noteworthy improvements compared to traditional filtering techniques. Standard methods, such as Goring and Nikora (2002), poorly define the cutoff parameter and the number of iterations required to end the despiking process. Within the ARMA procedure, the definition of a cutoff parameter using the kurtosis of the model residuals (a_{kurt}) appears to be a simple and efficient method. Additional studies under a range of hydraulic conditions are required to confirm the appropriateness of using an a_{kurt} value of four. Similarly, a fixed $C_{\Delta k}$ equal to 10% of C_k^{single} that accounts for minor improvements in a_{kurt} when a block of data is nearly cleaned requires additional testing. Overall, empirical constants used throughout the developed program, such as those listed in Table 1, have proven to work well in filtering the available data but further validation is required. This testing is recommended to include statistical justification and a sensitivity analysis of the selected values.

Results of the analysis into the ϕ_1 and ϕ_2 coefficients and R^2 values are intriguing. Specifically, ϕ_1 coefficients are greatest in the near bed environment and toward the sidewalls of the flume, and abruptly decrease at sampling locations above the bed. A similar trend is noted with R^2 values being consistently large near the bed, and decrease at elevated sampling locations. An opposite trend is observed with ϕ_2 parameters which are largest above the bed, and are generally lower in the near bed environment.

Additionally, the largest ϕ_2 values are observed along the centerline of the channel, and decrease toward the sidewall of the flume. Agreement with the $\emptyset_1^2 < -4\emptyset_2$ relationship noted by Robert et al (1993) was not observed, but rather an upper boundary at $\emptyset_1 + \emptyset_2 \approx 0.95$ was noted to be most significant. The significance of the $\emptyset_1$ and $\emptyset_2$ model coefficients is largely unknown at this time, however it is hypothesized that they may offer a method for describing the coherent structure of flows. Preliminary results from this study indicate that large, coherent turbulent structures are associated with high R^2 and $\phi_1$values. This offers a potential opportunity for classifying the quality of cells within a sampling profile, whereby an abrupt decrease in the $\emptyset_1$ or R^2 value could be used as an indicator of a poor quality cell. Similarly, the $\emptyset_1$ and R^2 parameters alone may allow for a preliminary estimate of the size and distribution of coherent structures within a sampling reach. An initial estimate of the R^2 for a given block of data may be useful in refining the optimal size of the number of observations within a block of data. For example, if the R^2 value is small, the performance of filtering algorithms may be improved if the block length is reduced.

6.2 Applicability of impulse in sediment mobility

Recognition of the importance of turbulence in sediment mobility is becoming increasingly common among researchers. However, difficulties in simultaneously measuring properties of the fluid and the instant a particle becomes mobile have hampered research studies. The lack of a suitable hydraulic parameter for predicting the initiation of movement, especially under non-uniform flow conditions, has made it extremely difficult to predict the precise conditions that cause particles to become mobile. To begin filling this research gap, Diplas et al (2008) introduced the concept of impulse, to account for both the magnitude and duration of turbulent events that act on a particle of interest. While the work of Diplas et al (2008) and Celik et al (2010) is an immense contribution to the role of turbulence in hydrodynamics, they did not cover the common case of non-uniform flow conditions, such as those present in riffle pool structures. The laboratory flume experiments completed in this study are the first known attempt at characterizing the spatial distribution of impulse events under accelerating and decelerating flows. The high flow conditions under a decelerating slope, CDF2-H were completed with temporally separated particle movement ranking observations and velocity measurements. These experiments showed a decoupling between u^* and τ_R^+, indicating that these parameters cannot be interchangeably used to predict sediment movement potential under non-uniform flow conditions. The u^* parameter provides an approximate indicator of movement potential, with higher u^* values generally associated with larger

movement potentials. The use of dimensionless shear stress, τ^*, indicates general decline throughout the CDF zone; however, calculated τ^* values are consistently below threshold conditions although rapid movement was observed. Neither u^* nor τ^* account for the occurrence of specific turbulent events that cause individual particles to become mobile. The use of impulse offers a promising alternative to commonly used parameters for estimating particle mobility.

The single flow rate used for the CDF2-H configuration successfully provided a range of movement rankings throughout the flume. However, hydraulic conditions at only a limited number of sampling locations were near the point of incipient motion, where the concept of impulse is suspected to be most valuable for understanding particle mobility. At several sampling locations, such as near the transition to the CDF zone, the recorded velocities exceeded u_{cr}^2 for the entire time sampling duration. In these cases, impulse does not provide a meaningful parameter for understanding the role of individual turbulent events that initiate particle movement. From the available experiments, impulse magnitudes ranging from 4.8 to 45.1 N-s are capable of producing movement of a 25.4 mm spherical Teflon particle. This is a significant range, and indicates that additional testing is required to better define the minimum impulse magnitude require for a particle to become mobile. Additionally, the analysis in this study has relied solely on the drag forces that are created due to the streamwise velocities at the 'sweet spot' of the VII. The role of vertical velocities, producing lift forces, have been neglected. Additional analysis of the collected data, including vertical forces, may demonstrate the important role of outward interactions ($v' > 0$) in sediment mobility.

A significant drawback to the implementation of the impulse concept is the difficulty in determining the horizontal moment arm, X_{arm}. This single variable has proven to be exceedingly difficult to estimate, especially on a rough bed where small variations can produce significant differences in the estimated u_{cr}^2 values and the calculated impulse values. The work of Diplas et al (2008) and Celik et al (2010) used a uniform pocket geometry of spherical particles, which allowed for a simple calculation of the contact points between the particle and the bed. An accurate method for measuring X_{arm} or a new experimental set up is required to allow for an accurate of this important variable. Furthermore, the temporal decoupling between determining the particle movement ranking and measuring the fluid velocities with the VII resulted in an analysis that calculated the maximum impulse in the time series, I_{max}, and not necessarily the impulse event that actually caused the particle to move. It is hypothesized that when

hydraulic conditions are at the point of incipient motion, the concept of impulse will be most powerful in accurately describing the mobility of sediment particles. Implementing the Proof of Concept on experiments in a laboratory flume is expected to assist in overcoming this limitation.

The six sets of flume experiments under low flow conditions (CDF1 to CDF3 and CAF1 to CAF3) indicate several important findings. The impulse events generated under CDF conditions are much stronger than under CAF conditions. Additionally, under CDF conditions, impulses are strongest immediately downstream of the transition and along the centerline of the flume, and rapidly attenuate throughout the sampling reach. The largest impulse events are associated with the steepest bedslope, CDF3. The opposite conditions are found under CAF conditions, with the largest impulse events at the downstream end of the transition and are higher near the sidewalls. These findings generally agree with the findings of MacVicar and Best (2013) in their study including the distribution of normalized maximum Reynolds stress in zones of CAF and CDF. An analysis of the role of particle size and specific gravity indicate that the CDF3 bedslope is associated with the ability to move the largest sized particles at the entry to the CDF zone, and progressively finer particles are predicted to become mobile at increasing distance into the CDF zone. These findings may offer an explanation of the natural particle sorting processes that occur within pools. It is hypothesized that the steeper bed slopes are associated with large coherent turbulent structures that pass at increasing distances above the bed. This is observed as a rapid attenuation in the magnitude of impulse events in, for example, CDF3 compared to CDF1. While this study is concerned only with sediment movement in the near-bed environment, analysis of the data can reveal the structure and distribution of turbulent structures under non-uniform flow conditions. Under CDF conditions excess turbulence is generated, whereas under CAF conditions the turbulence is suppressed. With respect to riffle pool formation, laboratory scale testing is required under a range of bedslopes to determine when large amounts of coherent structures begin to move into the bed region under CDF conditions and thus have an important effect on particle mobility and bed morphology. Similarly, under CAF conditions, the suppression of turbulence in the near-bed environment is expected to be a function of the bed slope, and therefore has a similarly important effect on the morphology of the downstream end of a pool. Lastly, the particle size in these experiments relative to the flow depth was excessively large. This caused the particle to extend beyond the boundary layer and into the faster outer layer where the role of turbulence may have been diminished.

6.3 Validity of Proof of Concept

The developed Proof of Concept presented three methods for tracking sediment particles. The final approach uses a machine vision camera and offers the most promising and tested methodology for simultaneously measuring fluid velocity and particle location. In contrast to existing approaches, the Proof of Concept is largely automated and requires minimal user input to track particles of interest. The program determines the precise digital timestamp that a particle becomes mobile and allows for easy correlation with recorded velocities, such as those recorded by the VII. Overall, the Proof of Concept has proven to be effective for tracking sediment particles in a tabletop environment. Although not tested in this study, it is expected that the developed methodology can be readily applied to a laboratory flume environment. Additional automation and refinement of the program is recommended, such as automated calculation of the hydraulic parameters (e.g., impulse) that are associated with movement. Currently, only the digital timestamp of movement is determined and the user is required to separately calculate the associated hydraulic conditions at this timestamp.

The machine vision camera used in this study, the Prosilica GT200, is capable of recorded frame rates of up to 48 fps. However, the desktop computer used was limited to collection rates of approximately 6.5 fps. An improved Ethernet card is required to optimize the collection rate of the camera. Increasing the collection rate to be closer to the optimal frame rate will allow for improved synchronized with the VII and its maximum velocity sampling rate of 100 Hz. This level of precision would allow for the two instruments to be synchronized to within approximately 0.02 seconds of each other allowing for an exceptional ability to determine the precise velocities at the instant a particle of interest becomes mobile.

The Proof of Concept offers unique advantages that other particle tracking techniques do not. The use of image analysis, opposed to a laser-based system, allows for the determination of the trajectory of transported particles. Additionally, information regarding the particle size, speed of movement, number of particles transported and also an approximate mass transport rate can be obtained. Although this level of analysis has not been completed, the Proof of Concept can be adapted in future versions to provide these capabilities.

6.4 Recommendations for future work

The $\emptyset_1$ and $\emptyset_2$ coefficients offer an interesting and potentially rewarding future research area. Studies are required to examine the effect of laboratory flow conditions, profiling instrument selection and natural geophysical flows on the estimated $\emptyset_1$ and $\emptyset_2$ coefficients. The possible application of these coefficients to aid in the filtering of velocity data is of particular interest. The ability to classify the data quality within a sampling cell by examining $\emptyset_1$, $\emptyset_2$ or R^2 values may be of possible use and should be investigated.

From the flume experiments, a significant number of additional studies are required to fully understand the role of turbulence in the mobility of sediment particles. Such studies would focus on understanding the impulse events that cause particles to become mobile under non-uniform bed conditions. Additional testing is required with synchronized measurement of both fluid velocities and particle location when hydraulic conditions near the point of incipient motion. Additional tests are required to determine the minimum impulse event required for the initiation of particle movement for a range of particle sizes. This testing may initially be completed under flat bed conditions, with a consistent pocket geometry, such as a bed of spheres. Testing can also be completed to determine the effect of particle shape, pocket geometry, imbrication, exposure and specific gravity. A significant amount of laboratory flume studies are required to resolve the movement of particles under non-uniform bed slopes. It is recommended that testing be completed with a variety of flow rates such that the regions near the point of incipient motion are produced at the entry, midpoint and exit of the change in bed slope. As previously noted, the velocities during the CDF2-H experiments consistently exceeded the u_{cr}^2 threshold for the entire three minute sampling duration and therefore are unable to highlight the important role of turbulence. Data analysis techniques that account for lifting forces should be developed in future studies. Additionally, the use of smaller particles that are well below the outer layer of flow are recommended to better study the effect of turbulence within the boundary layer.

Minor refinement of the Proof of Concept is expected to be an ongoing process during implementation in a flume environment. One simple goal is the complete synchronization and automation of the selected velocity profiling instrument and machine vision camera. More specifically, it should be confirmed that both instruments are timestamped with the identical digital time. Analysis of particle location to reveal

the trajectory, size of particle, speed, number of transported particles and an estimate of the mass transport rate can also be included in future revisions of the Proof of Concept and associated programs.

Overall, this study aims to be a valuable reference document for researchers and practitioners in applying new methods for understanding the hydrodynamics of non-uniform flow and improved data filtering techniques. Although the methods presented are still in the research stage of development, they offer a strong potential for evolving into a comprehensive set of methods that can be valuable in improving the performance of river restoration projects. The concept of impulse has the potential to provide a powerful explanatory tool for estimating the incipient motion condition of sediment particles for flow over non-uniform boundaries. This understanding could in turn aid in the design of engineered bed structures, such as riffle pools, thereby improving the performance of river restoration projects. The development of a new approach for filtering velocimetric data using ARMA offers unique advantages to researchers compared to current options. More importantly, the ARMA methods have the potential to produce cleaned velocity time series that better reflect the hydraulic conditions, enabling improved interpretation of measured velocities.

Chapter 7
CONCLUSIONS

River restoration projects in gravel bed rivers commonly include the construction of riffle pool structures to promote aquatic habitat and provide flood protection. However, many restoration designs fail due to an incomplete understanding of the hydrodynamics and sediment transport processes. Research studies into the mechanics of the hydraulic conditions that cause sediments to become mobile are limited due to the difficulties in collecting high-resolution, high-quality hydraulic measurements of the fluid properties that are synchronized with the precise instant that particles are entrained by the fluid. This study describes three main components that can improve the study of the hydrodynamics within non-uniform boundaries, such as those in riffle pool structures.

The laboratory flume experiments represent the first known application of the concept of impulse in non-uniform flow boundaries. Although much additional testing is required, results of this study indicate that impulse is a promising explanatory tool for determining the precise hydrodynamic conditions that cause individual particles of sediment to become mobile. Impulse is expected to be most powerful for predicting particle mobility when turbulent flows are near the point of incipient motion. Common parameters, such as shear velocity and Shields parameter offer an incomplete understanding of the mechanics of sediment movement due to the neglected role of turbulence. Results of the flume experiments highlight a negative correlation between shear velocity and Reynolds stress. This indicates a decoupling between these two commonly used parameters due to the neglected role of turbulence in the fluid. Positive correlations between observed movement and shear velocity, Shields parameter, normalized Reynolds stress and impulse demonstrate their general validity in predicting sediment movement. However, only impulse is able to account for individual turbulent events that are hypothesized to be most important for the movement of particles.

The developed Proof of Concept offers a new and promising method for simultaneously collecting fluid velocities and particle location. While full implementation in a laboratory environment was not part of this study, it is anticipated that the Proof of Concept will enable future research projects to determine the precise impulse events that cause particles to become mobile.

The use of high spatiotemporal resolution velocity data requires automated filtering algorithms. The developed method using ARMA models offer unique advantages compared to existing approaches. Results from testing the ARMA algorithms indicate that the kurtosis of the model residuals can be used as a robust and accurate cutoff parameter during despiking iterations. Additionally, the replacement of spikes with the expected value such that the residual term is eliminated offers a valuable tool for replacing spikes with meaningful data that accounts for the local velocity signal while preserving the natural variance.

The methods developed for studying the role of impulse in sediment mobility offer a preliminary, but potentially powerful, means for improving the understanding of the hydrodynamics in non-uniform beds, such as riffle pools. The ability to collect synchronized measurement of fluid velocities and particle location has the potential to understand the precise mechanics of sediment transport under turbulent conditions. Significant refinement and testing of the developed methods is required to fully understand the sediment transport processes that occur in riffle pools. Two future research endeavors are highlighted by this study. Firstly, validation of the velocimetric data filtering approach using ARMA models for use in spike detection, replacement and cell quality classification is required. Secondly, testing of impulse under non-uniform boundaries including a range of particle sizes when conditions are near the point of incipient motion is required. Overall, enhancing the understanding of the precise mechanics of sediment movement in turbulent conditions within riffle pools can enable better design and performance of river restoration projects.

References

Allied Vision Technologies (2013), 'AVT Prosilica GT - Technical Manual', Allied Vision Technologies GmbH.

Annable, W.K.,Watson, C. and Thompson, P. (2012), 'Quasi-equilibrium conditions of urban gravel-bed stream channels in southern Ontario, Canada', *River Research and Applications* **28** (3), 302-325.

Bernhardt, E. O., Palmer, M., Allan, J., Alexander, G., Barnas, K., Brooks, S., Carr, J., Clayton, S., Dahm, C., Follstad-Shah, J., Galat, D. I., Gloss, S., Goodwin, P., Hart, D., Hassett, B., Jenkinson, R., Katz, S., Kondolf, G., Lake, P., Lave, R., Meyer, J., O'Donnell, T., Pagano, L., Powell, B. and Sudduth, O. (2005), 'Synthesizing U.S. river restoration efforts' *Science* **308**(5722), 636-637.

Buffington, J. B. and Montgomery, D. b. (1997), 'A systematic analysis of eight decades of incipient motion studies, with special reference to gravel-bedded rivers', *Water Resources Research* **33**(8), 1993-2029.

Böhm, T., Frey, P., Ducottet, C., Ancey, C., Jodeau, M. and Reboud, J.L. (2006), 'Two-dimensional motion of a set of particles in a free surface flow with image processing', *Experiments in Fluids* **41**(1), 1-11.

Box, G. E. P. and Jenkins, G. M. (1976), *Time Series Analysis: Forecasting and Control*, Holden-Day, San Francisco

Cea, L., Puertas, J. and Pena, L. (2007), 'Velocity measurements on highly turbulent free surface flow using ADV', *Experiments in Fluids* **42**(3), 333-348.

Celik, A. O., Diplas, P., Dancey, C. L. and Valyrakis, M. (2010), 'Impulse and particle dislodgement under turbulent flow conditions', *Physics of Fluids* **22**(4), 046601.

Church, M. and Jones, D. (1982), 'Channel Bars in Gravel-Bed Rivers', *Gravel-Bed Rivers* **113**, 291-338.

Clifford, N., Robert, A. and Richards, K. (1992), 'Estimation of flow resistance in gravel-bedded rivers: a physical explanation of the multiplier of roughness length', *Earth Surface Processes & Landforms* **17**(2), 111-126.

de Almeida, M. G. A. and Rodrıguez, J. F. (2011), 'Understanding pool-riffle dynamics through continuous morphological simulations', *Water Resources Research* **47**, W01502.

Diplas, P., Celik, A., Dancey, C. and Valyrakis, M. (2010), 'Nonintrusive method for detecting particle movement characteristics near threshold flow conditions', *Journal of Irrigation and Drainage Engineering* **136**(11), 774-780.

Diplas, P., Dancey, C., Celik, A., Valyrakis, M., Greer, K. and Akar, T. (2008), 'The role of impulse on the initiation of particle movement under turbulent flow conditions', *Science* **322**(5902), 717-720.

Dwivedi, A., Melville, B. and Shamseldin, A. (2010), 'Hydrodynamic forces generated on a spherical sediment particle during entrainment', *Journal of Hydraulic Engineering* **136**(10), 756-769.

Ferguson (1961), 'On the Rejection of Outliers', *Proceedings of the Fourth Berkeley Symposium on Mathematical Statistics and Probability,* **1,** 253-287

Frey, P., Ducottet, C. and Jay, J. (2003), 'Fluctuations of bed load solid discharge and grain size distribution on steep slopes with image analysis', *Experiments in Fluids* **35**(6), 589-597.

Gomez, B. and Church, M. (1989), 'An assessment of bed load sediment transport formulae for gravel bed rivers', *Water Resources Research* **25**(6), 1161--1186.

Goring, D. and Nikora, V. (2002), 'Despiking Acoustic Doppler Velocimeter Data', *Journal of Hydraulic Engineering* **128**(1), 117-126.

Heymann, S., Latapy, M. and Magnien, C. (2012), 'Outskewer: Using skewness to spot outliers in samples and time series', *Proceedings of the 2012 IEEE/ACM International Conference on Advances in Social Networks Analysis and Mining (ASONAM) 2012*, 527-534.

Hipel, K. W. and McLeod, A. I. and Lennox, W. C. (1977), 'Advances in Box-Jenkins Modeling - 1. Model Construction', *Water Resources Research* **13**(3), 567-575.

Hipel, K.W. and McLeod, A.I. (1994), 'Time Series Modelling of Water Resources and Environmental Systems', Elsevier, New York

Hurther, D. and Lemmin, U. (2001), 'A correction method for turbulence measurements with a 3D acoustic doppler velocity profiler', *Journal of Atmospheric and Oceanic Technology* **18**(3), 446-458.

Julien, P. Y. (2002), *River Mechanics*, Cambridge University Press, Cambridge, UK

Keller, E. and Melhorn, W. (1978), 'Rhythmic spacing and origin of pools and riffles', *Bulletin of the Geological Society of America* **89**(5), 723-730.

Kelley, W.D. and Ratliff, T. (1992), *Basic statistics for laboratories: a primer for laboratory workers*, Van Nostrand Reinhold, New York

Kendall, A. and Koochesfahani, M. (2008), 'A method for estimating wall friction in turbulent wall-bounded flows', *Experiments in Fluids* **44**(5), 773-780.

Kironoto, B. A. and Graf, W. H. (1994), 'Turbulence Characteristics in Rough Uniform Open-Channel Flow', *Proceedings of the ICE - Water Maritime and Energy* **106**, Issue 4, 01, 333-344.

Kironoto, B. A. and Graf, W. H. (1995), 'Turbulence characteristics in rough non-uniform open-channel flow', *Proceedings of the ICE - Water Maritime and Energy* **112**, 336-348.

Lane, S., Biron, P., Bradbrook, K., Butler, J., Chandler, J., Crowell, M., Mclelland, S., Richards, K. and Roy, A. (1998), 'Three-dimensional measurement of river channel flow processes using acoustic doppler velocimetry', *Earth Surface Processes and Landforms* **23**(13), 1247-1267.

MacVicar, B. and Best, J. (2013), 'A flume experiment on the effect of channel width on the perturbation

and recovery of flow in straight pools and riffles with smooth boundaries', *Journal of Geophysical Research: Earth Surface* **118**(3), 1850--1863.

MacVicar, B. J., and C. D. Rennie (2012), 'Flow and turbulence redistribution in a straight artificial pool', *Water Resources Research*, ***48***(2), W02503.

McEwan, I. and Heald, J. (2001), 'Discrete particle modeling of entrainment from flat uniformly sized sediment beds', *Journal of Hydraulic Engineering* **127**(7), 588-597.

Montgomery, D. and Buffington, J. (1997), 'Channel-reach morphology in mountain drainage basins', *Geological Society of America Bulletin* **109**(5), 596-611.

Nelson, J., Shreve, R., McLean, S. and Drake, T. (1995), 'Role of near-bed turbulence structure in bed load transport and bed form mechanics', *Water Resources Research* **31**(8), 2071-2086.

Newbury, R. W. and Gaboury, M. (1993), 'Stream Analysis and Fish Habitat Design: A Field Manual', Newbury Hydraulics Ltd.

Nino, Y., Garcia, M. and Ayala, L. (1994), 'Gravel saltation 1. Experiments', *Water Resources Research* **30**, No. 6, 1907-1914.

Nortek AS (2012), 'Users Guide – Nortek Vectrino II', Nortek Scientific Acoustic Development Group, Boston

Nortek AS (2013), 'Nortek Vectrino II - Principles of Operation - Measuring Currents and Waves', Nortek Scientific Acoustic Development Group, Boston

Parkinson, S., Goodwin, P. and Caamano, D. (2012), 'Flow structure and sustainability of pools in gravel-bed rivers', *Environmental Fluid Mechanics,* CRC Press, *Ch 9*.

Radice, A., Nikora, V., Campagnol, J. and Ballio, F. (2013), 'Active interactions between turbulence and bed load: Conceptual picture and experimental evidence', *Water Resources Research* **49**(1), 90-99.

Razaz, M. and Kawanisi, K. (2011), 'Signal post-processing for acoustic velocimeters: detecting and replacing spikes', *Measurement Science and Technology* **22(**12), 125404.

Richards, K. (1979), 'Stochastic processes in one-dimensional series: an introduction.', *Concepts & Techniques in Modern Geography,* **23**.

Robert, A., Roy, A. and De Serres, B. (1993), 'Space-Time Correlations of Velocity Measuements at a Roughness Transition in a Gravel-Bed River', *Turbulence - Perspective on Flow and Sediment Transport*.

Schmeeckle, M., Nelson, J. and Shreve, R. (2007), 'Forces on stationary particles in near-bed turbulent flows', *Journal of Geophysical Research: Earth Surface* **112**(2).

Shields, F., Copeland, R., Klingeman, P., Doyle, M. and Simon, A. (2003), 'Design for stream restoration', *Journal of Hydraulic Engineering* **129**(8), 575-584.

Smart, G. and Habersack, H. (2007), 'Pressure fluctuations and gravel entrainment in rivers', *Journal of Hydraulic Research* **45**(5), 661-673.

Sumer, B. M., Chua, L. H. C., Cheng, N. and Fredsoe, J. (2003), 'Influence of Turbulence on Bed Load Sediment Transport', *Journal of Hydraulic Engineering* **129**(8), 585-596.

Valyrakis, M., Diplas, P., Dancey, C. L., Greer, K. and Celik, A. O. (2010), 'Role of instantaneous force magnitude and duration on particle entrainment', *Journal of Geophysical Research: Earth Surface* **115**(F2).

Wilcock, P. R. and McArdell, B. W. (1997), 'Partial transport of a sand/gravel sediment', *Water Resources Research* **33**, No. 1, 235-245.

Wong, M. and Parker, G. (2006), 'Reanalysis and Correction of Bed-Load Relation of Meyer-Peter and Müller Using Their Own Database', *Journal of Hydraulic Engineering*, 1159 - 1168.

Yalin, M.S. (1972), 'Mechanics of Sediment Transport', Pergamon Press, 288